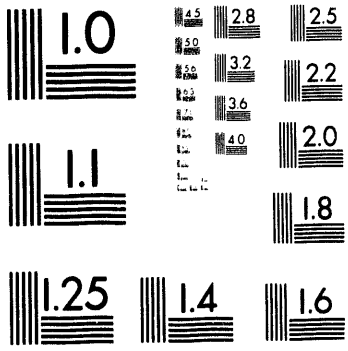
1.0
1.1
1.25
1.4
1.6
1.8
2.0
2.2
2.5
2.8
3.2
3.6
4.0
4.5
5.0
5.6

1 of 2

LBL-34665

SUBMILLIMETER RESIDUAL LOSSES IN HIGH-T_c SUPERCONDUCTORS*

by

David Miller

Department of Physics, University of California at Berkeley, and
Materials Sciences Division, Lawrence Berkeley Laboratory,
University of California, Berkeley, CA 94720

A dissertation submitted in partial satisfaction of the
requirements for the degree of
Doctor of Philosophy

University of California at Berkeley

September 1993

* This work was supported in part by the Director, Office of Energy Research, Office of Basic Energy Sciences, Materials Sciences Division of the U. S. Department of Energy under Contract No. DE-AC03-76SF00098.

Abstract

Submillimeter Residual Losses in High-T_c Superconductors

by

David Miller

Doctor of Philosophy in Physics

University of California at Berkeley

Professor Paul L. Richards, Chair

We have used a novel bolometric technique to obtain accurate submillimeter residual loss data for epitaxial films of $YBa_2Cu_3O_7$ (YBCO), $Tl_2Ca_2Ba_2Cu_3O_{10}$, $Tl_2CaBa_2Cu_2O_8$ (TCBCO), and $Ba_{0.6}K_{0.4}BiO_3$ (BKBO). In this technique the film acts as the absorbing element in a composite bolometric detector. The data are normalized against a reference film of known absorptivity. The loss measurements were made from 25 cm^{-1} to 700 cm^{-1} at 2K. The films used in these measurements were grown by different groups using a variety of deposition techniques and substrates. We have also measured the residual loss for Nb films. We are able to fit the absorptivity measured for the Nb films to an Eliashberg strong coupling calculation, and find excellent agreement between the parameters obtained from the best fits and the measured Residual Resistivity Ratio for the films.

Microwave surface resistance measurements made on the same YBCO and TCBCO films are in excellent agreement with the results of our submillimeter measurements. The microwave measurements were made near 0.3 cm^{-1} (10 GHz) and 4K using resonant techniques. For the YBCO and TCBCO films we obtain good agreement between the submillimeter and microwave data, with the residual losses scaling approximately as frequency squared below 30 cm^{-1} (1 THz). The absorptivities measured for all YBCO films studied are qualitatively

similar, increasing smoothly with frequency, with no gap-like features below the well known absorption edge at 450 cm^{-1}. We are able to fit the losses in the YBCO films to a weakly coupled grain model for the a-b plane conductivity, in good agreement with results from a Kramers-Kronig analysis of the loss data. We observe strong phonon structure in the TCBCO films for frequencies between 60 cm^{-1} and 700 cm^{-1} (2 THz and 23 THz), and are unable to fit these losses to the simple weakly coupled grain model. This is in strong contrast to the case for other high-T_c superconductors such as YBCO, where phonon structure observed in ceramic samples is absent in epitaxial oriented films and crystals because of the electronic screening due to the high conductivity of the a-b planes.

In contrast to the previous results, the absorptivity data for the BKBO films all show a strong absorption onset near the BCS tunneling gap of 3.5 k_BT_c. Comparison of the data with predictions based on strong coupling Eliashberg theory and with results of a Kramers-Kronig analysis indicate that the absorption onset is consistent with a superconducting energy gap.

We have also studied the effects of magnetic field on the residual losses in YBCO films. We observe a resonant absorption feature in the vicinity of the predicted vortex quasiparticle excitation energy $\Omega_0 = \hbar/m\xi_0^2 \sim 100\ cm^{-1}$. We compare our results with some recent predictions.

For my parents, Alan and Naomi

Table of Contents

List of Tables

List of Figures

Acknowledgments

I am truly indebted to so many people whose encouragement, teaching and insight have allowed me to reach this point. This is only a partial list of all those whose time and energy have allowed me to develop as a scientist, and I sincerely thank them all.

My labmates have been my primary teachers, and I am grateful for the time and energy that they have shared with me. I have been exceedingly lucky to have had the honor of being labmates with such a dedicated and good-natured group of people. Tom Kenny was my original mentor in the Richard's group, and his understanding of physics has often been an inspiration to me. Simon Verghese has been an excellent teacher to me and I have often been amazed with the breadth of his understanding of physics. Carl Mears has provided me with much insight, and I have benefited from the depth of his knowledge. John Birmingham, whose desk was next to mine for the past several years, has been a constant source of companionship and amusement in the lab, and I have often been inspired by his dedication to his work. Both Marc Fisher and Mark Sherwin were a useful source of information when I began research in the Richard's group. Jamie Bock has provided me with information on how to make filters necessary for my measurements and has often provided me with the filters themselves. Bill Creager was a helpful companion in my early days in the Richard's group. I would also like to thank Michael Nahum, Quing Hu, Bob Phelps and Warren Holmes.

I am particularly indebted to all those individuals who have provided me with superconducting films. Without such films my measurements would not have been possible. I have been particularly lucky to have had access to some of the best high-T_c films grown in the world. I sincerely thank Chang-Beom Eom,

T. Venkatesan, Nate Newman, Eric S. Hellman, Chris Platt, Jun Amano, Wen Lee and Paul Merchant.

Jeff Beeman and John Emes in Eugene Haller's group at LBL have supplied me with the NTD thermistors used in my experiment. Without these thermistors my measurements would not have been possible, and I sincerely thank the entire Haller group for their support.

I would like to thank Dr. Alan Portis at U.C. Berkeley for many helpful, extended conversations, as well as for some key insights that critically aided in my understanding of the weakly coupled grain model.

Elisabeth J. Nicol at U.C. Santa Barbara provided me with the Eliashberg calculations used to fit the losses in Nb and BKBO. I would especially like to thank Elisabeth for all of her work and for her patience in teaching me about her calculations. It has been a pleasure collaborating with Elisabeth.

The work on the field dependent losses was partially stimulated by Bob Taber, who also provided YBCO samples. The field dependent work has also benefited greatly from conversations with Steve Spielman, Beth Parks and Professor Joe Orenstein.

Certain individuals provided me not only with useful discussions and insight but also with important auxiliary measurements related to my work. Nate Newman formerly of Conductus not only provided me with YBCO films and microwave measurements made on these films but has encouraged my thinking of the complex microstructure of epitaxial films. Steve Garrison at Conductus has been exceedingly generous with his time and taught me about x-ray measurements, and provided me with such measurements on several of my samples. John Martens formerly of Sandia Labs provided me with extensive microwave measurements.

From time to time I have met individuals at various conferences who have influenced my work. Gordon Thomas has often been a familiar face, full of enthusiasm, insight and support. I would also like to thank Gordon for giving me the opportunity of attending the NATO Advanced Study Institute at St. Andrews, Scotland, 1991. Steve Anlage has offered much useful insight, encouragement and data. I would like to thank D. Wayne Cooke and Alan Portis for inviting me to various Los Alamos sponsored conferences. Shahab Etemad has not only provided me with insight but samples and data as well.

Finally, I would like to thank Professor Paul Lindford Richards for allowing me to work in his group. It has been a long and sometimes difficult journey for me. Most importantly, I am honored to have had the opportunity to work with someone whose scientific rigor and intellectual honesty is of the highest order, and who has hopefully set the standard by which I will judge my future scientific accomplishments.

1. Introduction

Optical measurements at far infrared frequencies have traditionally played an important role in understanding the superconducting state. While the optical properties of a metal in the visible and near infrared do not change upon transition to the superconducting state, the metal becomes a perfect conductor near dc. It is at far infrared frequencies where the most dramatic changes in the optical properties of a superconductor occur.

The theory of Bardeen, Cooper and Schrieffer[1] showed that at $T = 0$ there would be a finite energy gap $E_g = 2\Delta = 3.5\, kT_c$ between the ground state of the superconductor and the lowest excited state, one in which a bound pair is broken and two Fermi excitations have been created. This gap frequency optically manifests itself at far infrared frequencies and below. The existence of this gap was demonstrated spectroscopically in many conventional, Type I superconductors such as aluminum, lead and tin.[2-5] The experiments of Joyce and Richards[6] on lead further observed the interaction between phonon excitations and the superconducting states, and demonstrated how infrared measurements are capable of yielding important information on the excitation spectrum of the system in the energy range of a few times the energy gap.

Soon after their discovery by Bednorz and Müller[7] infrared spectroscopy was used to study the optical properties of the high-T_c superconductors.[8] Much of this work was driven by the spectacular success of infrared spectroscopy in elucidating the optical properties of the conventional superconductors. The measurements on the high-T_c superconductors, however, were and still are complicated by several factors, including the highly anisotropic nature of the cuprate superconductors, and also by the difficulty of growing crystalographically perfect specimens of a size suitable for precise spectroscopy. Because of these factors optical measurements almost invariably consist of complicated averages of the anisotropic response. For example, $YBa_2Cu_3O_7$ (YBCO), perhaps the most structurally complicated of the high-T superconductors, has an orthorhombic crystal structure and is optically biaxial. Because the a and b unit cell lengths are nearly equal, twinning occurs in all but thermomechanically detwinned specimens,[9] so that most optical measurements of the a-b plane conductivity of YBCO contain some average of the a-b plane response. Thermomechanically detwinned single crystals of YBCO are typically of submillimeter dimensions, making low frequency optical measurements extremely difficult because of diffraction effects. It is therefore difficult to uniquely determine all components of the conductivity tensor for the cuprate superconductors, which is necessary for a complete understanding of these materials. In addition, because of the difficulty in growing crystalographically perfect specimens it still remains unclear what role, if any, defects have on the optical and transport properties of the high-T_c materials.

Still another major obstacle towards understanding the properties of the high-T_c superconductors is the complicated behavior of the normal state of these materials.[10] The a-b plane resistivity of the cuprate superconductors

is linear, or nearly linear, in T up to the highest measured temperatures, while the c axis resistivity exhibits the opposite, or "semi-conducting," temperature dependence.

As will be discussed in Chapter 3, much of the early work on YBCO was devoted to finding the superconducting gap, as manifested by a region of perfect reflectivity occurring at low temperature. Despite the considerable experimental complications outlined above, many such 'sightings' of the gap were reported in the literature.[11] In fact, it is becoming clear that there is no such region of perfect reflectivity in any of the cuprate superconductors. It should be noted that even for the conventional superconductors, there has always been the troublesome presence of residual losses, namely, losses at low temperature and low frequency in excess of what is expected from the conventional theories of superconductivity.[12] These residual losses are generally only observable in very high Q superconducting cavities operated at low temperatures. The residual losses in such systems are independent of temperature and field level, and have a frequency squared dependence.[12,13] Although several mechanisms have been proposed to explain residual losses in conventional superconductors,[14] this phenomenon is still not well understood.

In order to improve the accuracy of the far infrared measurements in high-T_c superconductors we have developed a novel technique for directly measuring the residual loss. In this technique the high-T_c film acts as the absorbing element in a composite bolometric detector. Most far infrared spectroscopic techniques rely on measurement of the reflectivity, R. In our technique the absorptivity A is measured directly. The absorptivity at low temperature, where our measurement is done, is just the residual loss. In principle these measurements give precisely the same information when

studying optically thick samples, since in this case R = 1 - A. However, sources of experimental error which tend to multiply the resulting spectra such as drift, sample placement errors, standing waves, which can dominate the signal for reflectivity measurements when the reflectivity is close to unity are minimized in the absorptivity measurement. For this reason there are significant advantages to direct absorptivity measurements over reflectivity measurements when the sample reflectivities being studied are close to unity, which occurs for the high-T_c superconductors below approximately 300 cm^{-1}. In addition, uncertainties associated with the precise determination of unity reflectivity are minimized by measuring the absorptivity directly. Direct absorptivity measurements are also less sensitive to substrate properties than transmissivity measurements. Since the first results of our experiment were announced,[15] similar techniques have been used by others to measure absorptivity in single crystals of YBCO.[16]

We have studied the optical properties of epitaxial high-T_c films of $YBa_2Cu_3O_7$, $Tl_2Ca_2Ba_2Cu_3O_{10}$, $Tl_2CaBa_2Cu_2O_8$, and $Ba_{0.6}K_{0.4}BiO_3$ as well as Nb.[17-21] The films we have studied are grown on a variety of substrates using a variety of deposition techniques. Epitaxial oriented films of high quality can be grown with centimeter dimensions, making spectroscopic measurements relatively easy. In contrast, crystals generally have millimeter dimensions, and detwinned crystals have submillimeter dimensions. By studying films which are several times thicker than the superconducting penetration depth we avoid complications due to substrate properties. However, thin film growth is an extremely difficult and complicated process in its own right.[22] For example, the epitaxy of the film is strongly influenced by the choice of substrate and deposition conditions.

Another important area of study is concerned with potential device applications for the high-T_c materials. It is extremely important to understand and minimize the microwave loss of the high-T_c superconductors so that high-T_c microwave devices can become competitive with conventional technology. Potential device types include resonators, filters, delay lines, couplers, antenna matching networks[23,24] and bolometric detectors,[25] among others.

In order to improve our understanding of the microwave, millimeter and submillimeter losses we have also compared our results to the microwave losses measured on the same films. Using the well documented frequency squared dependence of the microwave loss up to 100 GHz,[26] we can infer the loss in our films over four decades in frequency.

Because of its potential importance in elucidating the electrodynamics of superconductors we have also studied the magnetic field induced absorptivity in epitaxial films of $YBa_2Cu_3O_7$. In this measurement the high-T_c film is the absorber in a bolometric detector with the film placed at the center of a 3 Tesla superconducting magnetic solenoid. This measurement is made between 50 cm^{-1} and 200 cm^{-1} at 2 K. The effect of a magnetic field on the submillimeter optical properties of high-T_c superconductors has been measured by other workers,[27,28] and several models for this effect have been reported in the literature.[27-30]

1.1. Outline of Thesis

The outline of this thesis is as follows:

The remainder of Chapter 1 contains brief outlines of the general theory of infrared absorption, of the Kramers-Kronig analysis technique and

of an Eliashberg strong coupling calculation which we have used to model the losses for Nb and for $Ba_{0.6}K_{0.4}BiO_3$ films.

Chapter 2 contains a description of the experimental techniques used in the direct absorption measurement, including a brief review of bolometer theory and Fourier Transform Spectroscopy. The results of submillimeter absorptivity measurements on Nb films and an analysis using an Eliashberg strong coupling calculation are also contained in Chapter 2.

The results of studying epitaxial c-axis oriented films of $YBa_2Cu_3O_7$ (YBCO) are contained in Chapter 3. Along with the submillimeter absorptivity data, the microwave surface resistance was also measured at 10 GHz (0.3 cm^{-1}) and 4K for the same films. Using the well documented frequency squared dependence of the microwave loss up to 100 GHz,[26] we can infer the loss in the YBCO films over four decades in frequency. The results of our measurements are compared to a three parameter model which can be interpreted either in terms of a weakly coupled grain model or a homogeneous two-fluid model with residual normal conductivity. We use these models to phenomenologically describe the microwave and submillimeter losses in our samples, and comparison is made to the results of a Kramers-Kronig analysis.

In Chapter 3 we also analyze the effects of uncertainties in the low frequency optical properties on the electrical conductivity $\sigma(\omega)$ determined from a Kramers-Kronig analysis for the case of low temperature measurements made on YBCO samples.

The results of studying epitaxial c-axis films of $Tl_2Ca_2Ba_2Cu_3O_{10}$ and $Tl_2CaBa_2Cu_2O_8$ (TCBCO) is contained in Chapter 4. The microwave surface resistance was also measured at 10 GHz (0.3 cm^{-1}) and 4 K for these films. We have also made x-ray scattering measurements on these films.

The results of studying epitaxial $Ba_{0.6}K_{0.4}BiO_3$ (BKBO) films is contained in Chapter 5. Because the BKBO films we studied are only slightly thicker than the penetration depth, we have corrected for effects due to the finite film thickness. We compare the results of our measurement with an Eliashberg strong coupling calculation.

In Chapter 6 we discuss the effects of a magnetic field on the submillimeter optical properties. We use the two-fluid and weakly coupled grain models and two recent models for the field dependent complex conductivity $\sigma(\omega;H)$ to analyze measurements we have made on epitaxial films of $YBa_2Cu_3O_7$. These measurements were made using the direct absorption technique at 2K in fields up to 3 Tesla and for frequencies between 50 cm^{-1} and 200 cm^{-1}.

1.2. General Theory of Infrared Absorption

The response of a metal to an electromagnetic field is given by the complex conductivity $\sigma(\omega,\mathbf{q})$ for frequency ω and wave vector $\mathbf{q}$. For example, $\sigma(\omega,\mathbf{q})$ for a normal metal can be obtained by applying Fourier analysis to the well-known Chambers integral expression for the current $\mathbf{J}(\mathbf{r},t)$.[31] Knowing $\sigma(\omega,\mathbf{q})$ we can in principle solve the electromagnetic response of a homogeneous medium using Maxwell's equations and a suitable Fourier analysis of the fields involved. For example, from solving Maxwell's equations we find that the absorptivity $A(\omega)$ of a homogeneous medium filling the half space $x > 0$ is

$$A(\omega) = 1 - \left| \frac{\frac{4\pi}{c} - Z(\omega)}{\frac{4\pi}{c} + Z(\omega)} \right|^2 . \qquad (1.1)$$

The quantity $4\pi/c$ is the impedance of free space in cgs units, which is equal to 377 $\Omega/$ in MKS units. cgs units will be employed exclusively throughout this work. $Z(\omega)$ is the surface impedance defined by

$$Z(\omega) = \frac{4\pi}{c} \left(\varepsilon_\infty + i \frac{4\pi\sigma(\omega)}{\omega} \right)^{-1/2} \quad . \tag{1.2}$$

The quantity ε_∞ is the value of the dielectric constant at high frequency, and can be neglected at low frequencies where $\varepsilon_\infty << |4\pi\sigma(\omega)/\omega|$. A more general definition of the surface impedance $Z(\omega) = R_s(\omega) + i\, X_s(\omega)$ is

$$Z(\omega) = \frac{E_y(x=0)}{\int_0^\infty J_y(x)dx} \quad , \tag{1.3}$$

where J is the current induced in the medium. At low frequencies for which $|Z(\omega)/(4\pi/c)| << 1$ the surface impedance and absorptivity are related by $A(\omega) = (c/\pi)\, R_s(\omega)$. The relationship between $Z(\omega)$ and $\sigma(\omega,\mathbf{q})$ or equivalently between $\sigma(\omega)$ and $\sigma(\omega,\mathbf{q})$ has been determined by Reuter and Sondheimer[32] for the case of either diffuse or specular scattering of the electron carriers at the surface of the medium. These expressions involve integration of $\sigma(\omega,\mathbf{q})$ over the variable $\mathbf{q}$.

Although calculation of $A(\omega)$ or equivalently $Z(\omega)$ from $\sigma(\omega,\mathbf{q})$ is in general quite complicated, there are two limiting cases.[31] The dominant Fourier components of $\sigma(\omega,\mathbf{q})$ occur roughly for $q \sim 1/\delta$, where the skin depth is defined by $\delta = (c^2/2\pi\omega\sigma_0)^{1/2}$. σ_0 is the dc conductivity. When the mean free path l is much larger than the skin depth δ, i.e. when $l >> \delta$, then the

dominant Fourier components of $\sigma(\omega,\mathbf{q})$ occur for $q \sim 1/\delta << 1/l$ and we can approximate $\sigma(\omega,\mathbf{q}) \sim \sigma(\omega,0) = \sigma(\omega)$ in the expressions of Reuter and Sondheimer. In this limit an electron will suffer many collisions during the time spent in the skin layer δ and during one period of the light wave. There is a well defined local, instantaneous relationship between the induced current and total electric field. This is known as the local, or classical skin effect limit. When $\delta >> l$ then the dominant Fourier components of $\sigma(\omega,\mathbf{q})$ occur for $q \sim 1/\delta >> 1/l$ and we can approximate $\sigma(\omega,\mathbf{q})$ by the asymptotic form as $ql \rightarrow \infty$. This is known as the extreme anomalous limit.

Another important length scale to consider is v_F/ω, the distance which an electron travels in a period of the radiation field. In analogy with the discussion in the previous paragraph, if $v_F/\omega << \delta$ then a local conductivity is adequate to describe the electrodynamics; otherwise one must use $\sigma(\omega,\mathbf{q})$ in the full non-local calculation given by Reuter and Sondheimer.

1.2.1. Volume versus Surface Absorption

A photon of energy $\hbar\omega$ and momentum $q = 0$ incident on a conducting medium will only be absorbed if the momentum of the excited electron-hole pair is conserved. In general, momentum is conserved by the presence of collisions or, as will be discussed below, by the presence of excitations. However, even a collisionless or excitationless electron gas has a dissipative mechanism: Since momentum transfer normal to a surface is not conserved (because the translational invariance is broken at the surface) a photon can excite an electron-hole pair at the surface of the collisionless electron gas. However, this process can only occur if $q > \omega/v_F$, where $1/q$ is the distance which an electron travels in one period of the radiation field. Any lower q

would imply a wave with velocity greater than v_F which could not transfer energy and momentum to an electron-hole pair. This is known as surface absorption because of the role of the surface in the absorption mechanism. Surface absorption is associated with the large q contributions of $\sigma(\omega,q)$. When collisions are added, absorption becomes possible for all values of ω and q. For $\delta >> l$, the electron suffers many collisions within δ of the surface, independent of the surface, corresponding to what is called volume absorption.

When $l >> \delta$ ($\delta >> l$), surface (volume) absorption is usually the dominant mechanism for absorption. For all of the materials studied in this work, $\delta >> l$ so that all of our calculations are done in the $q \rightarrow 0$, or local limit. For the high-T_c materials in the superconducting state, $\delta \sim \lambda >> l$. In this limit we only need to consider local electrodynamics where $\sigma(\omega,q) \sim \sigma(\omega,0) = \sigma(\omega)$.

1.2.2. Impurity- and Excitation- Assisted Absorption

Our discussion so far has been limited to impurity and surface scattering. In general, there are two physical processes that are relevant for calculating the optical conductivity $\sigma(\omega)$: impurity-assisted absorption and excitation-assisted absorption. In both cases we are interested in the response of the system to an incident photon of energy $\hbar\omega$ and momentum q = 0. The incident photon can excite an electron-hole pair with energy $\hbar\omega'$ and momentum q' only if energy and momentum are conserved.

In the case of impurity-assisted absorption the additional momentum is absorbed by an impurity with no change in the energy of the impurity. This process is also known as elastic scattering, since no energy is transferred to the

impurity excitation. Absorption of light in an impure system can therefore occur at any frequency of incident light. The optical conductivity for this process is simply the Drude conductivity with plasma frequency ω_p and impurity scattering rate $1/\tau$ given by

$$\sigma(\omega) = \frac{\omega_p^2 \tau}{4\pi} \frac{1}{1 - i\,\omega\,\tau} \,. \tag{1.4}$$

In the superconducting state the creation of an electron-hole pair cannot occur until a Cooper pair is liberated from the superconducting condensate, which places a threshold on the onset of absorption at 2Δ. Note that in a clean superconductor $2\Delta >> 1/\tau$. In this case the absorption onset is not directly visible.

In the case of excitation-assisted absorption, momentum of the excited electron-hole pair is conserved by the presence of some excitation. This process is also known as inelastic scattering, since energy is also transferred to the excitation. Excitation-assisted absorption can only occur at the characteristic excitation energies of the system. In conventional systems the excitation is usually a phonon. For the case of phonon excitations, this process is known as the Holstein effect.[33] For the case of Pb,[34] the absorptivity spectrum was observed to mimic the excitation density of states since the absorptivity increases as more phonons are available to scatter.

In the superconducting state, the electron quasiparticles need to be liberated from the Cooper pairs which compose the superconducting condensate. Excitation assisted absorption which in the normal state occurs at a frequency ω will therefore occur at a frequency $2\Delta + \omega$ in the superconducting state.

1.2.3. Oscillator Strength

The oscillator strength is a quantity useful for understanding the behavior of the response function $\sigma(\omega)$. The total oscillator strength can be expressed as

$$\mathcal{A} = \int_0^\infty \sigma_1(\omega)d\omega = \frac{\pi}{2}\frac{ne^2}{m} \tag{1.5}$$

where n is the total carrier density, e and m the effective charge and mass, respectively, of the charge carriers and $\omega_p = (4\pi ne^2/m)^{1/2}$ is the plasma frequency. The quantity $\mathcal{A}$ depends only on the intrinsic parameters n, e and m and therefore is conserved independent of extrinsic factors such as temperature or magnetic field. In the superconducting state charge carriers condense into the superconducting ground state, which mathematically manifest itself as a delta function in the conductivity at $\omega = 0$.[35] In fact, it can be shown from the Kramers-Kronig relations that the London conductivity $\sigma_2(\omega) = n_s e^2/m\omega = c^2/4\pi\lambda^2\omega$ leads to a term $\sigma_1(\omega) = \delta(\omega)(c^2/8\lambda^2)$.[36] We can define

$$\mathcal{A}_n = \int_{0^+}^\infty \sigma_1(\omega)d\omega = \frac{\pi}{2}\frac{n_n e^2}{m} \tag{1.6}$$

$$\mathcal{A}_s = \frac{\pi}{2}\lim_{\omega\to 0}\omega\sigma_2(\omega) = \frac{\pi}{2}\frac{n_s e^2}{m}\ , \tag{1.7}$$

corresponding to the oscillator strength of the normal and superconducting charge carrier densities n_n and n_s, respectively, so that $\mathcal{A} = \mathcal{A}_s + \mathcal{A}_n$. This result will be discussed more in Chapters 3 and 6.

1.3. Kramers-Kronig Analysis

The Kramers-Kronig (KK) relations give us a technique for determining the complex conductivity $\sigma(\omega)$ from measurements of the reflectivity $R(\omega)$, or equivalently the absorptivity $A(\omega) = 1 - R(\omega)$. The KK relations are based on the fact that the complex response function of any linear, passive, causal system is analytic in the upper half plane (for $e^{-i\omega t}$ time dependence of the field), viewed as a function of the complex frequency ω. The physically profound consequence of this mathematical fact manifests itself as the relationship between the real and imaginary components of the complex response function. The real and imaginary parts of the complex response function are related mathematically through Cauchy's integral theorem.

The response function we need to consider for our optics measurements is the complex reflection coefficient $r(\omega)$ defined by

$$r(\omega) \equiv R(\omega)e^{i\theta(\omega)} = \frac{\frac{4\pi}{c} - \dot{Z}(\omega)}{\frac{4\pi}{c} + Z(\omega)}, \qquad (1.8)$$

where $R(\omega)$ is the amplitude and $\theta(\omega)$ is the phase of the reflection coefficient. The expression on the right side of Eq. 1.8 relates the reflection coefficient $r(\omega)$ to the impedance $Z(\omega)$ of a medium in the case where radiation is incident normal to the medium. The phase function $\theta(\omega)$ is given as[37]

$$\theta(\omega) = -\frac{\omega}{\pi} \mathcal{P} \int_0^\infty \frac{\ln R(\omega')\, d\omega'}{\omega'^2 - \omega^2} . \qquad (1.9)$$

We can rewrite this expression eliminating the principal value and also eliminating the singularity at $\omega = \omega'$ as[38]

$$\theta(\omega) = -\frac{\omega}{\pi} \int_0^{\infty} \frac{[\ \ln R(\omega') - \ln R(\omega)\ ]d\omega'}{\omega'^2 - \omega^2}. \qquad (1.10)$$

Calculating $\theta(\omega)$ from $R(\omega)$ defines the complex reflection coefficient $r(\omega)$, which can then be used to determine $\sigma(\omega)$.

In principle, the KK technique requires a knowledge of the reflectivity $R(\omega)$ at all frequencies. In all practical cases the reflectivity is measured over some finite frequency interval $\omega_{low} < \omega < \omega_{high}$ and extended to zero and infinite frequencies by suitable extrapolations. The integral in Eq. 1.10 is done analytically over the frequency intervals $[0,\omega_{low}]$ and $[\omega_{high},\infty]$ using the low and high frequency extrapolations, respectively, and discretely over the frequency interval $[\omega_{low},\omega_{high}]$ using the measured data. From Eq. 1.10 it is clear that the choice of the high frequency extrapolation will affect the overall level and not the shape of $\theta(\omega)$ at low frequencies. The choice of low frequency extrapolation affects the shape of the deduced $\sigma(\omega)$ in the vicinity of the extrapolation. In Chapter 3 we have studied the effects of the low frequency extrapolation on the inferred conductivity $\sigma(\omega)$ for the case of the cuprate superconductors.

Often in addition to knowing the real part of the reflection coefficient at low frequency one has available both the real and imaginary components of the reflection coefficient from some high frequency measurement. For example, ellipsometric techniques can determine the complex reflection coefficient in the vicinity of several eV. We can use both $R_{hifreq}(\omega)$ and $\theta_{hifreq}(\omega)$ from this high frequency measurement to determine the complex

reflection coefficient at low frequencies.[39] The uncorrected phase function $\theta_{uncorr}(\omega)$ is first determined from the KK transform of the data using the high frequency reflectivity data $R_{hifreq}(\omega)$. It can be shown[39] that the difference function $\Delta\theta(\omega) = \theta_{hifreq}(\omega) - \theta_{uncorr}(\omega)$ is an analytic function of frequency and can be expandable into a series containing only odd powers of ω. The difference function $\Delta\theta(\omega)$ can fitted to the polynomial $P(\omega) = a_1\omega + a_2\omega^2 + ... + a_{2m+1}\omega^{2m+1}$ where m is typically between 10 and 20. The corrected phase function is then obtained as $\theta_{corr}(\omega) = \theta_{uncorr}(\omega) + P(\omega)$, and is used to compute $\sigma(\omega)$. This technique was used to obtain $\sigma(\omega)$ for the BKBO samples studied in Chapter 5, where we had available to us ellipsometric data between 1.3 and 4.5 eV.[39]

1.4. Eliashberg Strong Coupling Calculation

We have used an Eliashberg strong coupling calculation[40] to model the residual losses of Nb and $Ba_{0.6}K_{0.4}BiO_3$ thin films. This work is contained in Chapters 2 and 6, respectively. The Eliashberg strong coupling calculations used in this thesis were done by Dr. E. J. Nicol at U. C. Santa Barbara.

The Eliashberg strong coupling calculation is done in the local, non-retarded limit. A Green's function approach is used to calculate the optical conductivity resulting from impurity- and excitation- assisted absorption processes occurring in the superconducting state. The impurity scattering mechanism is described by a phenomenological impurity scattering rate $1/\tau_i$ and by the oscillator strength of the free carriers, given by the plasma frequency ω_p. The dominant excitation mechanism is assumed to be electron-phonon scattering as described by the coupled electron-phonon $\alpha^2(\omega)F(\omega)$ spectrum, where $\alpha^2(\omega)$ is the electron-phonon matrix element and $F(\omega)$ is the

phonon density of states. For convenience of notation, we will write $\alpha^2F(\omega)$ instead of $\alpha^2(\omega)F(\omega)$.

The input to the calculation is the plasma frequency ω_p, the critical temperature T_c, the $\alpha^2F(\omega)$ spectrum and the impurity scattering rate $1/\tau_i$. The quantities ω_p and T_c are known. We use $\alpha^2F(\omega)$ spectra taken from the literature determined from inversion of the gap equations using the I-V characteristics from tunneling measurements.[41] The impurity scattering rate $1/\tau_i$ is a fitting parameter. The screened Coulomb potential μ^* and mass enhancement factor $m^*/m = 1 + \lambda$ are determined from T_c and $\alpha^2F(\omega)$.[42]

We assume that the electrodynamics are in the local limit for the systems we have studied. The validity of this assumption is checked self-consistently by examining the impurity scattering $1/\tau_i$ rate determined by the fits of the model to the data. The quantity of interest is $l/\delta \sim v_F\tau_i/\lambda$ where l is the electronic mean free path, v_F is the Fermi velocity and where we have made the assumption that the skin depth δ is a good approximation to the penetration depth λ in the superconducting state. In all cases we have studied the quantity l/δ determined in this way is less than unity, indicating that our assumption of local electrodynamics is justified.

2. Experimental Approach

In order to make a direct measurement of the absorptivity of high-T_c films we have used the film itself as the absorbing element in a composite bolometric far infrared detector.[43] The detector with the high-T_c absorbing film is used in conjunction with a Michelson interferometer in order to measure the spectral response of the film at submillimeter frequencies, using the technique of Fourier Transform Spectroscopy (FTS). This chapter contains a description of all the techniques used in this experiment.

2.1. Bolometers

This section contains a review of bolometer theory as well as a complete analysis of a typical bolometer used in the direct absorption experiment. In what follows we are not concerned with optimizing the response of the bolometer *per se*, but are rather attempting to use the bolometer as a tool for measuring the absorptivity of high-T_c thin films.

2.1.1. Elementary Bolometer Theory

There are several excellent outlines of bolometer theory.[44,45] In this section I will describe only the essential elements of bolometer theory relevant to my measurement.

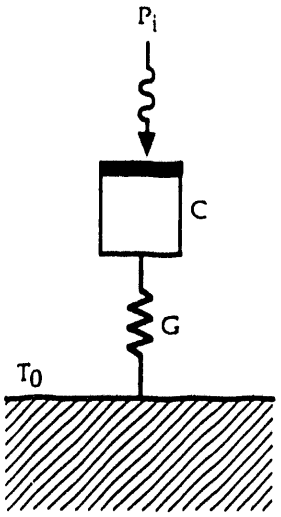

Fig. 2.1 - The basic components of a bolometer. Radiation P_i is incident on and some fraction is absorbed by an absorber (black region) which is part of a substrate with total heat capacity C. The substrate is attached to a heat sink held at a fixed temperature T_0 through a thermal conductance G. The temperature is monitored by a thermistor which is attached to the substrate, not shown. In our experiment, the radiation absorber is the high-T_c film.

A bolometer is a thermal infrared detector which utilizes an electrical resistance thermometer, or thermistor, to monitor the temperature of the radiation absorber. The basic elements of a bolometer are shown in Fig. 2.1. Radiation P_i is incident on and some fraction is absorbed by the radiation absorber (black region) which is part of a substrate with total heat capacity C. The substrate is attached to a heat sink held at a fixed temperature T_0 through a thermal conductance G. Radiation absorbed by the absorber is thermalized in the substrate. The temperature is monitored by a thermistor which is

attached to the substrate, not shown. In our experiment, the radiation absorber is the high-T_c film.

The two equations needed to understand the behavior of this thermal circuit are the diffusion and the continuity equations describing heat flow through a medium with thermal conductivity K and heat capacity per unit volume C :

$$\mathbf{J} = -K \nabla T \tag{2.1}$$

$$\nabla \cdot \mathbf{J} + \frac{\partial \rho}{\partial t} = \nabla \cdot \mathbf{J} + C \frac{\partial T}{\partial t} = 0 \tag{2.2}$$

$$D \nabla^2 T = \frac{\partial T}{\partial t} \ . \tag{2.3}$$

The third equation is a combination of the first two equations, and is known as the heat conduction equation, with thermal diffusivity $D = K / C$.

There are several approximations which simplify our understanding of these equations for our simple bolometer. The first approximation is that the thermal mass is isothermal. A characteristic decay length associated with solutions to the heat conduction equation is given by $l = (D / \pi f)^{1/2}$, where f is the driving frequency of the modulated temperature wave. (In this paper I will reserve the variable f to correspond to an acoustic modulation frequency, and ω will correspond to an optical frequency). At the operating temperature of our bolometers, typically T ~ 1.5 K and for typical substrate used (e.g., saphire), D ~ 10^3 cm^2 s^{-1} corresponding to l ~ 5 cm for a modulation frequency f ~ 10 Hz. Table 2.1 contains the thermal properties of some typical bolometer materials. Since l is much larger than typical bolometer dimensions the

Material	K (W/cm-K)	C (J/gm-K)[c]	ρ(gm/cm^3) [b]	C (J/cm^3-K)
Cu	2.0×10^0 [a]	0.84×10^{-6}	9.0	7.5×10^{-6}
Brass	$15. \times 10^{-3}$ [a]	21.0×10^{-6}	8.7	0.18×10^{-3}
Nylon	0.8×10^{-3} [a]	....	1.1	....
Al_2O_3	0.3×10^0 [a]	$13. \times 10^{-6}$	4.0	50.0×10^{-6}
MgO	2.5×10^0 [c]	8.3×10^{-6}	3.6	$30. \times 10^{-3}$
$SrTiO_3$	3.0×10^{-3} [c]	0.3×10^{-3}	4.8	1.6×10^{-3}

(a) From Ref. [68]
(b) From Ref. [69]
(c) From Ref. [70]

Table 2.1 - Thermal properties of some selected materials at 1.5 K. The heat capacity for Cu ($SrTiO_3$) is extrapolated from its 10 K (60 K) value using an approximately T^3 ($T^{1.5}$) dependence.

substrate is effectively isothermal and has a lumped heat capacity $C = V\,C$, where V is the volume of the substrate. The second approximation is that the thermal conductivity K is independent of temperature so that the temperature gradient in the thermal lead $G = K\,A/L$ varies linearly with distance, where A and L are the cross sectional area and length, respectively, of the thermal lead.

Given these approximation, equations 2.1 - 2.3 are one dimensional. We can express the power absorbed by the bolometer P, substrate temperature T and thermistor resistance R as

$$P = P_{dc} + P_{ac}\, e^{-i\,2\pi f t} \quad ,$$

$$T = T_{d\,c} + T_{ac}\, e^{-i\,2\pi f t} \quad ,$$

$$R = R_{dc} + R_{ac}\, e^{-i\,2\pi f t} \quad ,$$

using complex phasor representation. Equation 2.2 can then be written as

$$G\,(T_{dc} - T_0) = P_{dc} + I^2 R_{dc} \quad , \qquad (2.4a)$$

$$G\,T_{ac} - i\,2\pi f C\,T_{ac} = P_{ac} + I^2 R_{ac} \quad , \qquad (2.4b)$$

where we have included a source term in the continuity equation for the absorbed optical power P and electrical power I^2R which is dissipated in the thermistor and absorbed by the substrate. Equations 2.4(a) and 2.4(b) determine the dc and ac operating temperature of the bolometer, respectively.

2.1.2. Bolometer Responsivity and NEP

Two important figures of merit describing the performance of bolometers are the responsivity $S(f)$ and the Noise Equivalent Power (NEP). The responsivity $S(f)$ is the amplitude of the thermistor voltage response to the absorbed power, and can be written as

$$S(f) = \left|\frac{\partial V}{\partial P}\right| = \left|\frac{I\,R_{ac}}{P_{ac}}\right| = \frac{\alpha\, I\, R_{dc}}{G}\,\frac{1}{\sqrt{1 + (2\pi f \tau)^2}} \quad . \qquad (2.5)$$

I is the constant bias current through the thermistor, R is the electrical resistance of the thermistor, $\alpha = \frac{1}{R}\frac{\partial R}{\partial T}$ is a property of the thermistor evaluated at the operating temperature T and $\tau = C/G$ is the time constant of the detector. In general, $S(f)$ can be written a complex response function, but we are only concerned with the amplitude response here. We have neglected feedback effects, which are negligible under our operating conditions.[45] $S(f)$ has the form of a single pole rolloff function with characteristic time constant τ. Modulating, or chopping the radiation incident onto the detector at a frequency f for which $2\pi f \tau << 1$ leads to a frequency independent

responsivity $S(f) \sim \alpha V / G$. At frequencies f for which $2\pi f \tau >> 1$, $S(f) \sim \alpha V / 2\pi f C$, and the responsivity rolls off as $1/f$, and inversely proportional to C.

Another figure of merit for the bolometer is the NEP, or the Noise Equivalent Power, which is defined as the signal power required to obtain a signal equal to the noise in a one Hz bandwidth. The NEP is given by

$$NEP^2 = 8 k_B T \varepsilon P_B + 4 k_B T^2 G + \frac{4 k_B T R}{S^2} + \frac{V_n^2}{S^2} + \frac{V_{mic}^2}{S^2} + \frac{V_{1/f}^2}{S^2} , \qquad (2.6)$$

where k_B is Boltzmann's constant. The first term on the right is noise from the background power loading due to photon fluctuations associated with the incident radiation εP_B; the second term to thermal fluctuation noise associated with the thermal conductance G at temperature T; the third term is the Johnson noise due to the thermistor or resistance R at temperature T ; V_n is amplifier noise; V_{mic} is microphonic noise and $V_{1/f}$ is a phenomenological term used to describe noise with a $1/f$ characteristic spectrum. Voltage noises are expressed as power noise by scaling with the electrical responsivity. The first three terms are fundamental thermodynamic limits to the NEP. The various contributions to the NEP are not correlated, and so add in quadrature.

2.1.3. Detector Noise

Contributions to the NEP for the bolometric detectors used in this experiment are given in Table 2.2. Photon noise is due to radiation from a room temperature blackbody emitter through a 700 cm^{-1} cutoff lowpass filter cooled to 1.2 K. The radiation throughput is $A\Omega \approx 0.03$ sr-cm^2. The dominant sources of noise in our bolometric detectors are Johnson and amplifier noise. Johnson noise is discussed in most elementary thermodynamic textbooks.[46]

Electrical:	$R(T) = R_0 \exp(A / T^{1/2})$	$NEP_{Johnson} = 2 \times 10^{-13}$ W $Hz^{-1/2}$
(NTD#4)	$A = 9.2$	
	$R_0 = 490\ \Omega$	
	$T = 1.5$ K	
	$\alpha(T = 1.5\ K) = -6.9$	
	$R(1.5\ K) = 0.9\ M\Omega$	
	$R_L = 4\ M\Omega$	
	$I^2R = 400$ nW	
Background:	$\omega_{cutoff} = 700\ cm^{-1}$	$NEP_{photon} = 1 \times 10^{-14}$ W $Hz^{-1/2}$
	$A\Omega \approx 0.03$ sr-cm^2	
	$P_{dc} \approx 1\ \mu W$	
Thermal:	$f = 6$ Hz	$NEP_{thermal} = 4 \times 10^{-14}$ W $Hz^{-1/2}$
	$\tau = 100$ ms	
	$G = 10\ \mu W/K$	
	$C = 1\ \mu J/K$	
	$S(f = 6Hz) = 5 \times 10^4$ V/W	
Amplifier:	$e_n = 3$ nV $Hz^{-1/2}$	$NEP_{amplifier} = 1 \times 10^{-13}$ W $Hz^{-1/2}$
(TSK-147)	$i_n = 5$ fA $Hz^{-1/2}$	
		$NEP_{total} = 2.5 \times 10^{-13}$ W $Hz^{-1/2}$

Table 2.2 - Characteristics of a typical bolometer used in the direct absorptivity experiment. The thermistor is NTD #4 material described in reference [47]. Background power loading is due to a room temperature blackbody through a 700 cm^{-1} cutoff lowpass filter with throughput listed below. The temperature of the lowpass filter and the heat sink is $T_0 = 1.2$K.

Amplifier noise can be characterized by

$$V_n^2 = e_n^2 + (i_n R_s)^2 \quad , \tag{2.7}$$

where e_n and i_n are the voltage and current noise of the amplifier, respectively, with input source resistance R_s. V_s is the electrical signal across R_s. Voltage and current noises are uncorrelated so add in quadrature. An electrical circuit used for analyzing amplifier noise is shown in Fig. 2.2. The amplifier noise temperature T_n is defined as the temperature of a resistor of resistance R_s which produces an equivalent amount of Johnson noise, so that $T_n = V_n^2/(4\, k_B\, R_s)$. Values of e_n and i_n measured for the amplifier used in our experiment are given in Table 2.2. A plot of T_n versus R_s is shown in Fig. 2.3. The amplifier e_n and i_n and detector resistance R_s are chosen so that T_n is less than the detector heat sink temperature so that the amplifier noise does not dominate the NEP. The minimum T_n occurs for $R_s = e_n / i_n$.

Microphonic noise can also be a significant source of noise in our bolometric detectors. This effect is due to time varying parasitic capacitances c between the electrical leads and their surroundings. Mechanical resonances present in the electrical leads result in time varying capacitances $\partial c/\partial t$. Since $q = cV$, then $I_{mic} = \partial q/\partial t = \partial c/\partial t\, V$, where I_{mic} is the current induced in the electrical leads by the mechanical motion of the leads. V is the voltage bias across the leads. The microphonic noise $V_N \propto I_{mic}\, R_s$. Microphonic noise is strongly frequency dependent. In practice, electrical leads must be rigidly secured in order to reduce this effect. This increases the frequency and lowers the Q of the mechanical resonance.

2.1.4. Bolometer Design Considerations

In order to design a sensitive bolometer one needs to maximize the responsivity $S(f)$ and minimize the noise, or NEP. This is a complicated

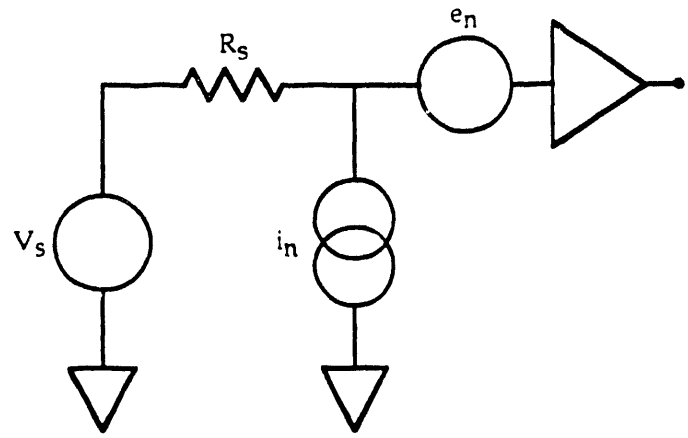

Fig. 2.2 - Electrical circuit used for analyzing amplifier noise. The quantities e_n and i_n are voltage and current noise, respectively. V_S is the signal across the source resistance R_S.

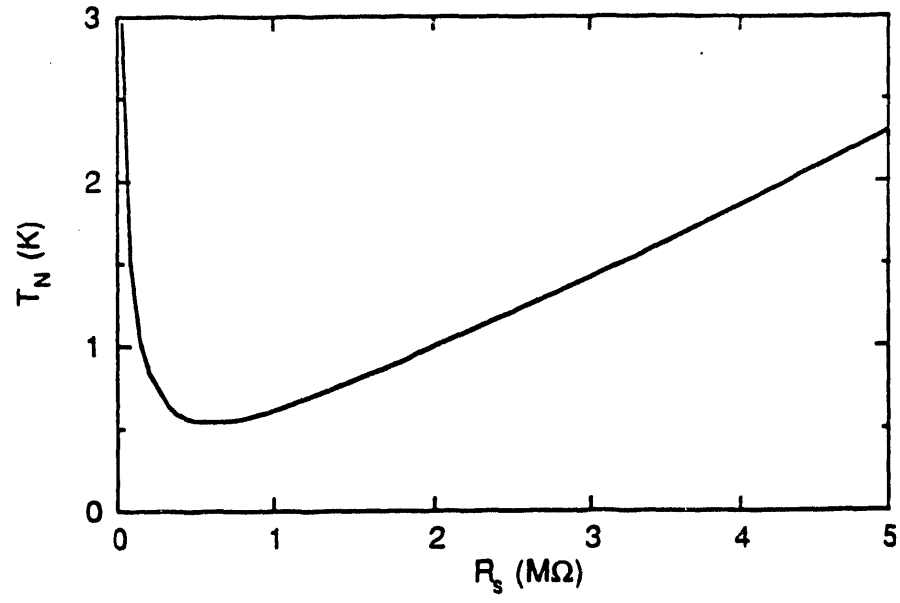

Fig. 2.3 - Amplifier noise temperature T_n versus source resistance R_S as described in the text. The minimum T_n occurs for $R_S = e_n / i_n$.

optimization problem. In general, a bolometer is optimized at a particular temperature. This is primarily due to the fact that most sensitive thermistor elements are useful only in some limited temperature range. Additionally, it is important to minimize the heat capacity of the bolometer, which in our case is dominated by the high-T_c film and substrate. The heat capacity of the bolometer can increase as fast as T^3 . At any finite operating frequency f this leads to a responsivity $S(f)$ falling off like $1/C$, leading to a large NEP. We operate our detectors at 2K, where the heat capacity of our bolometer is low and where we have available to us sensitive thermistor elements. The thermistors are made from neutron transmutation doped (NTD) germanium[47] which are doped near the metal insulator transition. Electrical properties of a typical thermistor are given in Table 2.2. This choice of operating temperature allows us to study the residual, low temperature losses of the superconducting films.

2.1.5. Design of a Typical Bolometer

The bolometers used in our measurement are not globally optimized. Rather the optimization of a typical bolometer used in our measurement is driven by our choice to operate at pumped LHe temperatures and by the availability of a laboratory standard, low noise room temperature amplifier. We use the Toshiba TSK - 147 JFET ampifier. This is the same amplifier whose noise temperature T_n versus source impedance R_s is shown in Fig. 2.3. The input source impedance which minimizes the amplifier noise temperature is $R_s = e_n / i_n \sim 500\ k\Omega$. The bolometer base temperature is ~ 1.2 K. In order that the bolometers we use are not amplifier noise limited the amplifier noise temperature T_n must be at or below the bolometer base temperature, corresponding to a source impedance of close to 500 kΩ. It is

reasonable to operate the detector at a temperature approximately 25 % above the base temperature. Therefore we must use a thermistor with a resistance of ~ 500 kΩ at a temperature of ~ 1.5 K. The neutron-transmutation-doped germanium thermistor NTD #4 is an excellent candidate for our application.[47] We have used this NTD #4 material for all of our bolometers. The thermal conductivity G of the bolometer is chosen to satisfy the above constraints on the operating temperature given the background power loading P_{dc}.

In this section and in Table 2.2 we completely describe a typical bolometer used in our measurement. This bolometer uses a highly reflective high-T_c thin film as the absorber and is optimized given the constraints due to the choice of base temperature and amplifier, as described above. Given this information, it is possible to adjust the thermal conductance G of the bolometer if the operating condition of the bolometer is varied. The bolometer described below and in Table 2.2 is optimized for viewing radiation from 0 to 700 cm^{-1}. For example, if one wishes to use the bolometer to view radiation over some other spectral band or if the throughput changes then the background power loading P_{dc} will change. The thermal conductance G of the bolometer must then be adjusted so that the operating temperature T ~ 1.5 K remains the same. Since $P_{dc} \sim G\Delta T$, if P increases (decreases) G must increase (decrease). To first order this modification of G will account for any changes in the operating conditions of the bolometer.

A typical bolometer used in this experiment consists of a 125 μm thick by 5 × 5 mm^2 Al_2O_3 substrate which is suspended in a thermal vacuum by 100 μm diameter nylon threads. A small neutron-transmutation-doped (NTD#4) germanium thermistor[47] and NiCr resistor[48] are glued to one surface of the Al_2O_3 substrate, as shown in Fig. 2.4. The thermistor is used to

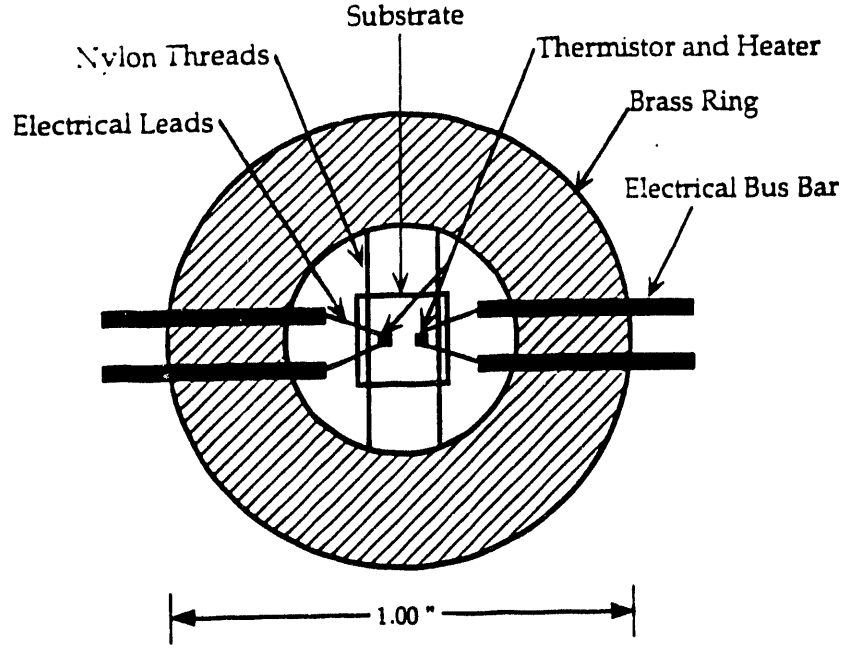

Fig. 2.4 - Schematic of a typical bolometer used in this experiment as discussed in the text. The absorbing film is on the side of the substrate opposite to that shown here. The substrate is operates in a vacuum and is thermally isolated from the brass bolometer ring, which is held at the heat sink temperature of $T_0 \sim 1.2K$.

measure the substrate temperature and the NiCr resistor is used to determine the absolute responsivity of the detector, as discussed below. The electrical connection from the thermistor to the heat sink at 1.2 K is made from 25 μm diameter copper wire. The electrical connection from the NiCr heater to the heat sink is made from 12 μm diameter brass wire. The materials are chosen so that the thermal time constant $\tau = C/G$ of the bolometer, typically 100 ms, is determined by the relatively large thermal conductance G due to the copper leads from the thermistor to the heat sink at ~1.2 K and by the heat capacity C

of the assembled bolometer. The thermal properties of materials used in the bolometer design are tabulated in Table 2.1.

The bolometer with Al_2O_3 substrate is completely assembled before attaching the high-T_c absorbing film. The back surface of the substrate on which the high-T_c film has been deposited is glued onto the surface of the bolometer substrate without the thermistor and heater. The high-T_c films used in this study have been deposited on a variety of substrates, for example, $LaAlO_3$, $SrTiO_3$, or MgO. Typical substrate dimensions are 500 μm thick by 5 x 5 mm^2. The heat capacity of the high-T_c substrate can be an important component of the total bolometer heat capacity, especially for $SrTiO_3$, as in Table 2.1.

2.1.6. Measuring Bolometer Responsivities

In order know to the value of the power absorbed by the bolometer we need to determine the absolute value of the bolometer responsivity. The dc bolometer responsivity can be determined from the bolometer dc I-V characteristics.[45] However, this technique neglects effects of electrical bias-induced nonthermal nonlinearities in NTD germanium.[49] In addition, determining the bolometer responsivity from the dc I-V characteristics neglects effects due to thermal rolloff, which for our large time constant bolometers is appreciable.

In order to overcome these difficulties the responsivity of the bolometer at frequency f is directly measured by passing an ac current at frequency $f/2$ through a known heater resistance which is glued onto the back surface of the bolometer, as shown in Fig. 2.4. An ac current at frequency $f/2$ will dissipate power in the resistor in exactly the same way an optical signal chopped at a frequency f dissipates power in the bolometer absorber, provided

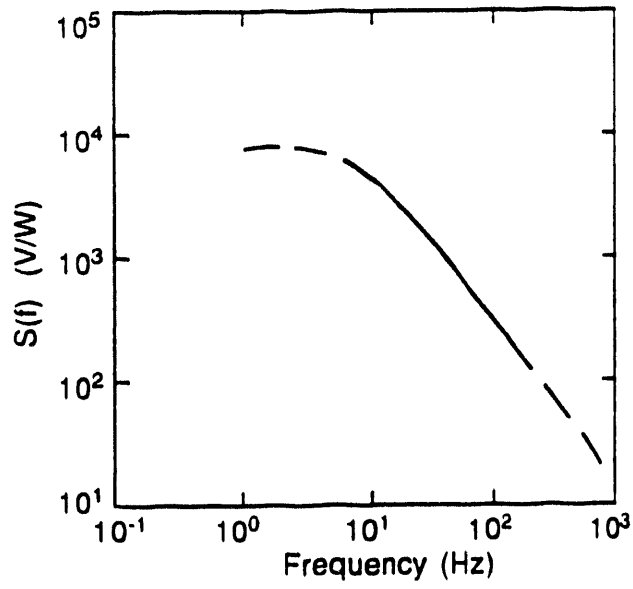

Fig. 2.5 - The measured responsivity S(*f*) of a typical bolometer used in this experiment. The optical response of the bolometer to incident radiation (solid line) agrees with the electrical response of the bolometer to power input to the heater (dashed line).

that at the frequency *f* the thermal time constant τ of the bolometer is dominated by the heat capacity C of the bolometer and the thermal conductivity G between the thermistor and the heat sink. Measuring the ac signal across the bolometer δV and the known ac power across the heater δP determines the responsivity $S(f) \sim \delta V/\delta P$.

The frequency dependence of the response to an ac current through the heater and to chopped infrared radiation are both measured to confirm that all internal thermal relaxation times in the bolometer are much shorter than $\tau = C/G$. Typical results are shown in Fig. 2.5. The optical response (solid line) can only be modulated down to 6 Hz, below which the chopper becomes unstable. The electrical response (dashed line) is measured after turning off the chopper so that the chopper blade covers the light pipe and by passing an

ac voltage across the heater resistor. The electrical response can be measured to low frequencies (~1 Hz) in order to confirm the shape of the thermal response. The slight deviation from a frequency independent response seen in the electrical response in Fig. 2.5 arises because of the frequency dependent gain of the amplifier.

Using numerical modelling we have shown that as long as the measured electrical response of the bolometer is independent of frequency over some low frequency region and rolls off like $1/f$ above some characteristic frequency f_0 then the dominant relaxation rate of the bolometer is $\tau^{-1} = G/C = f_0$. Operating the bolometer for any chopping frequency such that the response falls off at or slower than $1/f$ is therefore dominated by the known relaxation rate τ^{-1}.

2.1.7. Measuring the Response of an Arbitrarily Complicated Thermal Circuit

The response of an arbitrarily complicated thermal circuit can be solved by generalizing Eq. 2.4. For a thermal circuit with N thermal masses, this requires inverting an N x N matrix to solve for the temperature at a given thermal element given some power input. We have the analyzed the three element thermal circuit shown in Fig. 2.6, which can be represented by the matrix:

$$\mathbf{M} = \begin{pmatrix} i\omega C_1 + G_1 + G_3 & -G_1 & 0 \\ -G_1 & i\omega C_2 + G_1 + G_2 & -G_2 \\ 0 & -G_2 & i\omega C_3 + G_2 \end{pmatrix}.$$

The temperature vector **T** can be expressed in terms of the input power vector **P** by $\mathbf{T} = \mathbf{M}^{-1}\,\mathbf{P}$. The form of the matrix **M** given above can be quickly generalized to any arbitrarily complicated thermal circuit. In general, the

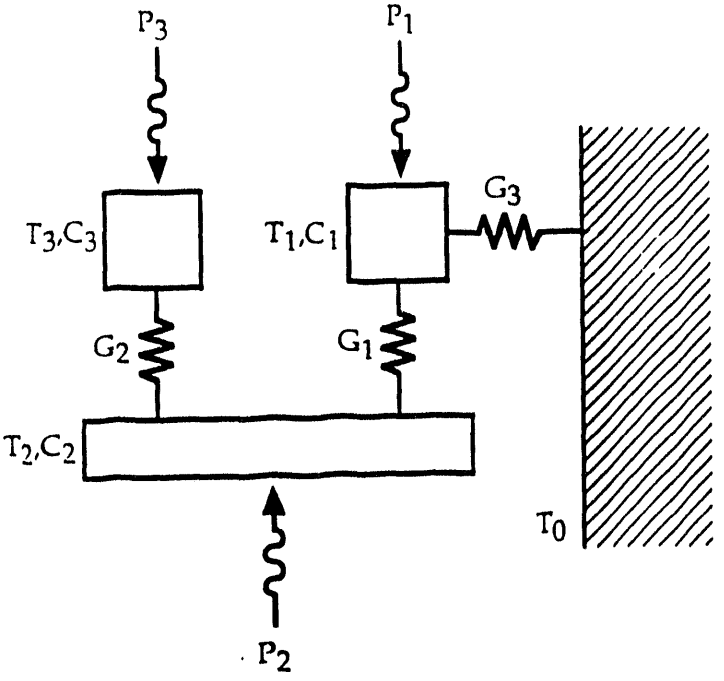

Fig. 2.6 - A three element thermal circuit used to model the thermal response of our bolometric detectors. This circuit represents a typical bolometer used in our experiment. Element 1 represents the thermistor; element 2, the high-T_c film/substrate; element 3, the heater.

responsivity $S(f)$ versus frequency f will exhibit N poles in some complicated way, depending on where power is input into the circuit and where the temperature is monitored.

The thermal circuit we have chosen to analyze in Fig. 2.6 represents a typical bolometer used in our experiment. Element 1 represents the thermistor; element 2, the high-T_c film/substrate; element 3, the heater. Through numerical simulations we have shown that if $\tau = C_2/G_3$ is the longest time constant in the thermal circuit then the temperature response at the thermistor (element 1) is independent of whether power is input optically (through element 2) or electrically (through element 3), provided the

measured electrical and optical responses are not falling off faster than $1/f$. If the response of the bolometer is independent of whether power is input optically or electrically then we are able to directly measure the absolute responsivity of the bolometer by delivering a known amount of power through the heater resistor and measuring the bolometer response.

2.2. Spectroscopic Techniques

We have used a Michelson Interferometer along with the technique of Fourier Transform Spectroscopy (FTS) to obtain broad band spectral information about high-T_c superconducting samples. The power of this technique can be seen in comparison to grating spectroscopy. The most significant advantage of FTS over grating spectroscopy is the enhancement of signal to noise ratio in the measured spectrum. This can be understood by considering spending time T observing the broadband spectrum of interest divided into N resolvable elements. The grating monochrometer spends a time T/N time observing each resolvable spectral element, while the interferometer spends a total time T observing all spectral elements simultaneously. The interferometer gains a factor N in integration time per spectral element. If the noise is independent of the signal, the spectrometer therefore has a signal-to-noise ratio improvement over the grating monochrometer of $N^{1/2}$. Because the interferometer modulates the incident radiation, the actual improvement in available signal to noise is $N^{1/2}/2$. This is known as the multiplex, or Fellgett advantage.[50]

2.2.1. Fourier Transform Spectroscopy

Fourier Transform Spectroscopy is a well established technique[51] so only a brief description will be given here. Collimated broadband radiation in

a Michelson Interferometer is split into two beams and recombined, with the radiation in one of the arms allowed to travel a distance δ farther by moving the mirror in the arm by $\delta/2$ along the beam propagation direction. If the intensity distribution of the source is $H(\nu)$, with ν the frequency in wavenumbers, and the intensity distribution of the interferometer as a function of path difference is $B(\delta)$, then $H(\nu)$ and $B(\delta)$ are related by Fourier transforms, e.g.,

$$H(\nu) = \int_{-\infty}^{+\infty} h(\delta) e^{i 2\pi \nu \delta} \, d\delta$$
$$h(\delta) = \int_{-\infty}^{+\infty} H(\nu) e^{-i 2\pi \nu \delta} \, d\nu \quad , \tag{2.8}$$

where $h(\delta) = B(\delta) - B(0)/2$ is called the interferogram. It can also be shown that the inverse Fourier Transform of the autocorrelation function of the electric field amplitude as a function of position is the power spectrum. This statement is known as the Wiener-Khinchine Thorem.

In practice one samples the interferogram at a number of regular, discrete intervals around $\delta = 0$. This can be done either by moving the mirror at a constant velocity v_{mirror} and sampling at discrete time intervals or by discretely stepping the mirror and sampling the interferogram. With the former "scanning" technique, radiation at a frequency ν will appear at the detector modulated with frequency $f = 2 v_{mirror} \nu$. For a detector with a single pole rolloff and time constant τ this requires τ such that $2 \pi f \tau << 1$ so that the detector has uniform response to the incident broadband radiation. With the latter "step and integrate" technique, the radiation is modulated not by the motion of the mirror but rather by a chopper blade operated at a fixed frequency f so that the frequency response of the detector is largely irrelevant to the acquisition of the interferogram. Because of the relatively large time

constants of our detectors the "step and integrate" technique is used in this experiment.

The discrete sampling and the truncation of the interferogram has several important effects on the calculated spectrum:

(A) If the size of the discrete mirror step is δ_0 then radiation at $\nu_c = (2\,\delta_0)^{-1}$ is "critically sampled," that is, radiation at frequencies higher than ν_c, known as the Nyquist critical frequency, appears in the spectrum at a lower frequency. The precise way in which this occurs can be seen as follows. Sampling the continuous interferogram at discrete intervals is equivalent to mathematically multiplying the continuous interferogram by a series of delta functions with regular spacing δ_0. The latter is known as a "comb" function, $\perp\!\!\!\perp\!\!\!\perp(\delta;\delta_0)$, where

$$\perp\!\!\!\perp\!\!\!\perp(\delta;\delta 0) = \sum_{n=-\infty}^{+\infty} \delta\,(\,\delta - n\delta_0\,).$$

By the convolution theorem,

$$FT[\,h(\delta)\,\perp\!\!\!\perp\!\!\!\perp(\delta;\delta_0)\,] = FT[\,h(\delta)] * FT(\,\perp\!\!\!\perp\!\!\!\perp(\delta;\delta_0)\,] = H(\nu) * \perp\!\!\!\perp\!\!\!\perp(\delta;\delta_0),$$

where FT designates the Fourier transform, $FT[\,h(\delta)\,] = H(\nu)$ is the continuous spectrum, and the Fourier transform of the comb function is a comb function. The symbol " * " denotes the convolution. Therefore,

$$H_s(\nu) = H(\nu) * \perp\!\!\!\perp\!\!\!\perp(\delta;\delta 0) = \sum_{n=-\infty}^{+\infty} H(\,\nu - n\delta_0^{-1}\,),$$

where $H_s(\nu)$ is the spectrum resulting from the discrete sampling. From this it is clear that $H_s(\nu)$ must be zero for $\nu > \nu_c$ otherwise "aliasing," or the appearance of high frequency spectral weight at lower frequencies, will occur. In practice this means that a low pass filter which cuts off the radiation at or below ν_c must be used to avoid aliasing. Note that in the complex notation used above, $H(\nu)$ is symmetric about $\nu = 0$.

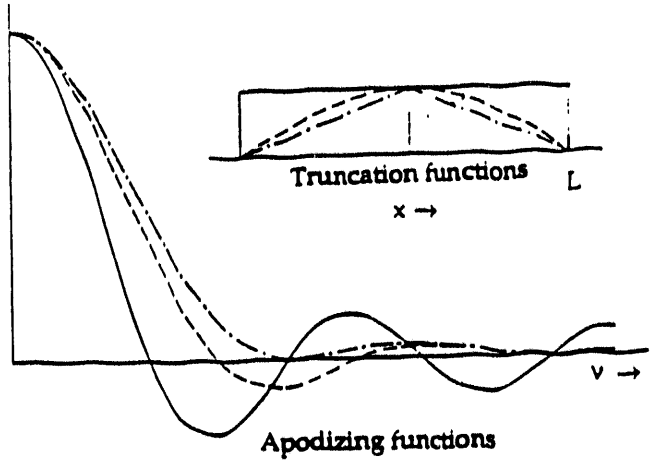

Fig. 2.7 - Several truncation functions and their Fourier transforms, or "apodizing" functions. The Fourier transform of the square wave truncation function is 2L sinc(z) = 2L sin(z)/z, where $z = 2\pi L\nu$. The Fourier transform of the triangular wave truncation function is L $\text{sinc}^2(z/2)$. The convolution of sinc(z) with a typical spectrum tends to minimally distort the spectrum along the frequency axis. However, because of its negative sidelobes, the sinc(z) function tends to distort the spectrum along the amplitude axis more than the $\text{sinc}^2(z/2)$ apodizing function. This figure is adapted from Ref. [51].

(B) Only measuring the interferogram at a finite number of points can be thought of a multiplying the interferogram measured at an infinite number of points by a truncation function. Again, by the convolution theorem, this amounts to convolving the spectrum with the Fourier transform of the truncation function. Several truncation functions and their Fourier transforms, or "apodizing" functions, are shown in Fig. 2.7.

The resolution of the spectrum is inversely related to the mirror travel L of the measured interferogram. In general, a spectral component at frequency ν will produce m constructive interference fringes in an interferogram of length 2L, with $2L = m/\nu$. The factor of two arises because a

mirror travel L results in an optical path difference 2L. If a spectral component at frequency $\nu + \delta\nu$ is at the limit of being resolved, then it will produce m+1 constructive interference fringes in the interferogram, so that $2L = (m+1)/(\nu + \delta\nu)$. Solving, we find $\delta\nu = 1/2L$.

2.2.2. Asymmetric Interferograms

Ideally, the interferogram is perfectly symmetric about $\delta = 0$. In this case it is only necessary to measure the interferogram for $\delta \geq 0$ and a simple cosine transform of the interferogram is required to compute the spectrum in Eq. 2.8. This reduces the time required to collect data, the computation time and, especially relevant for the case of small ν_c , corresponding to a large δ_0, does not require as much mirror travel. In most real cases the interferogram is asymmetric. This typically results from small differences in the optical properties between the two arms in the Michelson interferometer. For small asymmetries and when enough mirror travel is available to measure the symmetric interferogram, the RMS of the sin and cosine transforms of the interferogram will correct for this small asymmetry. However, this has the adverse affect of rectifying the noise in the spectrum.

When there is not enough mirror travel to take a double sided interferogram, or when the advantage of reduced integration time outweighs the slight interferogram asymmetry, several techniques may be used to correct for the asymmetry.[52-55] The basic technique is to measure a short, or low resolution, double sided interferogram along with a longer, higher resolution, single sided interferogram. The low resolution double sided interferogram is used to compute the phase function, which is the Arc tangent of the ratio of the sin and cosine transforms of the interferogram. The phase function is then used to correct the asymmetry of the

interferogram. A useful technique combines an asymmetric apodization function due to Mertz[55] with a computationally simple multiplicative correction to the spectrum.[52] The purpose of the asymmetry in the apodization is to minimize the effects of small zero path errors.

Although not used in this work, another useful spectroscopic technique places the sample to be measured in one arm of the Michelson interferometer, resulting in an intentionally asymmetric interferogram. The advantage of this technique, known as dispersive Fourier transform spectroscopy, is that it allows direct calculation of both the amplitude and phase of the complex reflection coefficient.[56]

2.2.3. The Michelson Interferometer

The Michelson Interferometer used in this experiment is shown in Fig. 2.8. This device was constructed by Joyce and Richards.[6] The blackbody radiation comes from a water cooled General Electric UA-3 Hg - arc lamp collimated by f/1.5 optics. The beamsplitter is a thin film of Mylar tightly stretched on a ring. After reflecting from the fixed and moveable mirrors the radiation is recombined and focused into a 7/16" ID light pipe, which conveys the radiation to the detector. The radiation is modulated by a mechanical chopper blade which can be operated from ~6 - 100 Hz so that phase sensitive detection techniques can be used. The chopper blade crosses the beam obliquely so that the detector "sees" the light pipe walls, and not its own reflection in the metallic chopper blade. The interferometer can be evacuated in order to remove water vapor, which has strong absorption lines in the infrared.

High frequency radiation is removed to avoid aliasing using either absorbing black polyethylene (graphite in a polyethylene base) or Yoshinaga[57]

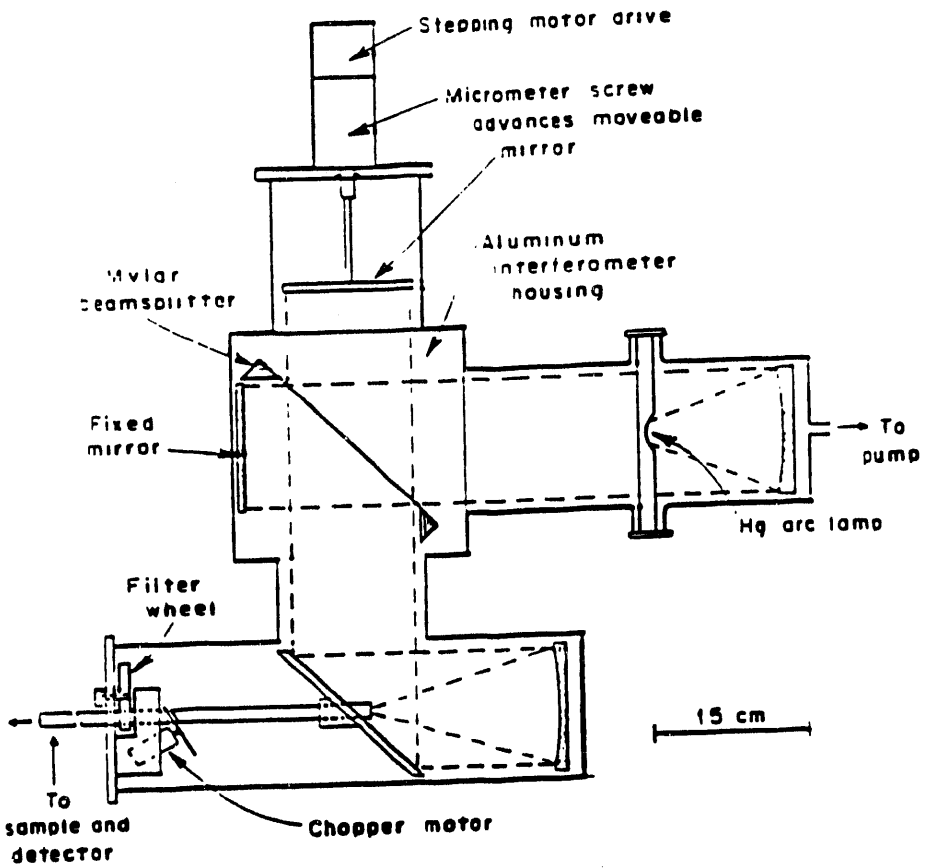

Fig. 2.8 - Schematic of the Michelson Interferometer used in this experiment. This device was constructed by Joyce and Richards.[6] The blackbody radiation comes from a water cooled General Electric UA-3 Hg - arc lamp collimated by f/1.5 optics. The beamsplitter is a thin film of Mylar tightly stretched on a ring.

filters at the output of the interferometer. The Yoshinaga filters rely on the Restrahl bands of the constituent ionic compounds to limit the transmitted radiation. Unmodulated room temperature radiation from the warm filters themselves can substantially warm the detector thereby degrading sensitivity. This unmodulated radiation is removed by filters placed in the cryogen used to cool the detectors.

The transmission efficiency of the mylar beamsplitter in the interferometer goes approximately as $\sin^2(2\pi n d \nu)$ due to interference in the mylar of thickness d, where n is the refractive index of the mylar, $n \sim 1.4$. This can be seen by treating the beamsplitter as a low finesse Fabry-Perot etalon. In general, for a given thickness beamsplitter, there is sufficient power to do spectroscopy between $0.2\,\nu_{max}$ and $0.8\,\nu_{max}$, where $\nu_{max} = (2 n d)^{-1}$. In order to measure spectra over an extended frequency region, it is therefore necessary to use several different combinations of beamsplitters and warm and cold low pass filters.

2.2.4. Data Acquisition

A block diagram of the experiment is shown in Fig. 2.9. The chopped radiation output of the interferometer goes through a light pipe and cooled low pass filters to an evacuated can containing the bolometers, described below. The bolometer can is immersed in pumped LHe. A lock-in phase sensitive detector provides the reference signal used to drive the chopper and detects the signal from the bolometer. The lockin output signal goes to a Voltage to Frequency converter (VFC) and then to the computer, which integrates the lockin signal by counting pulses from the VFC. After integrating the signal for a time t_{int} , the computer repositions the moveable mirror by means of a stepper motor. The computer then waits for a time interval t_{wait} before integrating the signal. Because the interferometer is operated in the "step-and-integrate" mode, the time t_{wait} is constrained by the lockin RC time constant and by the lockin Q factor : $t_{wait} \geq 3\,(RC)$, $3\,(Q/(2\pi f))$ so that the detector signal from the previous mirror position has decayed by $\sim e^{-3}$. The quantity $Q/(2\pi f)$ is the time constant associated with the Q and the detection frequency f of the lockin detector.

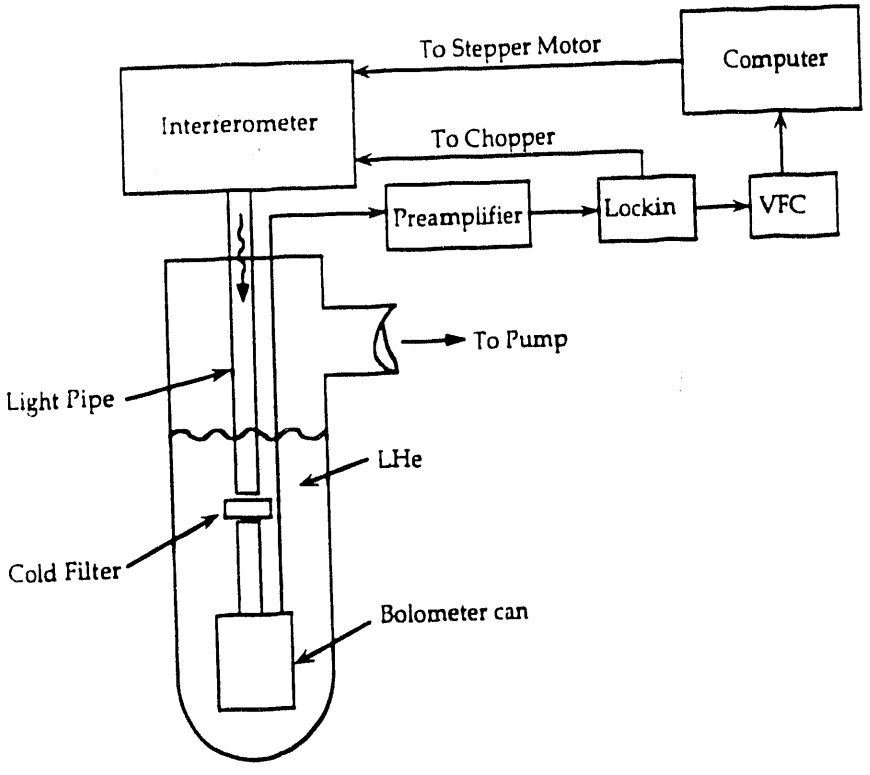

Fig. 2.9 - A block diagram of the experiment. The chopped radiation output of the interferometer goes through a light pipe and cooled low pass filters to an evacuated can containing the sample and reference bolometers. The bolometer can is immersed in pumped LHe. A lockin phase sensitive detector provides the reference signal used to drive the chopper and detects the signal from the bolometer. The lockin output signal goes to a Voltage to Frequency converter (VFC) and then to the computer, which integrates the lockin signal by counting pulses from the VFC. After integrating the signal for a time t_{int} , the computer repositions the moveable mirror by means of a stepper motor.

The VFC direct integration technique is nearly identical to repeatedly digitizing and subsequently averaging the lockin output signal, provided that the lockin signal is not undersampled, e.g., digitization must occur with period $\leq RC/3$. However, the error in the VFC integration is one LSB but

could be more in the digitization scheme. Digitization noise is negligible in this experiment.

2.2.5. Sources of Noise

Detector noise and spectrometer alignment drift are the dominant sources of noise in this experiment. Sources of detector noise up to and including the amplification stage is characterized by the NEP and was discussed previously. The detector signal-to-noise ratio can be improved by increasing the integration time t_{int} but only as $t_{int}^{1/2}$. Spectrometer alignment drift may come from differential thermal expansion of the interferometer, and is most severe when measuring data with the highest cutoff frequencies. Slow drifts in the detector heat sink temperature may be thought of as low frequency $1/f$ detector noise. Drifts with a period longer than the time required to acquire a complete interferogram correspond to a low frequency modulation of the interferogram and appear as a low frequency component of the resulting spectrum and may be insignificant. For this reason it is better to measure several interferograms rapidly rather than one interferogram slowly. Alternating sample and reference runs also minimizes the effects of slow drifts.

The effect of noise in the interferogram on the resulting spectrum can be considered by imagining the noise as some function of time which multiplies the ideal, noise-free interferogram. By the convolution theorem, the measured spectrum is the convolution of the "noise spectrum" with the noise-free spectrum.

2.3. Design of the Direct Absorption Experiment

The bolometer whose absorbing film is to be characterized is placed in the vacuum can shown in Fig. 2.9 attached to the mount shown in Fig. 2.10. The bolometer mount has positions both for a sample and reference bolometers.

2.3.1. Normalization

In order to determine the power incident on the sample detector the incident power is normalized against a reference detector with known absorptivity. Both sample and reference bolometers are attached to the mount shown in Fig. 2.10. Infrared radiation (A) chopped at 6 Hz from the Fourier transform spectrometer operated in the step-and-integrate mode passes through the light pipe and a cold low pass filter to a roof mirror (B) which divides the beam symmetrically between the sample bolometer (I) and a reference bolometer with known absorptivity (II). The aperture (C) of a thin walled brass tube (not shown) which is pressed against the absorbing film defines the throughput $A\Omega \approx 0.03$ sr-cm^2 onto each film. The absorbing film is located on the front surface of the substrate (E) which is held firmly against the exit of the throughput limiter by tension in the nylon threads (F), which are suspended from a support ring (G). The absorbing films are electrically isolated from the throughput limiters and are surrounded by infrared absorber[58] (D) to reduce stray radiation. The support ring (G) also serves as a heat sink (L) for the electrical connections (H) to the thermistor (J) and heater resistor (K). Frequency dependent asymmetries in the throughput are measured and corrected by interchanging sample and reference detectors.

The output spectrum from each detector channel can be represented by $F(\omega) = L(\omega)\, A(\omega)\, S(f)$ where ω is the frequency of light, $L(\omega)$ is the submillimeter spectrum incident on the absorbing film from the

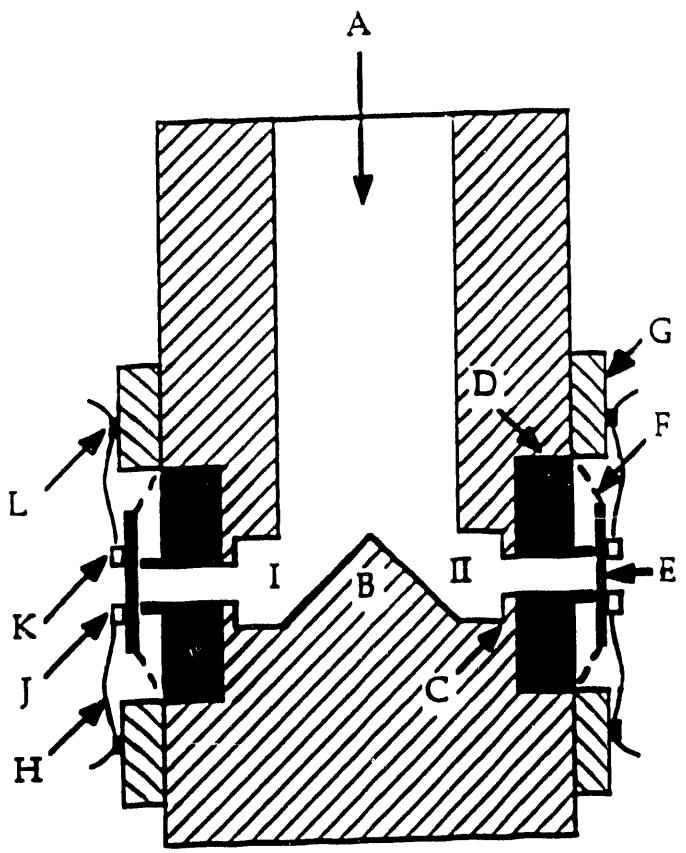

Fig. 2.10 - Cross section of the bolometer mount, which was operated in a thermal vacuum at ~1.2 K. Incident radiation A is split by roof mirror B and sent to detector channels I and II. In each channel a throughput limiter C defines the incident radiation. Stray radiation is absorbed by baffles D. The film being measured is located on the front inner surface of a substrate E which is suspended by nylon threads F from the support ring G. Thermistors J and resistance heaters K are indicated schematically. Electrical connections H to thermistors and resistors provided the thermal conductance between the substrate and the heat sinks L.

spectrometer, $A(\omega)$ is the absorptivity of the film, and $S(f)$ is the responsivity of the detector to absorbed power. If the detector responsivities and the absorptivity of the reference detector are known then the absorptivity of the sample can be determined from

$$A_s(\omega) = \frac{F_s(\omega)S_r(f)}{F_r(\omega)S_s(f)} A_r(\omega) \quad , \qquad (2.9)$$

where the subscripts s and r refer to the sample and reference channels, respectively, and where $A_r(\nu)$ is the known absorptivity of the reference absorber.

2.3.2. Characterization of the Reference Detector

The success of this experiment depends on the availability of a reference film with known absorptivity. In addition, the reference absorber should have a small heat capacity and an absorptivity comparable to that of the sample. For this reason we use a sputtered gold film. No special precautions are taken to insure the purity of the sputtered metal and so the conductivity of the film is low enough that the absorptivity can be calculated from the classical skin effect theory using the conductivity $\sigma(\omega) = \sigma_{dc} / (1 - i\omega\tau)$. Here $\sigma_{dc} = ne^2\tau/m$ is the dc conductivity of the gold film measured at 4K and τ is the momentum relaxation time inferred from σ_{dc} assuming a free electron mass and a carrier density of one electron per atom.[59]

Because of surface imperfections the optical absorptivity calculated from the bulk dc properties will underestimate the actual film absorptivity.[60] In order to correct for this effect we have measured the absorptivity of an etched brass foil relative to the gold reference. By fitting the ratio of absorptivities of brass and gold to a Drude model for each of the materials we are able to determine an effective dc conductivity and carrier density for both the brass and the gold. The use of these effective parameters should then partially compensate for the effects of surface imperfections.

The absorptivity of the brass is calculated from the classical skin effect theory using the dc conductivity of the brass measured at 4K and the carrier density estimated from a room temperature Hall coefficient measurement [61] assuming a single carrier band. We calculate the ratio of the absorptivities of brass and gold from the respective dc material properties and also from a best fit to the measured infrared ratio. The measured infrared ratio and the absorptivity ratio determined from the dc properties of the brass and gold, as well as the best fit absorptivity ratio, are shown in Fig. 2.11. A list of the dc and best fit parameters for the brass and the gold is given in Table 2.3.

The agreement between the directly measured ratio and the ratio determined from the dc properties is quite good between 30 and 650 cm^{-1}; the agreement between the directly measured ratio and the best fit is excellent over the same frequency range. Because the optical data accounts more accurately for the actual surface properties of the gold film than the simple theory, we use the absorptivity of the gold film determined from the best fit of the optical data to characterize the gold film. The correction to the frequency dependent absorptivity of the gold film varies smoothly with frequency. At 30 (700) cm^{-1} the best fit absorptivity is 3% higher (15% lower) than the absorptivity determined from the dc properties of the gold alone.

Deviations between the best fit and the absorptivity ratio in Fig. 2.11 help to establish the valid range of the optical data. The reproducibility of the data is poor above 650 cm^{-1}. This may reflect the sensitivity of the spectrometer to thermal drifts at these high frequencies. Deviations are seen below 30 cm^{-1} which appear to be due to the decreasing effectiveness of the light baffles surrounding the sample. The light baffles become transparent below ~30 cm^{-1}.[62] This effect leads to an overestimation of $A(\omega)$. Because the

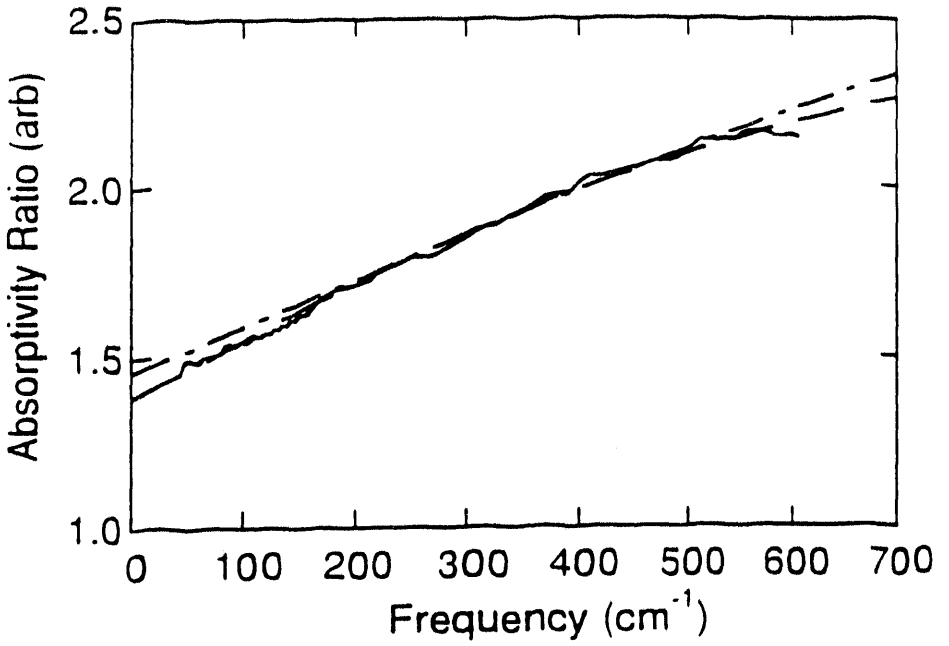

Fig. 2.11 - Ratio of the measured absorptivity of brass and gold, as described in text. The solid line is the experimental data. The dashed line is the best fit of the Drude model to the data. The dash - dot line is the fit of the Drude model using the measured dc properties of the brass and gold.

Sample	Carrier density n (10^{22} cm^{-3})		Electrical resistivity ρ (μΩ–cm)	
	dc	best fit	dc	best fit
Au	5.9	3.6	5.5	5.9
Brass	19.0	7.4	11.6	11.3

Table 2.3 - Parameters used in the Drude model for determining the absorptivities of Au and Brass.

sample and reference absorptivities are not identical this error does not cancel out when the ratio of absorptivities is calculated.

2.4. Testing the Technique: Absorptivity of Nb Thin Films

As a test of the method we have measured the absorptivity of two Nb films at 2K and fit the data to a theoretical model. These films are described in Table 2.4. The directly measured absorptivities are shown in Fig. 2.12 (solid lines). We observe the superconducting gap in both of the Nb films at ~ 25 cm^{-1} . For Nb, $2\Delta / k_B T_c = 3.8$ [63] so that $2\Delta \sim 24\ cm^{-1}$ for $T_c \sim 9K$, in agreement with our measurement. Note that we are able to clearly resolve the gap even for absorptivities less than 0.5%.

The structure observed above the gap in film B is reminiscent of structure seen in absorptivity ratios A_S/A_N measured by Joyce *et al.* for Pb films.[34] We do not understand why this structure is present in one Nb film and not the other. Structure in absorptivity ratios for Pb is due to electron - phonon coupling via the Holstein mechanism,[33] expected in a strong coupling superconductor. In order to explore whether the structure observed in sample B could be due to phonon coupling, we have compared our data to an Eliashberg strong coupling calculation[40] using $\omega_p = 7.9$ eV[64] and $\alpha^2F(\omega)$ spectra for Nb obtained from the literature.[65] The results of fitting this model to our data is shown in Fig. 2.12 (dashed lines). The $\alpha^2F(\omega)$ spectrum used in the calculation is also shown in Fig. 2.12 in arbitrary units shifted by 2Δ (dotted line). Because the electrons are bound in Cooper pairs with binding energy 2Δ, the spectrum of phonons available for electron - phonon scattering is shifted up in frequency by 2Δ. The Eliashberg calculation was done by Dr. E. J. Nicol at U. C. Santa Barbara.

Film	Institution	Thickness(nm)	RRR	R_S	T_c	$(2\pi c\tau_i)^{-1}$	τ_i / τ_{rt}
A	Conductus	250 nm	6	20 μΩ	~9 K	180 cm^{-1}	5.4
B	Yale	300 nm	3	....	~9 K	325 cm^{-1}	3

Table 2.4 - Nb films measured in this work. The microwave surface resistance R_S for sample A was measured at 4K and 10 GHz. Both films were sputtered onto fused quartz substrates. The Residual Resistivity Ratio (RRR) is the ratio of measured resistivities at room temperature and just above T_c. The impurity scattering $1/\tau_i$ rate is determined from the fit to the low temperature data, as described in the text. $1/\tau_{rt}$ is the room temperature scattering rate for Nb.

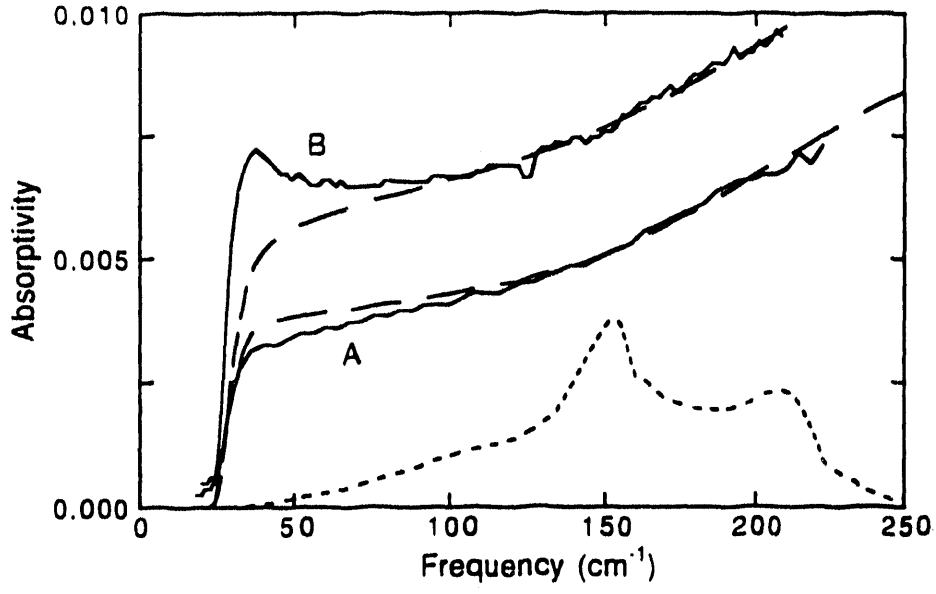

Fig. 2.12 - Measured absorptivity of two Nb films (solid lines) at 2K. These films are described in Table 2.4. Note that we are able to clearly resolve the gap even for absorptivities less than 0.5%. Also shown are best fits to the data (dashed lines) from an Eliashberg strong coupling calculation[40] using ω_p = 7.9 eV[64] and $\alpha^2F(\omega)$ spectra in arbitrary units for Nb obtained from the literature[65] shown shifted in frequency by 2 Δ (dotted line). The eliashberg calculation was done by Dr. E. J. Nicol at U. C. Santa Barbara.

The Eliashberg calculation we have used to model our data assumes local electrodynamics, e.g., $l/\delta \ll 1$, where l is the electronic mean free path and δ is the skin depth. In calculating the quantity l/δ one must consider not only electrical but also phonon emission processes, which will affect the actual skin depth δ and mean free path l.[33,66] It is the total scattering time of the electrons that is responsible for determining the ratio l/δ. The results of our modeling are consistent with our initial assumption that that the electrodynamics of our Nb samples is in the local limit. We approximate $l/\delta \sim v_F\tau_i/\lambda$ where $v_F \sim 10^8$ cm s^{-1} is an upper limit on the Fermi velocity[59], $\lambda \sim 39$ nm is the superconducting penetration depth[63] and $1/\tau_i$ is the impurity scattering rate from the best fit. From the values for the impurity scattering rate listed in Table 2.4 we estimate $l/\delta \sim 0.74$ and 0.41 for samples A and B, respectively, indicating that our assumption of local electrodynamics is reasonable.

Although we are able to fit the overall absorptivity levels for the two films, we are unable to fit the structure observed for film B. The model is however able to describe the absorption onset near 25 cm^{-1} for film A. We have also done an Eliashberg strong coupling calculation to fit the absorptivity A_s of a Pb film. A_s was deduced from the measured ratio A_s/A_n measured by Joyce *et al.*[34] and the normal state absorptivity calculated for Pb, A_n. A plasma frequency $\omega_p = 13$ eV was used with $\alpha^2F(\omega)$ taken from the literature.[67] The impurity scattering rate, discussed below, inferred from the best fit is $\Gamma_i = 90$ cm^{-1}. The measured A_s (solid line), the best fit (dashed line) and $\alpha^2F(\omega - 2\Delta)$ for Pb in arbitrary units (dotted line) are shown in Fig. 2.13. Interestingly, for the case of the Pb, the best fit overshoots the data just above the gap, opposite to the case for the Nb sample B. This apparent discrepancy may be related to our assumption of local electrodynamics in our Nb samples.

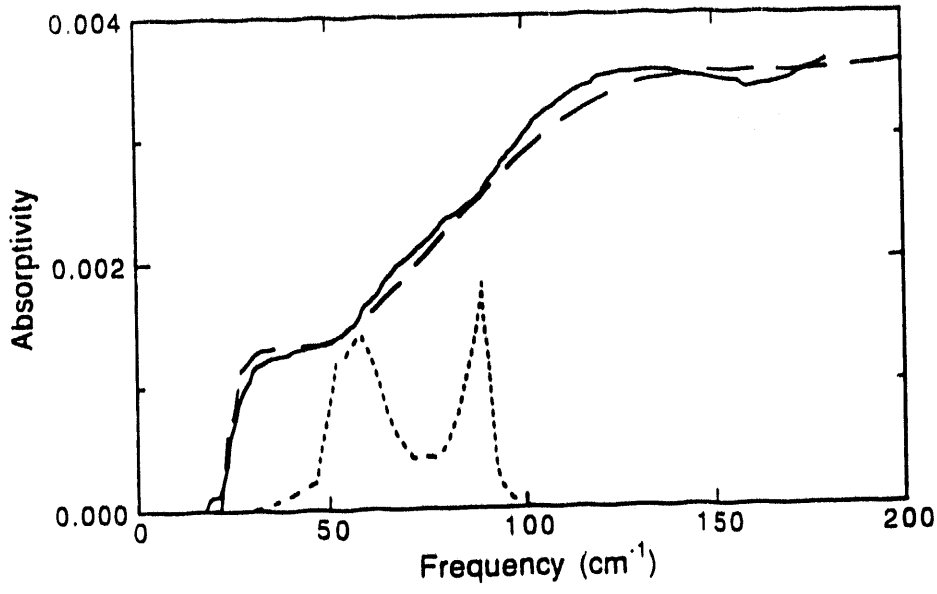

Fig. 2.13 - Absorptivity A_s of a Pb single crystal at 2K (solid line) from Joyce *et al.*[34] as described in the text. Also shown is a best fit from an Eliashberg strong coupling calculation (dashed line) using a plasma frequency ω_p = 13 eV and $\alpha^2F(\omega)$ spectrum[67] in arbitrary units, also shown shifted by 2Δ (dotted line).

The peak in the Nb $\alpha^2F(\omega - 2\Delta)$ near 150 cm^{-1} in Fig. 2.12 corresponds to an increase in the number of phonons capable of scattering with the electron quasiparticles. This additional scattering channel above 150 cm^{-1} results in a discontinuous change in the slope of the absorptivity. This increase can be clearly seen both in the measured and calculated absorptivities for sample A near 150 cm^{-1}. This feature is also present but less pronounced for sample B.

One of the parameters used to fit the data is the phenomenological impurity scattering rate, $1/\tau_i$. We can compare $1/\tau_i$ to the room temperature scattering rate, $1/\tau_{rt}$, which we can estimate from the plasma frequency ω_p =

7.9 eV[64] and from the room temperature dc resistivity for Nb,[59] $\rho_{dc} = 14.5\ \mu\Omega$ - cm, that is,

$$\frac{1}{\tau_{rt}} = \frac{\rho_{dc}\,\omega_p^2}{4\pi},$$

where c is the speed of light. From this we find $(2\pi c\tau_{rt})^{-1} = 980\ cm^{-1}$. Values of τ_i/τ_{rt} are listed in Table 2.4. The Residual Resistivity Ratio (RRR) is the ratio of dc resistivities at room temperature and just above T_c, so that the value for RRR should be equal to τ_i/τ_{rt}. Values of RRR measured for these two Nb samples are also listed in Table 2.4, and are in good agreement with the values of τ_i/τ_{rt} determined above.

In conclusion, by studying Nb films at 2K we have demonstrated that our technique is capable of directly measuring absorptivities down to as low as 25 cm^{-1} and for absorptivities much less than 1%. Calculations based on a strong coupling Eliashberg theory are in good agreement with our measurements, and scattering rates deduced from the calculation are in agreement with the measured dc properties of the Nb samples.

3. Direct Submillimeter Absorptivity Measurements on Epitaxial $YBa_2Cu_3O_7$ Films at 2K

We have measured the low temperature loss in six epitaxial a-b plane films of the high-T_c superconductor $YBa_2Cu_3O_7$ over a factor 2000 in frequency. Submillimeter measurements from 25 to 700 cm^{-1} were made at 2K by a novel direct absorption technique in which the film acts as the absorbing element in a composite bolometric detector. Microwave measurements near 10 GHz (0.3 cm^{-1}) were made on five of the same films by resonance techniques at 4K. The ~0.4 μm thick films were grown epitaxially on $SrTiO_3$, $LaAlO_3$ and MgO by off-axis sputtering and laser deposition. The absorptivities measured for all films studied are qualitatively similar, increasing smoothly with frequency, with no gap-like features below the well known absorption edge at 450 cm^{-1}. A successful three parameter fit is obtained for all of our films. This fit can be interpreted either in terms of a weakly coupled grain model or a homogeneous two-fluid model with

residual normal conductivity. The fitting parameters correspond to a grain penetration depth λ_g equal to the muon spin relaxation value of 140 nm, and to reasonable grain properties. They also give carrier densities in reasonable agreement with optically determined plasma frequencies and conductivities in agreement with a Kramers-Kronig analysis of the absorptivity data.

3.1. Introduction

One of the most studied cuprate superconductors is the $T_c \sim 90$ K material $YBa_2Cu_3O_7$ (YBCO). Almost all far infrared measurements of a-b plane oriented YBCO observe an onset of absorption at ~450 cm^{-1}.[71-78] While the amplitude of this absorption feature is strongly temperature dependent near T_c, the characteristic frequency is only weakly temperature dependent even in the neighborhood of T_c.[74] In addition, this feature is present at temperatures both above and below T_c[73] in oxygen deficient samples of this material with low T_c's. Within experimental uncertainties, the onset frequency of this feature is independent of the T_c of the sample.[73] These observations suggest that this feature is not a conventional superconducting energy gap. Another feature commonly observed in reflectivity measurements of a-b plane oriented YBCO is an onset of absorption near 140 cm^{-1} for $T << T_c$. Below this frequency the measured reflectivity is observed to be consistent with unity.[72-74,77,79] However the amplitude of this onset is comparable to the amplitude of the experimental uncertainties in these measurements, which are typically ±1%.

Measurements with polarized infrared radiation on detwinned YBCO crystals[80,81] show that the absorption is anisotropic in the a-b plane. For current flow perpendicular to the Cu-O chains, the absorption below 500 cm^{-1} is much smaller than for current flow along the chains.

Recently several groups have measured the transmissivity of thin YBCO films[82,83] in order to obtain more accurate data, especially at frequencies below a few hundred wavenumbers. Despite the complications associated with the optical properties of the substrate these experiments suggest that there is some non-vanishing fraction of normal (absorbing) carriers well below T_c. No onset of absorption is observed in these experiments below 450 cm^{-1}.[82]

Three basic interpretations have been given to the infrared data. Some workers have interpreted the frequency at which the measured reflectivity becomes consistent with unity (~ 140 cm^{-1}) with a superconducting gap.[10,11,72-74,77] For the samples with T_c = 90 K this leads to a value for the gap of $2\Delta \approx 2.2\, k_B T_c$. Others identify the 450 cm^{-1} feature with the gap,[74,77] giving $2\Delta \approx 7\, k_B T_c$ for samples with T_c = 90 K. Still others attribute the 450 cm^{-1} feature to a strong electron-phonon interaction[84] and suggest that the relaxation time is short enough in YBCO that no infrared gap should be visible.[72]

Microwave measurements show a temperature dependent component to the loss which is in reasonable agreement with the predictions of Mattis and Bardeen[85] for temperatures near T_c, e.g. T > 80K, plus a substantial residual loss that remains at low temperatures. This residual loss is minimized in high quality epitaxial a-b plane films. Both contributions to the loss vary as frequency squared from ~10 to ~100 GHz.[26]

In this paper we present submillimeter data for six well oriented films and microwave surface resistance measurements made near 10 GHz (0.3 cm^{-1}) and 4K for five of the six films. Four of these films are of high quality and are fully oxygenated. Using the well documented frequency squared dependence of the microwave loss up to 100 GHz,[26] we can infer the loss in our films over

four decades in frequency. The absorptivity varies as frequency squared up to ~ 10 cm^{-1} (300 GHz) and then approaches a constant by 450 cm^{-1} where there is a sharp onset of additional absorption. We do not observe any absorption onset at 140 cm^{-1} for any of our samples. Other investigators have explored the relationship between the residual microwave loss and the submillimeter absorptivity deduced from reflectivity measurements. Our data are generally consistent with early work,[86] but not with a recent paper which shows higher microwave losses relative to the infrared loss than we observe.[76]

A successful three parameter fit is obtained for all of our films. This fit can be interpreted either in terms of a weakly coupled grain model or a homogeneous two-fluid model with residual normal conductivity. The fitting parameters correspond to a grain penetration depth λ_g equal to the muon spin relaxation value of 140 nm, and to reasonable grain properties. They give carrier densities in agreement with optically determined plasma frequencies and conductivities in agreement with a Kramers-Kronig analysis of the absorptivity data. We use these models to phenomenologically describe the microwave and submillimeter losses in our samples below the absorption onset at 450 cm^{-1}. We do not expect these simple models to describe the absorptivity above the 450 cm^{-1} feature. Since these models are strictly valid only at frequencies below the superconducting gap, our model fitting implicitly assumes that the superconducting energy gap 2Δ, if one exists, occurs at or above 450 cm^{-1}. This analysis is consistent with the results of other workers[72-77] above ~400 cm^{-1}. Below ~400 cm^{-1} where our new data play an important role, the results of this analysis are in excellent agreement with the weakly coupled grain model fitting described above for all films, but not with the conductivity deduced from the two fluid model.

Sample	Institution	thickness (nm)	Substrate	Tc/δT (K)	Deposition Technique	R_S (μΩ)	ρ_n(300 K) (μΩ-cm)
A	Stanford	500	MgO	85 / 1.0	Off-Axis Sputter	12	195
B	Stanford	400	MgO	85 / 1.0	Off-Axis Sputter	16	260
C	Conductus	410	$LaAlO_3$	87 / 1.0	Off-Axis Sputter	30	330
D	Bellcore	500	$LaAlO_3$	92 / 0.5	Laser Ablation	48	...
E	Conductus	1250	$LaAlO_3$	87 / 2.0	Off-Axis Sputter	180	600
F	Bellcore	480	$SrTiO_3$	89 / 0.5	Laser Ablation	...	200

Table 3.1 - Samples measured in this work. Values of microwave surface resistance R_s measured at 4K near 10 GHz are scaled to 10 GHz using an ω^2 law, where ω is the microwave frequency. Superconducting transition temperatures are measured from midpoint of transition; transition widths are measured from 10 - 90 % of transition. Approximate values for the dc resistivity ρ_n measured at 300 K are listed for comparison.

3.2. Sample Characterization

The samples used in this study were fabricated by three different research groups using two different techniques, and were grown on MgO,[87] $LaAlO_3$,[88,89] and $SrTiO_3$ [89,90] substrates. A list of the samples studied is found in Table 3.1. Samples A, B, C and E were fabricated with a 90° off - axis sputtering technique from a composite YBCO target.[87,88] Substrates were attached to a substrate block heated to approximately 700° C with either a mechanical clamp or silver paste or both. Approximately 100 Watts of power on the sputter gun gave a deposition rate for the off-axis geometry of less than 0.1 Å/sec, depending on the sputtering atmosphere, which varied between 10 - 100 mTorr O_2 (or N_2O) and 40 - 300 mTorr Ar. Samples D and F were

fabricated with a laser deposition technique using a 248 nm KrF excimer laser fired at 1 Hz onto a rotating composite YBCO target.[89,90] The plume of ejected materials was collected onto substrates which were heated to approximately 700° C, with typical deposition rates of 1 Å/sec. A jet of oxygen was directed toward the center of the plume while the background pressure was maintained at approximately 10 mTorr.

The samples used in this study are notable for their lack of impurity phase and high degree of epitaxial alignment perpendicular to their surface, with the YBCO c-axis perpendicular to the substrate surface. Compositional analysis with Rutherford backscattering spectrometry indicated that the films used in this study were in the 1:2:3 phase.[88,91,92] Crystalline quality was studied by measuring x-ray rocking curve widths for films nominally identical to those used in this study [87,90,91,93,94] and suggest within the limitations of the experiment that these films have nearly perfect single crystalline structure. However, transmission and scanning electron microscopy studies indicate that these films are heavily faulted. This apparent contradiction between x-ray and electron studies can be resolved by recalling that x-rays are less sensitive to small scale structure than electrons, which have shorter wavelengths and coherence lengths.[90]

The microstructure of the laser deposited films on $LaAlO_3$ and $SrTiO_3$ exhibit undulations both along the (001) planes (c-layers) and the (110) planes, with a typical structural correlation range of about 10 nm.[90] These films are nevertheless free from macroscopic grain boundaries [72,90,91] and are very homogeneous, with surface roughness less than 15 nm, and are free from any secondary phase. In contrast, laser deposited films on MgO, or films deposited onto $LaAlO_3$ or $SrTiO_3$ substrates heated above 700° C, contain grain boundaries of a few μm or larger.[90,95] Typical c-axis oriented films deposited

by off-axis sputtering exhibit a high density of intersecting (110) twins, with typical spacing ranging from 10 - 70 nm and with twin lengths from 20 - 200 nm.[92] Typical surface roughness for c-axis films deposited onto MgO is less than 5 nm.[92] Films deposited on $LaAlO_3$ can be rougher.[94] In addition, the off-axis sputtered films contain a small volume fraction of a-axis oriented grains,[92,94] typically less than 1%.

In plane film texture was examined by studying x-ray ϕ scans.[96] Both $LaAlO_3$, $SrTiO_3$ and the 1:2:3 phase of YBCO have a perovskite structure and the lattice match between these materials is good. However, a 7-9% lattice mismatch for MgO and YBCO in the (001) crystallographic direction may, under non-optimal growth conditions, lead to the formation of grains in which the in plane unit cell axis of the film is aligned with the (110) axis of the substrate, corresponding to a rotation of 45°. The size of these 45° rotated domains ranges from 0.5 to 10.0 μm.[92] Off-axis sputtered films on MgO typically contain less than 1% volume fraction of such misoriented grains and misorientations of other distinct angles.[92]

A positive correlation has been found by others between the volume fraction of high angle (45°) grain boundaries and R_s for YBCO films on MgO.[93] However, other studies of YBCO thin films on $LaAlO_3$ have found a lack of correlation between R_s and structural properties such as the quantity of 45° misoriented material. In fact film E on $LaAlO_3$, with a fairly large R_s = 180 μΩ, was found to have a very small (.06%) volume fraction of 45° misoriented material.[88]

3.3. Microwave Measurements

The microwave surface resistance R_s of samples A, B, C and E was measured at 11 - 13 GHz with a parallel plate resonator technique, described

elsewhere.[97] Two flat superconducting films of the same nominal area with a thin dielectric spacer between them form the resonator. By using a dielectric spacer with a small loss tangent and making the spacer as thin as possible it is found that the Q of the resonator is dominated by the loss in the superconducting film and is therefore inversely proportional to the surface resistance of the film. In this analysis it is assumed that the films are thick enough that rf power is not transmitted through the film. If the films are too thin then the measured value of the surface resistance will be lower than for a thick film of similar material. Values of R_s quoted for the films measured with this technique do not include any correction for radiation loss.[88,93,94,97] The effects of the finite film thickness on these measurements is discussed below.

The surface resistance of sample D was measured by placing it in a superconducting niobium cavity operated in the TE_{011} mode at 5.95 GHz as described elsewhere.[98] The value of cavity Q was converted into surface resistance by comparison with the measured Q and the calculated surface resistance of a Nb foil with nominally the same area as the sample. In this measurement rf currents are induced in both the upper and lower surfaces of the film. The substrate losses are subtracted from the result through a separate measurement of a bare substrate. The resulting value of R_s is an average for the two surfaces and may contain contributions from losses at the interface between the film and the substrate.

3.3.1. Analysis of Transmission Losses

The effect of the finite film thickness on the measurement of the microwave surface resistance has been examined by Klein *et al.*[99] at 87 GHz and 77 K by treating the film - substrate system as a transmission line and

approximating the surface impedance of a hypothetical thick slab of superconductor as $Z_\infty = R_\infty - i\,4\pi\omega\lambda/c^2$, where R_∞ and Z_∞ correspond to the surface resistance and complex impedance, respectively, of the hypothetical thick slab. This treatment is a useful guide to the effects of the finite film thickness on observed surface impedance. The concept of a bulk impedance Z_∞ is of limited validity for high T_c films, however, since the microstructure of these materials, and hence Z_∞, can depend in a complicated way on sample thickness.[92,97]

We have done similar calculations at 10 GHz and 4 K using $\lambda = 140$ nm and treating the sample as a thin superconducting film of bulk impedance Z_∞ on a 500 μm substrate of $LaAlO_3$ backed by free space. Our results are shown in Fig. 3.1, where we plot R_∞ versus R_{eff} for a variety of film thicknesses. R_{eff} is the measured, effective surface resistance which depends on the film thickness. We find that measured surface impedances at 10 GHz and 4K can depend on film thickness for films thinner than ~500 nm. For films thicker than 300 nm, however, we find that R_∞ will be at most 25% lower than the measured R_{eff} for films with measured $R_{eff} > 10$ μΩ. We have done similar calculations at 1 THz, corresponding to the lowest frequencies of the submillimeter absorptivity measurement, and find that no correction to the measured absorptivity is required for the range of measured absorptivities and film thicknesses studied.

3.4. Results

Absorptivity data for sample F are plotted in Fig. 3.2 along with 1 - $R(\omega)$, where $R(\omega)$ is the reflectivity reported earlier on the same sample.[72] Certain features, such as the small knee just below 500 cm^{-1} and the plateau between 200 and 400 cm^{-1} exist in both data sets, but there are differences in

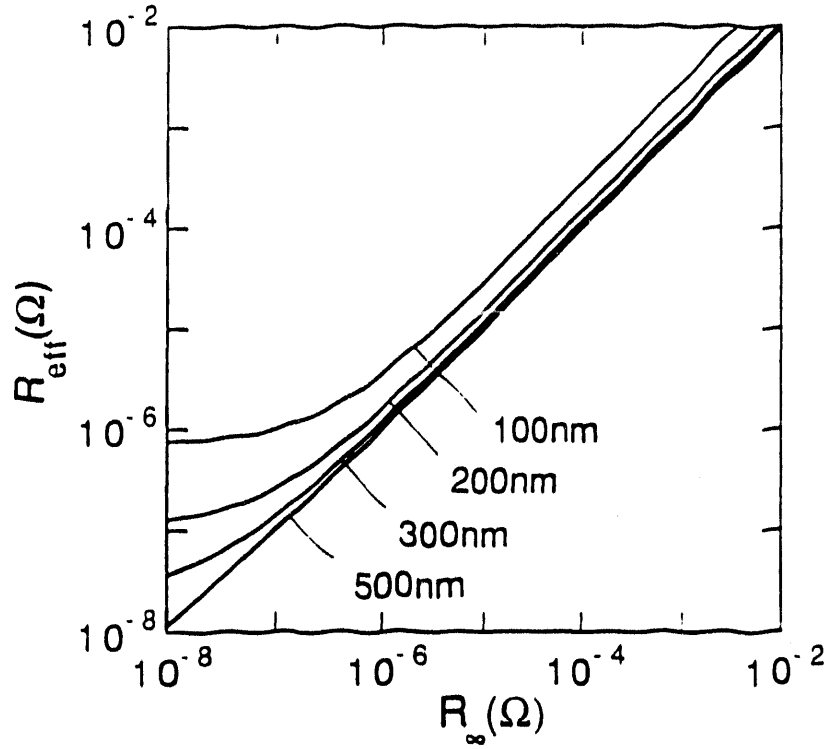

Fig. 3.1 - R_∞ versus R_{eff} at 10 GHz and 4 K using λ = 140 nm for a variety of film thicknesses. The sample is treated as a thin superconducting film of bulk impedance Z_∞ on a 500 μm substrate of $LaAlO_3$ backed by free space, as described in text. R_∞ is the surface resistance of a hypothetical thick slab, and R_{eff} is the effective surface resistance which depends on the film thickness.

the overall level and slope. The two data sets can be brought into very good agreement if we plot 0.85(1 - $R(\omega)$) + 1.1%. The additive constant may reflect the uncertainty associated with knowing the precise signal level corresponding to unity reflectivity in the reflectivity measurement. The reason for the discrepancy in slope is not known.

In order to test whether the discrepancy in Fig. 3.2 could be due to the loss of oxygen from the film in the three months between the reflectivity measurement and the absorptivity measurement, the absorptivities of this and several other films were measured before and after both plasma oxygenation and ion bombardment. Ratios of spectra measured before and

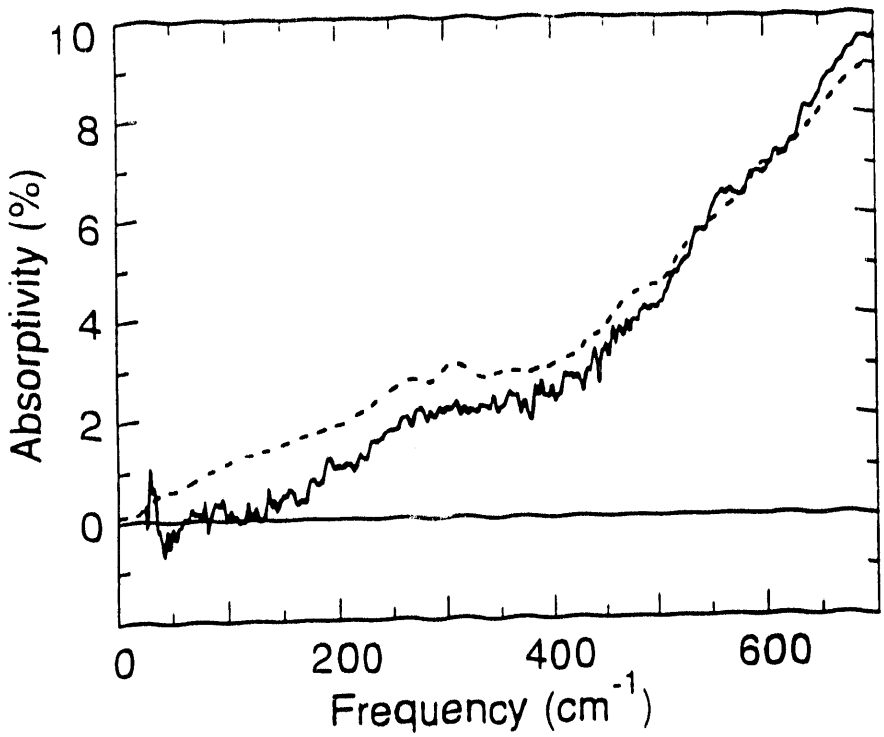

Fig. 3.2 - Absorptivity of sample F measured directly at 2K by the technique described in this work (dashed line) and deduced from a reflectivity measurement made at Bellcore at 15K (solid line).

after treatment showed observable differences which were fractionally more important in the low frequency part of our range, but neither the sign of the effect nor the frequency dependence were reproducible.

Absorptivity data for samples A through E are plotted in Fig. 3.3. The absorptivities for all samples are non-vanishing down to the lowest frequencies measured. Despite the varying deposition techniques and substrates, the infrared absorptivity spectra for samples A through D are qualitatively similar. This indicates that although we may not be observing the intrinsic absorptivity of the YBCO we are at least observing a reproducible optical signature which is insensitive to the detailed sample characteristics of high quality films. For these films the absorptivity is approximately monotonic. It increases from the lowest frequencies up to 300 cm^{-1} and has a

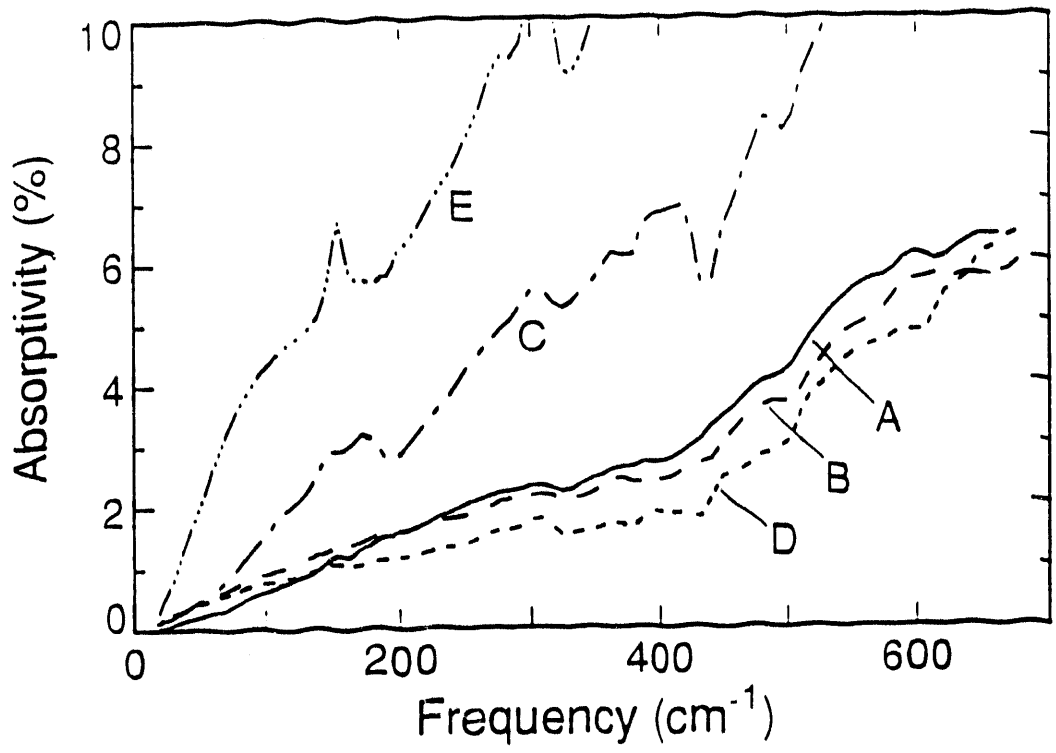

Fig. 3.3 - Measured absorptivity of samples A through E at 2 K. Sample E was intentionally prepared to give large microwave loss.

plateau from ~300 - 450 cm^{-1} above which there is an onset of additional absorptivity. There is no sign of any gap-like onset of absorption either near the BCS value of 3.5 $k_BT_c \approx 220$ cm^{-1} or near 140 cm^{-1}.[72-74,77,79] We observe distinct optical features in sample E at 150 cm^{-1} and at 310 cm^{-1} which are weakly present in sample A at 150 cm^{-1} and in all films measured at 310 cm^{-1}. These features have been identified as infrared active lattice modes.[100] Because of screening by the high conductivity in the a-b plane, observation of phonon modes is expected only for electric fields excitations along the c-axis. Both the appearance of these modes and the higher overall absorptivity show that samples C and E are of significantly lower quality than samples A, B and D. (Sample E was intentionally sputtered in an O_2 deficient atmosphere in order to have higher loss than the other films.)

Because of the low critical field H_{c1} for these superconductors it is certain that there is trapped flux in thin films at low temperatures due to the laboratory magnetic field. Flux motion driven by the incident radiation is a potential source of the loss. In order to explore this effect, fields of approximately 10 Gauss were applied normal to the films with both the smallest and largest microwave R_s. No significant differences in the measured absorptivities were observed. The effects of a magnetic field on the measured absorptivity was measured in fields up to 3 Tesla and is discussed in Chapter 6.

3.5. Data Analysis

3.5.1. Introduction

Absorptivity data for samples A through E are again plotted in Fig. 3.4 along with two theoretical fits described below. This logarithmic plot emphasizes the low frequency range of the submillimeter measurement and allows a comparison with the microwave measurements made on the same samples. The curves in this plot are displaced by factors of ten to avoid overlap. The microwave loss measurements at 4K are indicated by the filled circles for each film. The size of the circles is large enough to include estimated errors and corrections for film transparency. The solid lines give the submillimeter absorptivity measurements at 2K. Additive errors are thought to be small down to the lowest frequencies presented. Multiplicative errors could be as large as 15 percent (see Sec. II). These results give a picture of the residual loss in epitaxial a-b plane YBCO films over nearly four decades in frequency. For each film, the 10 GHz point can be connected to the submillimeter data at ~ 30 cm^{-1} by a line which varies as frequency squared. This agrees with Piel *et al.*[26] in the range from 10 to ~100 GHz (0.3-30 cm^{-1}),

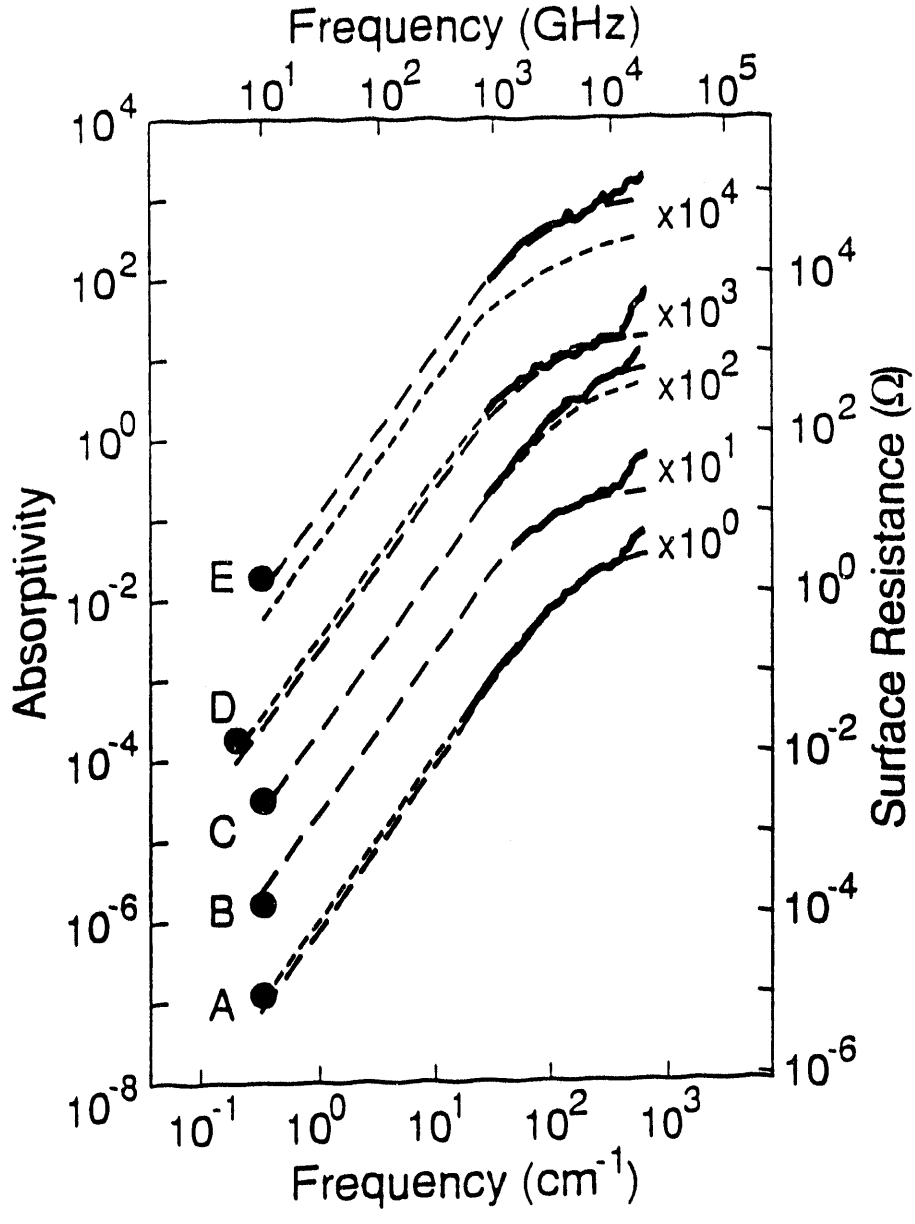

Fig. 3.4 - Measured submillimeter absorptivities of samples A through E at 2K (solid lines) multiplied by the indicated factors to separate the curves. Values of the microwave surface resistance measured for each sample at 4K are shown as filled circles. Also shown are two different fits to the absorptivity data. The interpretation of the long-dashed lines (Fit I) and the short-dashed lines (Fit II) is given in the text in terms of the weakly coupled grain and in terms of the two-fluid models.

but is in disagreement with Renk *et al.*[76] who observe the loss to be linear in frequency between 87 GHz (~ 3 cm^{-1}) and 30 cm^{-1}. The frequency dependence of the loss saturates smoothly above 30 cm^{-1} in a way that is different for different films. In contrast to the results of Pham *et al.*[16] on single crystals we do not observe the loss to vary quadratically with frequency in the range from 100 to 400 cm^{-1}.

We have analyzed data for films A through E in terms of a homogeneous two-fluid model and in terms of a model proposed by Hylton *et al.* [101,102] that treats polycrystalline high T_c films as a network of weakly coupled grains. We have also used the KK transform method to calculate the complex conductivity $\sigma(\omega)$ from the loss data for each sample.

3.5.2. Two-Fluid Model

The two-fluid model is often used to describe the electrodynamics of a homogeneous, isotropic superconductor below the gap frequency.[63] Some temperature dependent fraction n_s/n of the electrons is in the condensed phase, or superconducting state while the remainder n_n/n are in the excited, or normal state. In the implementation of the two-fluid model used here, the fraction of normal electrons n_n/n is assumed not to have the usual temperature dependence but is used as a free parameter. The conductivity can be written as

$$\sigma(\omega) = \frac{\sigma_0}{1 - i\,\omega\,\tau} + i\frac{c^2}{4\pi\lambda_{tf}^2\omega} \quad . \tag{3.1}$$

The complex normal (quasiparticle) conductivity is written in terms of $\sigma_0 = \sigma_{dc}(n_n/n)$ where $\sigma_{dc} = ne^2\tau/m$ is the normal state conductivity and τ is the

momentum relaxation time. The complex superconducting (pair) conductivity is given in terms of the superconducting penetration depth, λ_{tf}, where

$$\frac{1}{\lambda_{tf}^2} = \frac{4\pi}{c^2}\frac{n_s e^2}{m} \quad . \tag{3.2}$$

Here m and e are the mass and charge, respectively, of the paired carriers.

We can describe the two-fluid model in terms of an equivalent circuit with frequency independent lumped circuit elements, as shown in Fig. 3.5 (a). The normal carrier inductivity is $\mathcal{L}_n = m/n_n e^2 = \tau/\sigma_0$ and the superconducting carrier inductivity is $\mathcal{L}_s = m/n_s e^2 = 4\pi\lambda_{tf}^2/c^2$. The inductance per square of a film is equal to the inductivity divided by the film thickness. The free parameters for this model are λ_{tf}, σ_0 and τ.

At low frequencies for which $\mathcal{L}_n, \mathcal{L}_s << 1/\omega\sigma_0$, the penetration of the rf fields is limited by the superconducting electrons, and the absorptivity $A(\omega) = \beta_l \omega^2$ where $\beta_l = \sigma_0 \mathcal{L}_s^{3/2}/\pi^{1/2} = 8\pi\sigma_0\lambda_{tf}^3/c^3$. At intermediate frequencies for which $\mathcal{L}_s >> 1/\omega\sigma_0 >> \mathcal{L}_n$, the penetration is limited by the normal electrons and the absorptivity $A(\omega) \propto \omega^{1/2}$. Above the relaxation frequency of the normal electrons $\mathcal{L}_n, \mathcal{L}_s >> 1/\omega\sigma_0$ and the absorptivity $A(\omega) = \beta_h$ where $\beta_h = \mathcal{L}_s^{3/2}/\sigma_0\pi^{1/2}(\mathcal{L}_s + \mathcal{L}_n)^{3/2}\mathcal{L}_n^{1/2}$ is a constant up to the plasma frequency which is outside of our range. For non-vanishing $\tau = \sigma_0\mathcal{L}_n$, however, the intermediate frequency limit is accessible only for $n_n > n_s$. Our data do not show a distinct region in which the absorptivity varies as $\omega^{1/2}$.

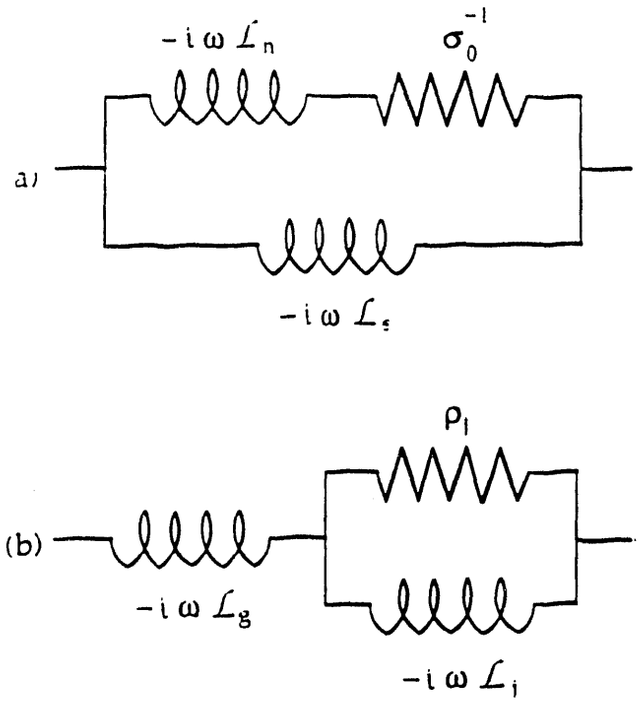

Fig. 3.5 - Equivalent circuits for (a) two-fluid and (b) weakly coupled grain models. A simple circuit transformation shows that these two circuits yield the same form for the frequency dependent fitting function for the absorptivity. The interpretation of the parameters, however, is different for the two models.

3.5.3. Weakly Coupled Grain Model

Hylton *et al.* [101] proposed a model that treats polycrystalline high T_c films as a network of weakly coupled grains, as suggested by the morphology of high T_c superconducting films. In c-axis oriented YBCO thin films the current flows in the strongly superconducting a-b planes, but is impeded by grain boundaries.[103] Hylton *et al.* proposed a phenomenological model that ignores the anisotropy of the electrical conductivity in the a-b plane and assumes that the material of the grains is an ideal BCS superconductor. The grain boundaries are modeled by resistively shunted Josephson junctions. The distributions of grain size and coupling strength between the grains are

then reduced to an effective grain size and coupling strength. It is assumed that the rf current density through the junction is small compared with the critical current I_c of the junction so that the Josephson junction can be approximated as an inductor $L_j = \hbar/2eI_c$. Introducing a characteristic length associated with the average grain size a the conductivity can be written as

$$\sigma(\omega)^{-1} = -i\,\omega\mathcal{L}_g + \left[\frac{1}{\rho_j} + \frac{1}{-i\,\omega\mathcal{L}_j}\right]^{-1} , \qquad (3.3)$$

where the superconducting inductivity of the grains is $\mathcal{L}_g = 4\pi\lambda_g^2/c^2$, the inductivity of the Josephson junction is $\mathcal{L}_j = \hbar/2ej_c a = 4\pi\lambda_j^2/c^2$. We obtain a shunt resistivity ρ_j for the junctions by assuming that the grains have characteristic length a. The parameter j_c is the critical current density of the grain boundary junction, λ_g is the penetration depth within the grains, and λ_j is the Josephson penetration depth of the junction. The equivalent circuit that represents this response is shown in Fig. 3.5 (b). The effective superconducting penetration depth λ_{eff} that would be measured in a magnetic field penetration experiment[102] is given by

$$\lambda_{eff}^2 = \lambda_g^2 + \lambda_j^2 . \qquad (3.4)$$

This parameter includes the effects of both the superconducting grains and the Josephson coupling between the grains.

The functional form for $\sigma(\omega)$ in the two-fluid model is identical to that in the weakly coupled grain model. Expressing the parameters of the two-fluid model in terms of the weakly coupled grain model parameters, we find

$$\mathcal{L}_s = \mathcal{L}_g + \mathcal{L}_j , \qquad (3.5\,a)$$

$$\mathcal{L}_n = \left(\frac{\mathcal{L}_g}{\mathcal{L}_j}\right)\left(\mathcal{L}_g + \mathcal{L}_j\right) \quad , \qquad (3.5\,b)$$

$$\sigma_0^{-1} = \rho_j \left(\frac{\mathcal{L}_g + \mathcal{L}_j}{\mathcal{L}_j}\right)^2 \quad , \qquad (3.5\,c)$$

Eq. 3.5 (a) is equivalent to Eq. 3.4 and shows that λ_{tf} in the two-fluid model is equal to λ_{eff} in the weakly coupled grain model.

3.5.4. Model Fitting

The two phenomenological models described above yield a single, three parameter frequency dependent conductivity $\sigma(\omega)$. The parameters can be interpreted either in terms of the two-fluid or in terms of the weakly coupled grain model. The three parameter conductivity $\sigma(\omega)$ is used to calculate the absorptivity $A(\omega)$, from Eq. 1.1 and 1.2, where the film is assumed to be much thicker than the penetration depth. The value of ε_∞ includes the effects of absorption above ~ 1000 cm^{-1}. We find that for $\varepsilon_\infty < 20$ the precise value of ε_∞ has no effect on the data analysis below ~700 cm^{-1}. As a consequence, the fitting function $A(\omega)$ contains just three independent parameters.

The three parameter fitting function was fit to the absorptivity spectra by a chi-squared minimization. A subset of twenty submillimeter points along with the microwave data point were used in the fitting for each sample. The data from the submillimeter spectral range were chosen to lie between ~40 - 400 cm^{-1} to avoid the onset of additional absorptivity above 450 cm^{-1} and were uniformly spaced in Log(frequency) so as not to overemphasize higher frequency data. When features such as the optical phonon at 150 cm^{-1} are

avoided the absorptivity spectra are smooth and the precise values of the chosen frequencies are unimportant. The statistical uncertainty used in fitting the data was arbitrarily set equal to 15% of the loss measured at each frequency.

The three parameter fitting function can be made to agree quite well with the data. However, since the data below the absorption edge at 450 cm^{-1} do not contain enough information to uniquely determine all three independent parameters, fits can be obtained for a range of parameter values. We use the penetration depth of 140 nm obtained from μSR experiments[104] to constrain the models in two different ways, as discussed below. We then plot contours of constant chi-squared in the remaining two parameters. In this way we are able to graphically determine the quality of the fit.[105]

3.5.4.1. Muon Spin Rotation Spectroscopy

Our use of the μSR data to constrain the weakly coupled grain model is complicated by the interpretation of the μSR data for inhomogeneous materials. μSR spectroscopy is used to sensitively measure the distribution of magnetic field strengths in a material which is immersed in a static, uniform field.[106] Typically, the material partially shields or distorts the external field, so that the spectral distribution of field strengths f(H) in the bulk is different from the external field distribution $f_{ext}(H) \propto \delta(H - H_{ext})$. In an ideal Type-II superconductor, the field in the bulk of the superconductor forms a triangular Abrikosov vortex lattice.[36] The magnetic field distribution and spectral distribution of this ideal vortex lattice can be analytically calculated and is plotted in Fig. 3.6. The field variation calculated for the case of the ideal lattice is related to the superconducting penetration depth by[107,108] $\overline{\Delta H^2} = \langle H^2 \rangle - \langle H \rangle^2 = 0.00371 \phi_0^2 \lambda^{-4}$, where ϕ_0 is the flux quantum.

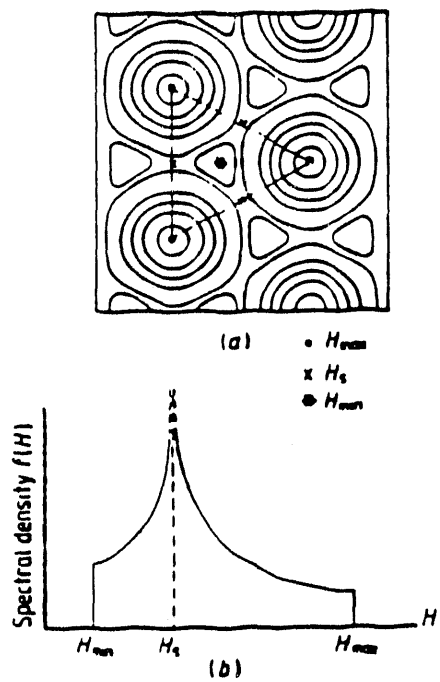

Fig. 3.6 - (a) Magnetic Field distribution and (b) spectral density of the field distribution f(H) in the mixed phase of a Type-II superconductor. This figure is taken from Ref. [106].

In most practical cases, $f_{exp}(H)$ is measured experimentally using the μSR technique and then fit to a Gaussian or a Lorentzian,[104,108,109] which roughly approximates the exact shape of f(H) shown in Fig. 3.6. The value of the superconducting penetration depth λ is then extracted from the field variation $\overline{\Delta H^2}$ calculated from the best fit to $f_{exp}(H)$.

There are several problems with this technique. First of all, the field distribution for a perfect vortex lattice is far from being a Gaussian or a Lorentzian. Second of all, defects at inhomogeneities such as grain and twin boundaries will tend to pin the magnetic vortices. Although only occurring in a relatively small volume, such inhomogeneities will tend to broaden the magnetic field distribution. In principle, the μSR experiment is capable of measuring the total volume-weighted distribution of magnetic fields

throughout the sample. In practice, however, fitting the field distribution to a Lorentzian or Gaussian is equivalent to focusing on the rather narrow distribution of fields which comprise most of the sample volume.[108] This narrow distribution of fields corresponds to the vortex lattice in the ideal superconducting grains. To the extent that the penetration depth is obtained from the field variation of the narrower field distribution, the μSR experiment measures λ_g, the penetration depth within the grains and not λ_{eff}, the effective penetration depth, which is affected by the total magnetic field distribution.

3.5.5. Discussion of Fits

The fits to the absorptivity data with λ_g = 140 nm, are called Fit I and are shown in Fig. 3.4 as long-dashed lines. Good fits are obtained to the submillimeter data and the microwave R_s for all five films measured. Results of this analysis are listed in Table 3.2. Uncertainties for each sample in Table 3.2 are estimated from constant chi-squared boundaries which define an arbitrary confidence region about the best fit. Errors indicate relative uncertainties between the parameters and do not include any uncertainty in λ_g. Any analysis of submillimeter data using the weakly coupled grain model suffers from the problem that most of the discussions in the literature use two-fluid concepts which are only appropriate for a homogeneous material. In order to make contact with this literature we convert the weakly coupled grain model parameters obtained by setting λ_g = 140 nm to the two-fluid model parameters σ_0, $\hbar/\tau$ and $\lambda_{tf} = \lambda_{eff}$ which give the same excellent Fit I to the absorptivity. The values of both the two-fluid and the weakly coupled grain parameters obtained in this way are listed in Table 3.2.

Sample	λ_j (nm)	ρ_j ($\mu\Omega$ cm)	I_cR (mV)	a [b] (nm)	$\lambda_{eff}=\lambda_{tf}$ (nm)
A	148 ± 17	93 ± 25	11.0 ± 2.5	40 ± 10	204 ± 12
B	175 ± 30	57 ± 18	4.9 ± 1.2	29 ± 12	224 ± 23
C	265 ± 55	216 ± 90	8.0 ± 2.1	12 ± 5	299 ± 49
D	160 ± 20	41 ± 9	4.2 ± 0.9	34 ± 10	212 ± 15
E	502 ± 100	300 ± 150	3.1 ± 0.6	4 ± 1	521 ± 96

Sample	σ_0 $\times 10^3$ (Ω cm)$^{-1}$	$(2\pi c\tau)^{-1}$ (cm^{-1})	l [a] (nm)	n_n/n (%)	ω_{p0} (eV)
A	3.0 ± 0.5	377 ± 80	3.1 ± 0.6	53 ± 33	1.4 ± 0.2
B	6.5 ± 1.5	201 ± 50	5.8 ± 1.4	61 ± 52	1.4 ± 0.3
C	2.8 ± 0.9	596 ± 196	2.0 ± 0.6	78 ± 96	1.4 ± 0.4
D	7.8 ± 1.6	157 ± 31	7.4 ± 1.5	57 ± 39	1.4 ± 0.2
E	2.8 ± 1.0	702 ± 256	1.7 ± 0.6	93 ± 131	1.4 ± 0.5

[a] Values of the electronic mean free path, l, are calculated assuming $v_F = 2.2 \times 10^7$ cm s^{-1}

[b] Values of the effective grain length, a, are calculated assuming $j_c = 3 \times 10^7$ A cm^{-2}

Table 3.2 - Model parameters deduced from Fit I to the measured absorptivity. This fit is successful for all films measured. The weakly coupled grain model parameters correspond to the assumption that $\lambda_g = 140$ nm, which is physically reasonable for all films. Values of λ_{tf} deduced from this fit range from 200 nm in our films with lowest absorptivity to 520 nm in our highest loss film.

The two-fluid parameters in Table 3.2 correspond to values of λ_{tf} which vary from 200 nm in the films with the lowest absorptivity to 520 nm in the film with the highest absorptivity. These values are in fact consistent

with the results for the magnetic field penetration depth from microstrip resonator experiments[110] on films. Since the penetration depth in films may actually be larger than for single crystals, it can be argued that the two-fluid parameters for Fit I in Table 3.2 have physical meaning.

An alternative way to constrain the two-fluid model is to use the μSR result and set λ_{tf} = 140 nm. The results of this procedure, called Fit II, are shown in Fig. 3.4 as the short-dashed lines. A good fit to the measured absorptivity is found for the low absorptivity samples A, B and D which smoothly joins the submillimeter data to the microwave R_s. However, Fit II is not successful for the higher loss samples C and E, which are expected to have larger penetration depths. In the case of film E, which has high residual loss, the fit does not even intersect the data. The fit can be forced to intersect the data, but the resulting slope at high frequencies is then so small that the value of chi-squared is increased. Results of this analysis are shown in Table 3.3 for the low loss samples. The discrepancy between the two sets of parameters for films A, B and D can be interpreted as a measure of our ignorance of the proper physical constraint for the two-fluid model fit.

We can understand the poor quality of Fit II for the high absorptivity films C and E in the following way. If the two-fluid model with λ_{tf} = 140 nm adequately describes the losses in low absorptivity films, then as film quality decreases, perhaps as a result of increased granularity, the absorptivity of the films increase, and we expect that the superconducting penetration depth λ_{tf} will also increase. By fixing λ_{tf} we insure that our simple model given by Fit II will not be able to describe the optical properties of the high absorptivity films.

Sample	σ_0	$\hbar/\tau$	l [a]	n_n/n	ω_{p0}
	$\times 10^3$ (Ω cm)$^{-1}$	(cm^{-1})	(nm)	(%)	(eV)
A	12 ± 3	566 ± 210	2.0 ± 0.8	75 ± 77	2.9 ± 0.6
B	28 ± 8	426 ± 215	2.7 ± 1.4	85 ± 123	3.6 ± 1.2
D	36 ± 16	305 ± 195	3.8 ± 2.4	84 ± 165	3.5 ± 1.6

[a] Values of the electronic mean free path, l, calculated assuming $v_F = 2.2 \times 10^7$ cm s^{-1}

Table 3.3 - Two-fluid model parameters deduced from Fit II which is successful only for the highest quality films A, B and D. From the two-fluid viewpoint this fit corresponds to setting λ_{tf} equal to the μSR result of 140 nm. This fit can also be obtained from a weakly coupled grain model viewpoint, but only with the non-physical constraint that λ_{eff}= 140 nm.

3.5.5.1. Scattering Rate

Reflectivity measurements made on YBCO thin films at temperatures just above T_c ~90K obtain values of $\hbar/\tau$ ~100 cm^{-1}. Assuming a BCS gap of 3.5 $k_B T_c$ this result implies that YBCO is in the clean limit of the classical skin effect regime of superconductivity ($1/\tau << 2\Delta$; $\xi_0 << l << \lambda_L$).[72] It is reasonable to assume that the quasiparticle scattering rate should rapidly decrease for temperatures below T_c. Such behavior has been observed by several groups.[82,111,112] However, at low temperature we find scattering rates of 150 cm$^{-1} > 1/\tau >$ 700 cm^{-1} for all films measured, corresponding to values of the electronic mean free path l between 2 and 7 nm, assuming $v_F = 2.2 \times 10^7$ cm s^{-1}.[10] It is interesting to speculate on possible explanations for a faster scattering at low temperatures, which is a property of both the parameters of Table 3.2 and of Table 3.3.

A scattering rate $1/\tau$ which is larger in the superconducting state than above T_c can be understood if we postulate that the film contains two types of carriers, which we call "good electrons" and "bad electrons". The "good electrons" condense rapidly into the superconducting ground state below T_c as in a BCS superconductor. The "bad electrons" remain in the normal state at all temperatures. If the "good electrons" have a slow scattering rate and a large oscillator strength and the "bad electrons" have a fast scattering rate and a relatively small oscillator strength then the effective conductivity of the composite system above T_c will be dominated by the "good electrons." Below T_c where the "good electrons" have all condensed the scattering will be dominated by the "bad electrons" and a faster scattering rate will be measured.

3.5.5.2. Superconducting Penetration Depth

We can determine the superconducting penetration depth from infrared measurements by determining the 'missing area' between $\sigma_1(\omega) = \mathrm{Re}[\sigma(\omega)]$ in the normal and superconducting states. This 'missing area' is oscillator strength which condenses into a delta function at zero frequency upon entering the superconducting state, and is related to the number of condensed carriers and thus to the superconducting penetration depth.[36] 'Missing area' calculations based on reflectivity measurements using single crystals obtain values for the penetration depth which are consistent with the μSR result of 140 nm,[73,74] not with λ_{eff}, which is larger than 140 nm, as might be expected from the weakly coupled grain model. Differences between the losses in thin films and crystals may account for some of this discrepancy despite the fact that above 400 cm^{-1} the loss in films A, B and D are nearly identical to the losses in YBCO single crystals with $T_c \sim 90$ K.[73,74] Another possible explanation is a difference between the absorptivity assumed in

interpreting the two experiments. In the missing area calculations the superconducting state conductivity $\sigma_1(\omega)$ below 140 cm^{-1} was taken to be either zero[73] or constant[74] and equal to ~1400 $(\Omega - cm)^{-1}$. As discussed in Sec. 3.6, we find a larger oscillator strength below 140 cm^{-1} both from Fit I and from the KK analysis of our loss data. Inclusion of this additional low frequency oscillator strength into the 'missing area' calculation for the superconducting penetration depth λ would lead to larger values of λ. However, λ only increases inversely as the square root of the area difference so that λ is still smaller than λ_{eff}. A third possible explanation is that grain models can be expected to fail at high enough frequencies that the coherence length of the radiation becomes small compared with typical grain sizes.

3.5.5.3. Carrier Densities

The normal and superconducting carrier densities, n_n and n_s, are determined from σ_0 / τ and $c^2 / (4 \pi \lambda_{eff}^2)$, respectively, using parameters obtained from our modeling. Values for n_n/n determined from Table 3.2 (Fit I) range from 50 to 60% at 2K for the low absorptivity films A, B and D, and from 80 to 90 % for the higher absorptivity films C and E, more than five orders of magnitude larger than the prediction of the Gorter-Casimir two-fluid model, where $n_n/n = (T/T_c)^4$. These values of the normal carrier density indicate that a significant proportion of the carriers are in the normal state even at 2 K. The values for the low loss films are consistent with the results of Gao *et al.*[82] who use a two-fluid model to fit their combined transmissivity and reflectivity data, obtaining values of n_n/n at low temperature between 10 and 50 %. Values for n_n/n determined from Table 3.3 (Fit II) range from 75 to 85%, where the results are listed only for the low absorptivity films A, B and D which are consistent with the losses described by Fit II.

We can also determine the plasma frequency $\omega_{p0}^2 = 4\pi (n_n + n_s) (e^2/m)$ which corresponds to the carrier concentration $(n_n + n_s)$. Because our simple models are used to fit the data below the sharp onset at 450 cm^{-1}, ω_{p0} does not contain information about oscillator strength at frequencies above 450 cm^{-1}. Values for ω_{p0} listed in Table 3.2 for Fit I are all equal to 1.4 eV. Several groups have modeled their low frequency spectra with a Drude oscillator in an attempt to deduce a temperature independent plasma frequency corresponding to the free carriers. Our values for ω_{p0} listed in Table 3.2 are in good agreement with these optically determined estimates for the Drude plasma frequency, which vary from 1.0 to 1.5 eV.[72,73,82] In contrast, values for ω_{p0} from Fit II are larger than or equal to the value of the optically determined plasma frequency ω_p = 3 eV corresponding to the total oscillator strength.[10] Since ω_{p0} is determined only from the oscillator strength below ~450 cm^{-1}, it must be significantly less than ω_p. This discrepancy, in addition to the results from the Kramers-Kronig analysis presented in Sec. 3.6, gives strong evidence that Fit II is fundamentally unsatisfactory, despite the fact that it can describe the losses in the lowest absorptivity films A, B and D.

3.5.5.4. Weakly Coupled Grain Model Parameters

For the weakly coupled grain model we have determined the $I_cR = \rho_j j_c a$ product and the characteristic grain length a of the junction. In order to determine a we must assume a value for the critical current density j_c, since only the product $j_c a$ is determined from the weakly coupled grain model. We assume that the critical current density j_c of the grain boundaries is essentially the critical current density 3×10^7 A cm^{-2} of the films, which is a typical value for high quality c-axis films at 4K,[92] in agreement with measurements made on films A and B.[92,93] I_cR products in Table 3.2 are consistent with

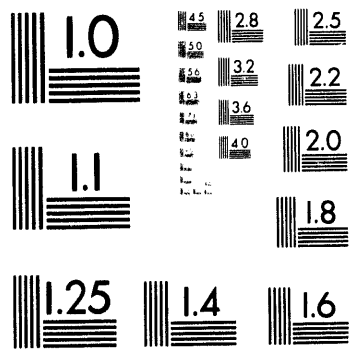
1.0
1.1
1.25
1.4
1.6
1.8
2.0
2.2
2.5
2.8
3.2
3.6
4.0
4.5
5.0
5.6
6.3

2 of 2

measurements on isolated grain boundary junctions, which range between 0.2 and 8 mV at 4.2K.[103] Characteristic grain lengths *a* range from 4 to 40 nm for all films. These values are roughly consistent with the spatial correlation range in the laser ablated films of ~ 10 nm,[90] and with twin domain sizes in off-axis sputtered films of ~ 20-200 nm.[92]

Although the weakly coupled grain model is able to fit our loss data so well, values of *a* found from the best fits are considerably smaller than the size of typical 45° misoriented grains, which range from 0.5 to 10.0 μm.[92] Such high angle grain boundaries are known to behave as resistively shunted junctions[103] which could therefore justify the use of the weakly coupled grain model. However, the volume fraction of such grains in our films is typically less than one percent,[92,93] which is an indication that the high angle grain boundary junctions probably do not provide the dominant intergrain coupling mechanism in these films. The parameter values deduced from fitting the weakly coupled grain model, however, are quite reasonable considering the simplicity of the model.

3.5.5.5. Including Oscillator Strength Below 450 cm^{-1}

The technique we have used to fit our data explicitly assumes that the absorption mechanism above 450 cm^{-1} does not contribute any oscillator strength below that frequency. This assumption is justified by the sharpness of the onset as is seen in Fig. 3.4. In order to test the sensitivity of the weakly coupled grain and two-fluid model parameters to this assumption, we have analyzed our data including oscillator strength peaked at ~1000 cm^{-1} proposed by other investigators.[11,72] While the addition of this high frequency oscillator strength reduces the oscillator strength at lower frequencies required to fit the data, the effect is quantitatively small and the model

parameters obtained in this way are all within the experimental uncertainties reported in Tables 3.2 and 3.3.

3.6. Kramers-Kronig Analysis

As an alternative to the model fitting described above, we have also used the KK transform technique to deduce the frequency dependent conductivity, $\sigma(\omega)$, from our loss data. In contrast to the fitting procedure, the KK technique requires a knowledge of the loss, or equivalently the reflectivity, for all frequencies. In all practical cases the loss is measured over some finite frequency interval and extended to zero and infinite frequencies, respectively, by suitable extrapolations. Care must be taken in extending the loss data as considerable uncertainties in the inferred conductivity may result, even at frequencies far from the range of the extrapolations.

3.6.1. Introduction

Although unnecessary confusion has arisen because some authors do not adequately describe their extrapolations, the effect of uncertainties in the low temperature reflectivity on the conductivity determined from the KK transform is widely suspected. For example, it has been briefly discussed by Orenstein *et al.*.[73] Progress in determining accurate values of $\sigma(\omega)$ really depend on the availability of better low frequency data. The absorptivities which we have directly measured along with microwave surface resistance measurements can improve this situation.

The Kramers-Kronig analysis of our data is in good agreement with results from fitting our data to the simple weakly coupled grain model for the a-b plane conductivity. However, below 450 cm^{-1} it is in disagreement with some published results of other workers obtained from Kramers-Kronig

analysis of reflectivity data. To understand this discrepancy we analyze how the conductivity determined by the Kramers-Kronig transform technique depends on some commonly used low frequency extrapolations of reflectivity data.

3.6.2. Extrapolations Used in the KK Analysis

There are two common low frequency extrapolations used for materials such as YBCO. One technique[74] is to use the Hagen-Rubens relation for the absorptivity $A = (1 - R) = \alpha \omega^{1/2}$, which assumes the behavior of a normal metal at frequencies for which $\omega\tau << 1$. The value of α is chosen so that the extrapolation smoothly joins the reflectivity data at some frequency ω_0 below which the measured reflectivity is judged not to be reliable. While there is a clear justification for using this extrapolation to describe the reflectivity of a metal in the normal state, using it to describe the low frequency, low temperature loss of a superconductor such as YBCO is less justified. A second technique[73] for suppressing noise in the reflectivity is to simply set $A = 0$ ($R = 1$) below ω_0. This results in $\sigma_1 = 0$ below the same ω_0. While a value of $\sigma_1 = 0$ is consistent with our expectations for the behavior of low T_c superconductors at low temperatures and for frequencies well below the gap, there is little experimental evidence from the cuprate superconductors to support this dependence.

In contrast to the low frequency extrapolation, the choice of a high frequency extrapolation can contribute an additive constant to $\sigma(\omega)$ for frequencies far below the extrapolation. We extend our absorptivity data to higher frequencies in two different ways. We have smoothly grafted our data, which ends at 700 cm^{-1}, onto reflectivity data for a good quality epitaxial film[113] which extends to 5 eV (40,000 cm^{-1}). This reflectivity is roughly

constant near 5 eV, with R ~ 0.08 . We then extrapolate the data to infinite frequency by assuming that the reflectivity remains constant above 5 eV. This is similar to the technique used by Orenstein *et al.*.[73] We have also grafted our loss data onto the data of Tajima *et al.*,[114] which extends to 35 eV. Above this frequency we have extrapolated the reflectivity measured by Tajima *et al.* by an ω^{-4} dependence, which is the free electron asymptotic limit. This is similar to the technique used by Schlesinger *et al.*.[74] Despite the difference between these extrapolations, the conductivities determined by the KK transform for both of these high frequency extrapolations are nearly identical below 2000 cm^{-1}.

3.6.3. Results

The results of this analysis are summarized in Fig. 3.7 where we plot $\sigma_1(\omega) = Re[\sigma(\omega)]$ for sample B. The solid line is obtained from the KK transform using the $A = \beta \omega^2$ low frequency extrapolation; the long-dashed line is from Fit I; and the short-dashed line is from Fit II. This figure is representative of the results obtained for all samples. We find remarkable agreement between the conductivity determined from the KK transform and that from Fit I. This agreement supports the parameter set obtained from the weakly coupled grain model by setting $\lambda_g = 140$ nm as a phenomenological description of the submillimeter and millimeter wave losses in YBCO. In particular, this agreement gives us confidence in our interpretation of λ_g, not λ_{eff}, as the superconducting penetration depth which is analogous to the penetration depth measured by μSR techniques, as discussed in Sec. 3.5.4.1. The two-fluid model is also successful if the values of λ_{tf} in Table 3.2 are used to constrain the fit. If, however, we choose $\lambda_{tf} = 140$ nm in the two-fluid model, the conductivities resulting from the best fit of the model to the

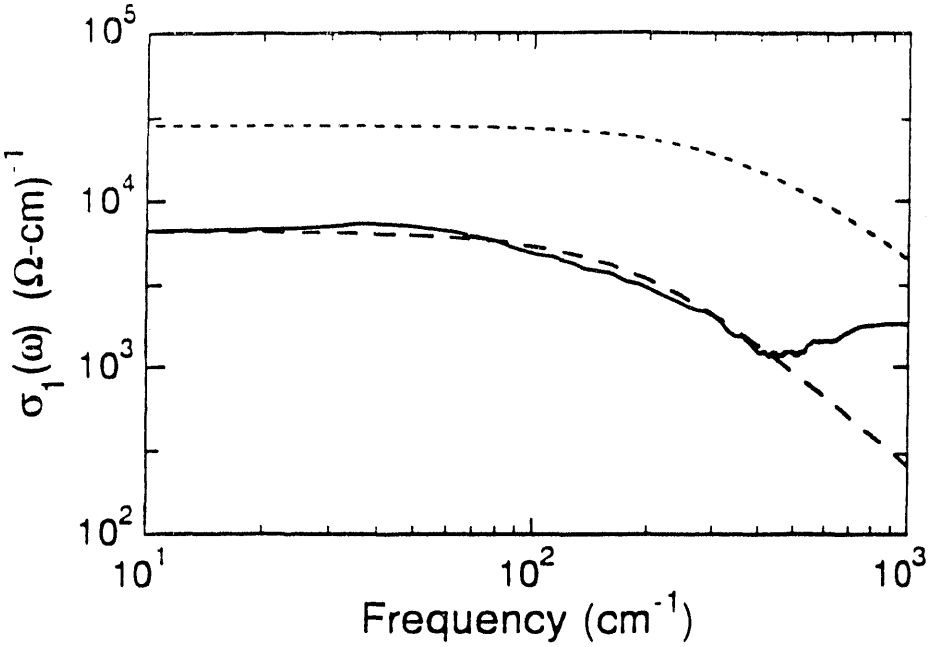

Fig. 3.7 - Values of $\sigma_1(\omega)$ for sample B determined from a Kramers-Kronig analysis using the $A = \beta\ \omega^2$ low frequency extrapolation (solid line); from the best fit of either the two-fluid model with $\lambda_{tf} = 140$ nm or the weakly coupled grain model with $\lambda_{eff} = 140$ nm (short-dashed line); and from the best fit of the weakly coupled grain model with $\lambda_g = 140$ nm (long-dashed line).

absorptivity data are consistently larger than the results of the KK analysis for frequencies below 700 cm^{-1}, as indicated in Fig. 3.7.

The results of our KK analysis of our absorptivity data for samples A, C, D and E are shown in Fig. 3.8. The solid line is obtained from the KK transform using the $A = \beta\ \omega^2$ low frequency extrapolation; the long-dashed line is from Fit I. Again, we find remarkable agreement between the conductivity determined from the KK transform and that from Fit I. The results are qualitatively similar for the low absorptivity samples A, B and D. Values for the superconducting penetration depth λ_{tf} determined from the KK transform, which are obtained from the low frequency slope of $\sigma_2(\omega)$, are consistent with the results of our model fitting for the low loss films.

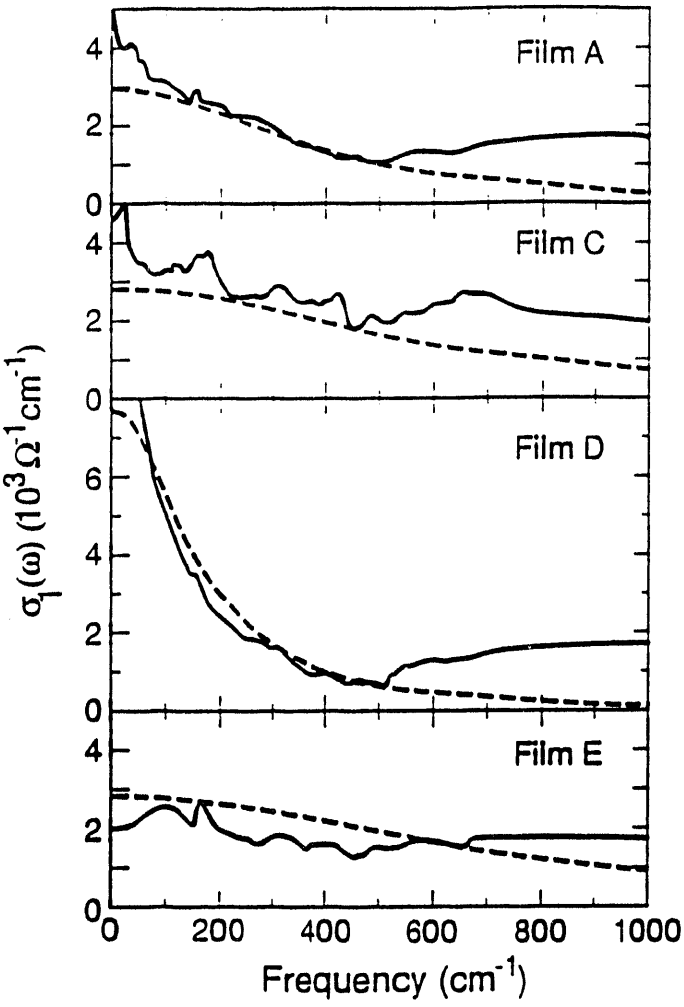

Fig. 3.8 - Conductivity $\sigma_1(\omega)$ determined from a KK transform of our direct absorptivity data extrapolated to low frequencies as $A = \beta\,\omega^2$ (solid lines) compared with the best fit to our absorptivity data using the weakly coupled grain model (dashed lines) for samples A, C, D and E. Samples A and D are high quality c-axis films. Samples C and E are of lower quality as discussed in the text.

The absorptivities measured below 700 cm^{-1} are larger for samples C and E than for samples A, B and D. Samples C and E are thought to be of significantly lower quality. Sample E was intentionally sputtered in an oxygen

deficient atmosphere to produce large residual microwave loss. The solid curves of $\sigma_1(\omega)$ deduced by the KK method for samples C and E plotted in Fig. 3.8 are significantly different from the results shown for the high quality samples. The appearance of phonon structure, for example, demonstrates either the existence of crystallites whose c-axis is not perpendicular to the sample plane or of considerable surface roughness.

Despite the fact that the weakly coupled grain model is able to fit the loss data for all five films below ~450 cm^{-1}, the agreement between the best fits and the KK transforms is not good for the high absorptivity samples C and E. For sample C, the weakly coupled grain conductivity does fit well to the minima between the phonon modes. This result may be expected as the grain model is fitted to the measured absorptivity only at points between the modes. Thus the effects of the phonons are not included in the grain model. The two curves of $\sigma_1(\omega)$ for sample E appear to be displaced by an additive constant. There is a special problem with the KK analysis of the absorptivity data for the lossy sample E which is thought to be deficient in oxygen. The measured absorptivity for sample E does not intersect the high frequency extrapolations described above which are appropriate for high quality samples. Various plausible linear interpolations have been used which cause 20% variations in the values of $\sigma_1(\omega)$ above 700 cm^{-1}. If the high frequency absorptivity of sample E is very different from that assumed, the results for $\sigma_1(\omega)$ could be shifted by an additive constant throughout the frequency range shown.

The results of our KK transforms of data for high quality samples are in agreement with the results of other workers both in magnitude and overall shape for frequencies above ~400 cm^{-1}.[72-77] In particular, we observe the well known conductivity onset at 450 cm^{-1}. Below 400 cm^{-1} we observe that the

conductivity decreases slowly from a peak at $\omega = 0$. The values of $\sigma_1(0)$ which we have found from our fits to the grain model range from 3000 to 8000 $(\Omega\ cm)^{-1}$ for the YBCO samples A through E. This result is consistent with two recent reflectivity experiments,[75,76] one of which was extended with a measurement of the microwave loss at 87 GHz.[76] It is interesting to note that our results are also consistent above ~ 100 cm^{-1} with the a-axis conductivity determined from the directly measured absorptivity of a detwinned single crystal of $YBa_2Cu_3O_7$.[81] However, below 400 cm^{-1} our results are in disagreement with the low temperature, low frequency conductivity determined from KK transforms of other reflectivity data,[72,73,77] from a combined transmissivity and reflectivity measurement,[82] and from a direct absorptivity measurement on twinned single crystals.[16] Uncertainties introduced into the KK transform by arbitrary low frequency extrapolations may be responsible for these discrepancies.

3.6.4. Effects of Low Frequency Extrapolation on Results of KK Analysis

We now use the infrared and microwave results for the high quality epitaxial c-axis film B to illustrate the effects of various low frequency extrapolations. The solid curve in Fig. 3.9 gives $\sigma_1(\omega)$ for sample B from the KK method with the ω^2 low frequency extrapolation between the submillimeter and microwave data. This curve rises slightly from its value at zero frequency to peak at ~50 cm^{-1}, and then drops to a minimum at 450 cm^{-1} above which there is a well known onset of absorptivity which has been observed by many workers.[10] This is our best estimate of the correct $\sigma_1(\omega)$ for sample B. The dotted lines in Fig. 3.9 (a) correspond to the KK transform of the same absorptivity data which gives the solid line, but are obtained by setting A = 0 below the cutoff frequencies ω_0 = 30, 70 and 140 cm^{-1}. One effect

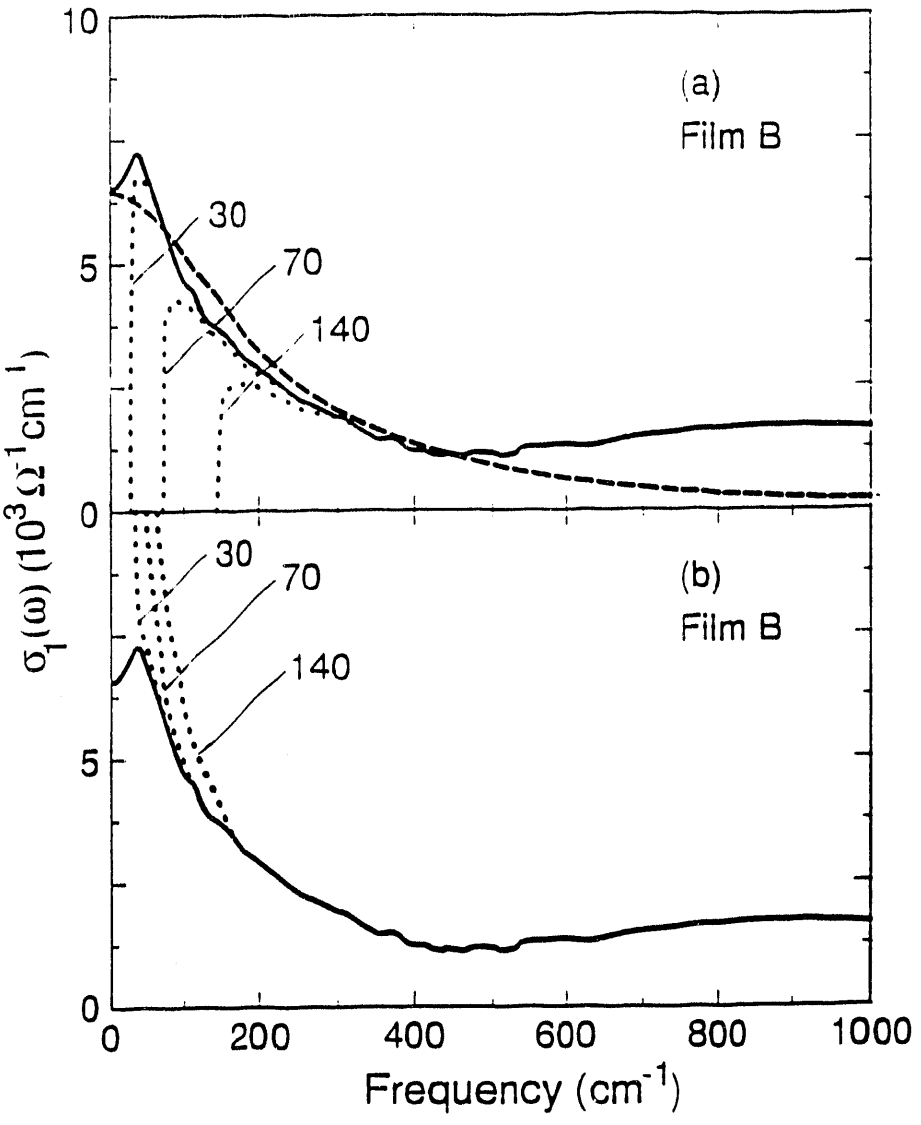

Fig. 3.9 - Conductivity $\sigma_1(\omega)$ determined from a KK transform of our direct absorptivity data extrapolated to low frequencies as $A = \beta\,\omega^2$ (solid line) for the low absorptivity epitaxial c-axis film B. This result is compared with curves for $\sigma_1(\omega)$ obtained from the KK method by extending the absorptivity data with (a) an $A = 0$ extrapolation and (b) an $A = \alpha\,\omega^{1/2}$ extrapolation below 20, 70 and 140 cm^{-1} (dotted lines). Also shown in (a) is $\sigma_1(\omega)$ obtained from a best fit to our absorptivity data using the weakly coupled grain model (dashed line).

of this artificial low frequency extrapolation is to introduce a prominent absorptivity edge precisely at ω_0, below which $\sigma_1 = 0$. This artificial

suppression of σ_1 at low temperature can introduce errors into so called 'missing area' calculations,[36] where the superconducting penetration depth is determined from the difference in oscillator strength between the low and high temperature values of $\sigma_1(\omega)$. The error will tend to decrease such estimates of the penetration depth, but only inversely as the square root of the area difference. The A = 0 extrapolation also leads to values for $\sigma_2(\omega)$ which in the vicinity of ω_0 deviate strongly from the result obtained from our ω^2 extrapolation. The long-dashed line in Fig. 3.9 is from Fit I with λ_g = 140 nm.

We have also analyzed the effects of the $A = \alpha\ \omega^{1/2}$ low frequency extrapolation on the KK transform. The dotted lines in Fig. 3.9 (b) correspond to σ_1 obtained from the KK transforms of the absorptivity data analyzed with the absorptivity extrapolated as $\alpha\ \omega^{1/2}$ below the cutoff frequencies ω_0 = 30, 70 and 140 cm^{-1}. As in Fig. 3.9 (a), the solid line in Fig. 3.9 (b) comes from our ω^2 low frequency extrapolation. All of the curves for σ_1 obtained with the $A = \alpha\ \omega^{1/2}$ extrapolations closely approximate the solid curve above the respective values of ω_0. Below the cutoff frequencies, however, they diverge from the solid curve and provide an upper bound to the solid curve. Results for σ_2 obtained with the $A = \alpha\ \omega^{1/2}$ extrapolations are all within ~20% of the result obtained from the ω^2 extrapolation for frequencies above ~50 cm^{-1}. Below ~50 cm^{-1} the curves diverge.

The discussion presented above suggests that the small peak in $\sigma_1(\omega)$ at ~50 cm^{-1} observed for film B could arise from an error in the ω^2 interpolation between submillimeter and microwave data. A larger peak is seen in sample D where σ_{max} ~ 15,000 $(\Omega\ cm)^{-1}$ and σ_{dc} ~ 12,000 $(\Omega\ cm)^{-1}$. In fact, by varying the parameter $\beta = A/\omega^2$ by ± 20% we are able to either remove or introduce sharp peaks and valleys in $\sigma_1(\omega)$ near ~50 cm^{-1}. Even though the ω^2 interpolation between submillimeter and microwave data represents a

significant improvement in our understanding of the frequency dependent losses, it is not sufficiently accurate to eliminate all errors from the KK analysis. Consequently, the KK analysis presented here must be considered unreliable below ~50 cm^{-1}.

3.7. Conclusions

We have measured the residual loss in six a-b plane epitaxial thin films of $YBa_2Cu_3O_7$ from 30 cm^{-1} (1.5 THz) to 700 cm^{-1} (21 THz) and for five of the six films near 0.3 cm^{-1} (10 GHz). We do not observe any gap-like features below 450 cm^{-1} nor is there any indication of an onset of absorptivity at ~ 140 cm^{-1}. For each of the five films the loss measured near 0.3 cm^{-1} can be connected to the submillimeter data at ~30 cm^{-1} by a line which varies as the frequency squared. Above ~30 cm^{-1} the loss saturates smoothly in a way which is different for different films. Above 450 cm^{-1} there is a sudden onset of additional absorptivity and the loss data diverge rapidly from model fits, suggesting the onset of an additional absorption mechanism.

We have used both a homogeneous two-fluid and an inhomogeneous weakly coupled grain model for the electrical conductivity to fit the frequency dependent absorptivity below the onset at 450 cm^{-1}. Both of these models yield the same three parameter fitting function. Because our models are strictly valid at frequencies below the superconducting gap, our model fitting implicitly assumes that the superconducting energy gap 2Δ, if one exists, occurs at or above 450 cm^{-1}. We find that the inhomogeneous weakly coupled grain model is able to smoothly fit the data for all films (Fit I) from 0.3 cm^{-1} (10 GHz) to 450 cm^{-1} (13.5 THz) when the parameter λ_g corresponding to the superconducting penetration depth within the BCS like grains is constrained by the μSR result. Our use of the μSR data to constrain λ_g in the weakly

coupled grain model is consistent with the interpretation of the μSR measurement for inhomogeneous materials.[108]

Fit I is also equivalent to a two-fluid model in which λ_{tf} varies from ~1.5 times the μSR result for our lowest absorptivity films to ~3.7 times the μSR result for our highest absorptivity film. The fraction of normal carriers n_n/n determined from this fit range from 50 to 60% at 2K for the low absorptivity films A, B and D, and from 80 to 90 % for the higher absorptivity films C and E, indicating that a significant proportion of the carriers are in the normal state even at 2 K. The total carrier density ($n_n + n_s$) determined from this two-fluid interpretation of Fit I is in agreement with optically determined estimates for the free carrier oscillator strength and the conductivity determined from Fit I is in excellent agreement with a KK analysis of the absorptivity data. However, when λ_{tf} is constrained by the μSR result to 140 nm, the resulting Fit II is only satisfactory for our lowest absorptivity films. In addition, the results are not consistent with the optically determined plasma frequency. Both fits correspond to a relaxation rate $1/\tau$ for the normal carriers that produce the residual loss that is significantly larger than the rate deduced for $T > T_c$. The fact that the successful Fit I comes naturally from a weakly coupled grain model with no adjustable parameters suggests that weak link behavior may play a significant role in the microwave and submillimeter losses. Values of junction I_cR products and a characteristic length determined from the model best fits are consistent with these independently measured quantities.

We have also determined $\sigma(\omega)$ from a KK transform of the absorptivity data and have used two different high frequency extrapolations and an $A = \beta\,\omega^2$ extrapolation below 30 cm^{-1} to extend the loss data to zero frequency. The low frequency extrapolation is consistent with measurements

on the same films near 10 GHz. The conductivities $\sigma(\omega)$ obtained from this analysis are in good agreement with results obtained from fitting our absorptivity data to the weakly coupled grain model when the superconducting penetration depth in the grains is constrained by the μSR result. We have compared our results to those obtained using less physical extrapolations found in the literature. The $A = \alpha\,\omega^{1/2}$ extrapolation provides an upper limit to the low frequency $\sigma_1(\omega)$ obtained from a truncated data set. In contrast, the $A = 0$ extrapolation is more dangerous because it introduces an artificial gap-like feature in $\sigma_1(\omega)$ at the cutoff frequency ω_0 which is not present in the more realistic data set.

4. Direct Submillimeter Absorptivity Measurements on Epitaxial Tl-Ca-Ba-Cu-O Films at 2K

We have used both bolometric and cavity techniques to obtain accurate submillimeter and microwave loss data for epitaxial thin films of $Tl_2Ca_2Ba_2Cu_3O_{10}$ and $Tl_2CaBa_2Cu_2O_8$ at low temperatures. The absorptivity of these films at 100 cm^{-1} is a factor of five lower than that obtained by others from a reflectivity measurement on a ceramic sample. We observe strong phonon structure for frequencies between 70 and 600 cm^{-1}, which are in agreement with a lattice dynamical calculation. Our results show remarkably similar phonon structure to that observed in a ceramic sample. This is in strong contrast to the case for other high T_c superconductors such as $YBa_2Cu_3O_7$, where phonon structure observed in ceramic samples is absent in epitaxial oriented films and crystals because of the electronic screening due to the high conductivity of the a-b planes. At microwave frequencies the

absorptivity follows a frequency squared dependence, and is consistent with the submillimeter results.

4.1. Introduction

The relatively high transition temperature of the cuprate superconductors $Tl_2Ca_2Ba_2Cu_3O_{10}$ and $Tl_2CaBa_2Cu_2O_8$, (TCBCO) with T_c ~ 125 K and 100 K, respectively, make these materials good candidates for passive low loss devices. Such devices could take advantage of the potentially low microwave losses at the relatively low reduced temperature $t = T/T_c$ attainable at liquid Nitrogen temperatures. However, preparation of thin films of the highest T_c compound, $Tl_2Ca_2Ba_2Cu_3O_{10}$, is complicated by the rapid loss of Tl during high temperature annealing, [115] and by the structural similarity of the $Tl_2CaBa_2Cu_2O_8$ phase, which results in mixed phase samples. Both of these factors may lead to films with excess residual losses.

Measurements of the optical properties of $Tl_2CaBa_2Cu_2O_8$ films determine the plasma frequency to be $\omega_p \sim 2000\ cm^{-1}$, more than one order of magnitude smaller than obtained in other cuprate superconductors such as YBCO, with $\omega_p \sim 11{,}000\ cm^{-1}$.[116] The optical properties of $Tl_2Ca_2Ba_2Cu_3O_{10}$ films determined from a combination of ellipsometric and reflectivity measurements show strong similarity to YBCO.[117]

4.2. Sample Characterization

The a-b plane oriented Tl-Ba-Ca-Cu-O samples used in this study were grown on $LaAlO_3$ substrates, as summarized in Table 4.1. Samples A and B were produced by 90° off - axis sputtering onto $LaAlO_3$ substrates from sintered targets prepared from oxide powder mixtures with an initial cation

Sample	Institution	thickness (nm)	Nominal Composition	Tc/δT (K)	Deposition Technique	R_s (μΩ)	ρ_n(300 K) (μΩ-cm)
A	IBM	500	2:2:2:3:10	123/1.5	Off-Axis Sputter	84	290
B	IBM	500	2:2:2:3:10	123/1.5	Off-Axis Sputter	84	290
C	STI	700	2:1:2:2:8	100/1.0	Laser Ablation	130	800

Table 4.1 - TCBCO samples measured in this work. Values of microwave surface resistance R_s measured at 4K near 10 GHz are scaled to 10 GHz using an ω^2 law, where ω is the microwave frequency. Films were grown on $LaAlO_3$ substrates. Superconducting transition temperatures are measured from midpoint of transition; transition widths are measured from 10 - 90 % of transition. Approximate values for the dc resistivity ρ_n measured at 300 K are listed for comparison.

ratio of 2Tl:2Ca:2Ba:3Cu. These amorphous precursor films were subsequently wrapped with 2:2:2:3 pellets and post-annealed at ~ 850 °C in order to minimize Tl_2O_3 loss. This technique has been described previously.[115] Film C was prepared by a laser ablation technique followed by a post-deposition thermal process at 830 - 900°C under controlled Tl and oxygen pressure to minimize loss of Tl_2O_3.[118]

Film microstructure for one of the samples (A) was investigated using a four circle x-ray diffractometer. An X-ray θ/2θ scan of the epitaxial nominal $Tl_2Ca_2Ba_2Cu_3O_{10}$ sample A is shown in Fig. 4.1. This scan indicates the presence of both the 2:2:2:3 (filled circles) and the 2:1:2:2 (open circles) phases. Substrate peaks are indicated by "s". The high background counts suggest the presence of some volume fraction of amorphous or randomly oriented polycrystalline grains. Within experimental uncertainty, the x-ray θ/2θ scan indicates that for this film as much as 70% but as little as 30% of the oriented

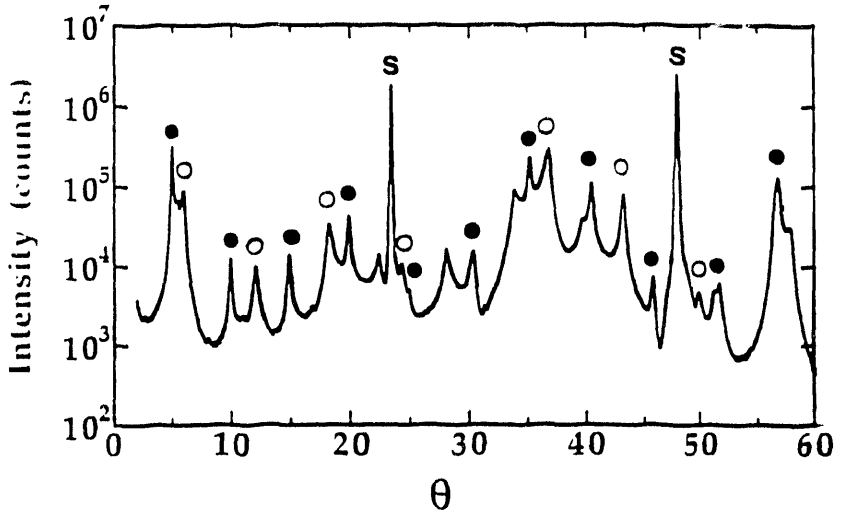

Fig. 4.1 - X-ray θ/2θ scan of the epitaxial nominal $Tl_2Ca_2Ba_2Cu_3O_{10}$ film A, indicating the presence of both the 2:2:2:3 (filled circles) and the 2:1:2:2 (open circles) phases. Substrate peaks are indicated by "s". The high background counts suggest the presence of some volume fraction of amorphous or randomly oriented polycrystalline grains.

material is in the 2:2:2:3:10 phase, with the remainder of the oriented material in the 2:1:2:2 phase, where the c-axis is perpendicular to the substrate surface. X-ray θ/2θ scans on similar films indicates that as much as 80% of the oriented material may be in the 2:2:2:3 phase. However, the relatively high background suggests the presence of some volume fraction of amorphous or randomly oriented polycrystalline grains. An x-ray φ scan on the same film is shown in Fig. 4.2. This X-ray φ scan uses the (1 0 15) peak of $Tl_2Ca_2Ba_2Cu_3O_{10}$ and indicates excellent in plane registry of the oriented 2:2:2:3 phase (upper panel). For comparison, a φ scan using the (1 0 1) peak of the bare $LaAlO_3$ substrate is shown (bottom panel), indicating that the c-axis oriented 2:2:2:3:10 and 2:1:2:2:8 phase material in these films are in excellent registry with the $LaAlO_3$ substrate. X-ray θ/2θ scans on samples nominally identical to sample C indicate that this is a single 2:1:2:2:8 phase film and is c-axis oriented. Sharp

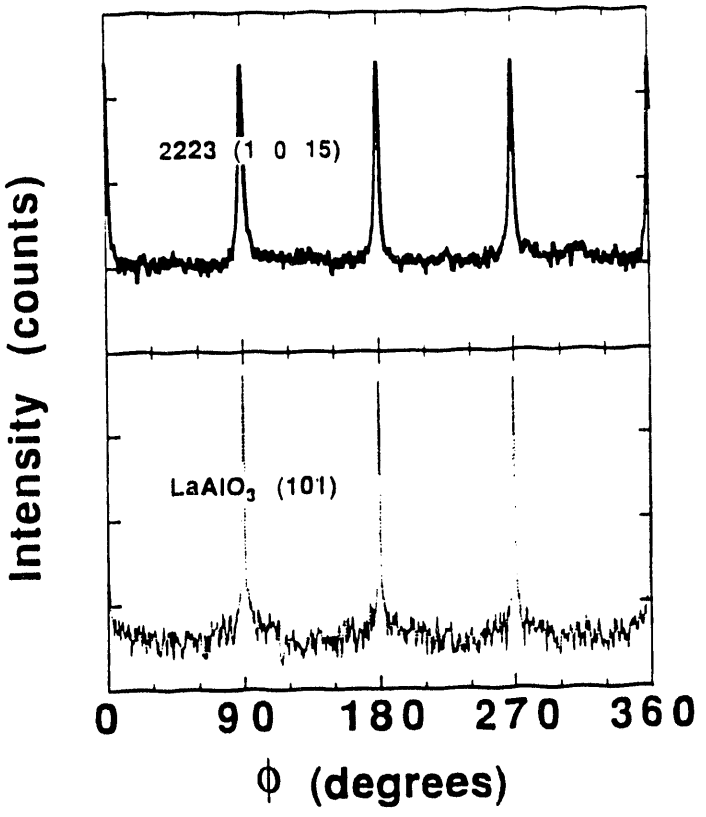

Fig. 4.2 - X-ray φ scan using the (1 0 15) peak of $Tl_2Ca_2Ba_2Cu_3O_{10}$ for the epitaxial film A, indicating excellent in plane registry of the oriented 2:2:2:3 phase (upper panel). For comparison, a φ scan using the (1 0 1) peak of the bare LaAlO3 substrate is shown (bottom panel).

x-ray rocking curves indicate that sample C is epitaxially oriented on the LaAlO3 substrate.[118] Scanning electron microscopy on similar samples show a lateral defect structure in the a-b plane with spacing on the order of ~10 μm. Tunneling electron microscopy on films similar to sample C indicate that these defects have typical depth of ~ 100 nm.

4.3. Microwave Measurements

The microwave surface resistance for samples A and B were measured at 11 - 13 GHz with a parallel plate resonator technique[97] and the microwave

surface resistance for samples A, B and C were measured at 30 and 90 GHz with a confocal resonator technique.[119] We have analyzed the effects of the finite film thickness on the measured optical properties both in the microwave and in the infrared.[99] Because the films we have studied are significantly thicker than typical superconducting penetration depths for TCBCO (~ 150 nm) we do not expect the finite film thickness to affect our measurements.

4.4. Results

The submillimeter absorptivity spectra for epitaxial samples A and B are plotted in Fig. 4.3. The submillimeter spectra contain many phonon modes between 2 and 21 THz. Such phonon structure has previously been observed experimentally in the sintered ceramic sample of Zetterer *et al.*, which is also plotted in Fig. 4.3.[120] Films A and B exhibit remarkably similar structure to that observed in the ceramic sample between 2 and 21 THz. Therefore the agreement with lattice vibration calculations found for the phonon structure from the sintered ceramic[120] should also be valid for the structure we measured on the films. However, the overall absorptivity of the epitaxial films is lower than for the ceramic samples.

The losses for samples A and B are again plotted with the losses for sample C in Fig. 4.4 (solid lines) along with the microwave loss data (filled circles) measured for the same films near 10 K. The curves in Fig. 4.4 are displaced by factors of 10 to avoid overlap. The size of the circles are large enough to include measurement uncertainties and possible corrections for film transparency. The dotted lines in Fig. 4.4 are frequency squared best fits to the microwave data. Losses at low frequencies increase as frequency squared between 10 and 90 GHz and are in good agreement with submillimeter data

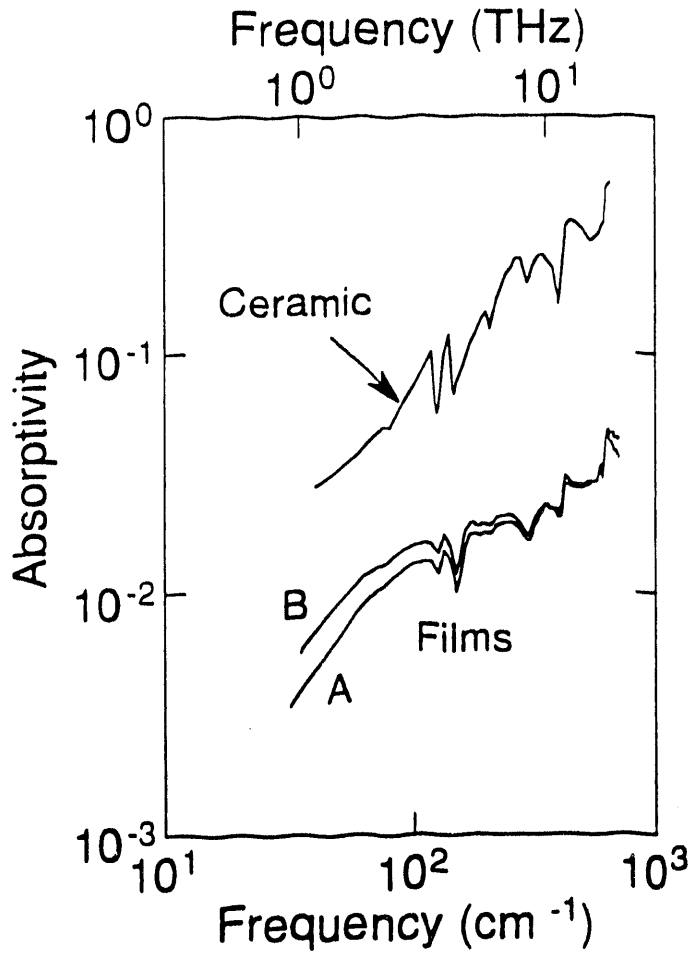

Fig. 4.3 - Submillimeter absorptivity spectra for the epitaxial $Tl_2Ca_2Ba_2Cu_3O_{10}$ samples A and B plotted logarithmically. Note that these films contain some volume fraction of the 2:1:2:2:8 phase. Also shown is the reflectivity measured by Zetterer *et al.* for a $Tl_2Ca_2Ba_2Cu_3O_{10}$ sintered ceramic sample plotted as an absorptivity. All three data sets show 8 phonon modes, in agreement with calculations for 2:2:2:3:10 phase material with E ⊥ c.

for both films. For all thallium films studied, an ω^2 extrapolation of the microwave data passes somewhat above the lowest frequency submillimeter measurements. This suggests that the losses may begin to saturate to the ω^2 limit, which is expected at microwave frequencies for these materials, at somewhat lower frequencies than for the YBCO samples studied in Chapter 3.

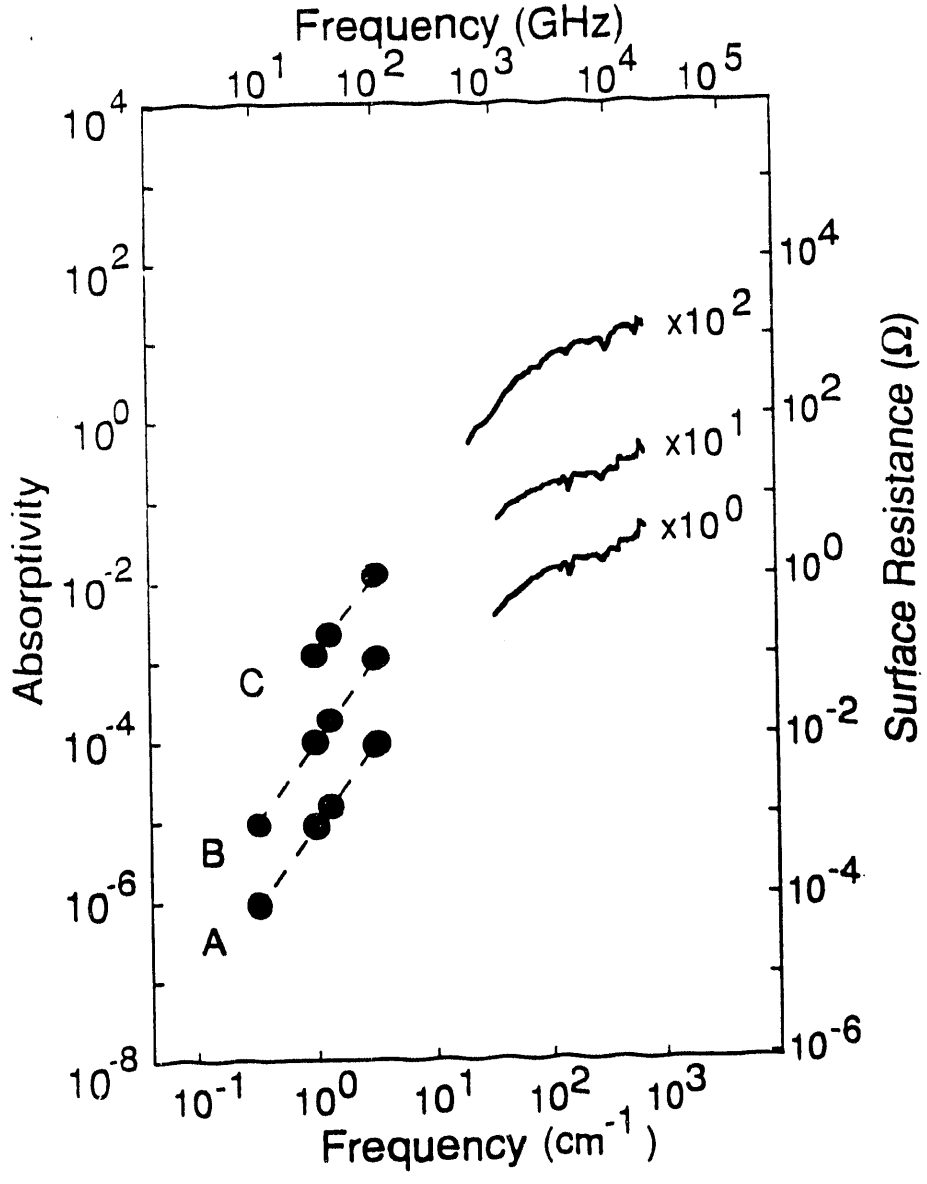

Fig. 4.4 - Measured submillimeter absorptivities of samples A, B and C at 2 K (solid lines) multiplied by the indicated factors to separate the curves. Values of the microwave surface resistance measured for each sample near 4K between 10 and 90 GHz are shown as filled circles. The dotted lines are best fits to the microwave surface resistance data using an ω^2 dependence, where ω is the microwave frequency.

Submillimeter losses for sample C also show strong phonon structure between 30 and 700 cm^{-1} (1 and 21 THz), which is consistent with lattice dynamical calculations.[121] We tentatively attribute the phonon structure in sample C to c-axis modes for the same reasons given for samples A and B. In contrast to samples A and B, the occurrence of this phonon structure is not consistent with the presence of randomly oriented grains, since x-ray rocking curve studies suggest that film C is highly epitaxial. However, there is considerable surface roughness in these films, with typical dimension of approximately 100 nm. In this case current induced in the a-b plane by the incident fields could cause current to be driven along the c direction which explain the presence of these c-axis phonon modes.

4.5. Analysis

We expect the high conductivity of the a-b plane to screen out phonon excitations with vibrational motion in the a-b plane. We therefore believe that the phonon modes observed in epitaxial films A and B correspond to infrared active excitations perpendicular to the a-b plane. The observed phonon structure is in agreement with a lattice dynamical study which show the existence of 8 phonon modes for 2:2:2:3 phase material with E | | c.[121] Since the incident fields probing the sample in our measurement are predominantly parallel to the surface of the film, the plausible identification of the observed structure to E | | c phonon modes suggest the presence either of a substantial fraction of the film containing grains whose c-axis is not perpendicular to the film surface or of considerable surface roughness which would cause current to be driven along the c direction. For samples A and B, the former possibility is consistent with the observation of a large background in the x-ray $\theta/2\theta$ scan measured for sample A.

4.6. Conclusions

We have characterized the residual loss in epitaxial a-b plane films of $Tl_2CaBa_2Cu_2O_8$ and mixed phase $Tl_2Ca_2Ba_2Cu_3O_{10}$ and $Tl_2CaBa_2Cu_2O_8$ films from 0.3 cm^{-1} (10 GHz) to 700 cm^{-1} (21 THz). We do not observe any gap-like features below for any of the films studied. For all films studied the losses below ~ 1 THz scale approximately as frequency squared.

We are unable to fit the losses in the Tl-Ba-Ca-Cu-O films to the weakly coupled grain model. We observe strong phonon structure in all Tl-Ba-Ca-Cu-O films between 30 and 700 cm^{-1}. This is in strong contrast to the case for other high T_c superconductors such as $YBa_2Cu_3O_7$, where phonon structure observed in ceramic samples is absent in epitaxial oriented films and crystals because of the electronic screening due to the high conductivity of the a-b planes. From comparison of our data to lattice dynamical studies and to reflectivity data on ceramic samples of $Tl_2Ca_2Ba_2Cu_3O_{10}$ we have been able to identify the eight phonon features seen in the measured absorptivities of samples A and B with c-axis phonon modes. In agreement with the analysis of the background scattering data from x-ray measurements this implies that Samples A and B contain some volume fraction of amorphous or randomly oriented polycrystalline material.

5. Direct Submillimeter Absorptivity Measurements on Epitaxial $Ba_{1-x}K_xBiO_3$ Films at 2K

We have used a bolometric technique to obtain accurate low temperature loss data for epitaxial thin films of $Ba_{0.6}K_{0.4}BiO_3$ from 30 cm^{-1} to 700 cm^{-1} at 2 K. These films were grown on MgO and $SrTiO_3$ substrates by MBE, off-axis sputtering and laser deposition techniques. All films show a strong absorption onset near the BCS tunneling gap of $3.5k_BT_c$. We have analyzed these data using a Kramers-Kronig transformation and have corrected for finite film thickness effects. Our results indicate that the absorption onset is consistent with a superconducting energy gap. Comparison is made with predictions based on strong coupling Eliashberg theory using $\alpha^2F(\omega)$ spectra obtained from the literature. While we are able to fit the overall measured absorptivity, we are unable to fit the structure observed in our data.

5.1. Introduction

The oxide superconductor $Ba_{1-x}K_xBiO_3$ (BKBO) is an interesting system because of its differences to other high-T_c materials. BKBO has a cubic structure in contrast to the cuprate superconductors, which are highly anisotropic. The parent compound of BKBO shows charge density wave ordering[122] rather than the antiferromagnetic ordering seen for example in the undoped parent compound of $YBa_2Cu_3O_{6+x}$(YBCO), i.e., for x = 0. The exchange of antiferromagnetic spin fluctuations has been discussed as a pairing mechanism in YBCO.[123] Fluctuation exchange mechanisms related to the charge density wave state have also been proposed for the pairing mechanism in BKBO.[122] Tunneling measurements have shown evidence for an energy gap and a BCS density of states in BKBO,[124-126] but not in YBCO. Reflectivity measurements on BKBO thin films show features which have been interpreted as a superconducting gap.[127]

5.2. Sample Characterization

In this work we have measured the absorptivities of three BKBO films with x ~ 0.4, listed in Table 5.1. Sample A was grown using a two step molecular beam epitaxy technique.[128] In this technique a film without potassium is first nucleated on the MgO substrate. The BKBO is subsequently grown on the potassium deficient film. This process allows epitaxial BKBO films to be grown at a low temperature. Sample B was grown with an *in situ* pulsed laser deposition technique[129] using stochiometric targets. These films exhibit good in-plane epitaxy, as studied by x-ray scattering. Sample C was grown using an *in situ* off-axis magnetron sputtering technique.[130] All films used in this study are nominally single phase and oriented in a mixture of the (100) and (110) directions.

Increasing the oxygen content has been observed to shrink the lattice

	Institution	Growth	Thickness	Substrate	T_c
A	AT&T	MBE	350 nm	MgO	15 (20) K
B	U. Illinois	Laser Deposition	300 nm	MgO	22 (28) K
C	H.P.	Off-axis Sputtering	400 nm	$SrTiO_3$	19 (21) K

Table 5.1 - List of samples used in this study. T_c values correspond to the low temperature end of the transition as measured by an ac susceptibility technique. The onset of the transition is given in parentheses.

parameter. It has been suggested that the oxygen content of the BKBO films increases on cooling,[128] resulting in lattice shrinkage and cracking. Cracking of the BKBO films is a significant problem,[128,129] which can be reduced by minimizing film thickness.

5.3. Results

The measured absorptivities for the three films are displayed in Fig. 5.1. The BKBO absorptivities are larger than for a high quality epitaxial YBCO film, with x~ 1, which is also shown in Fig. 5.1 for comparison. The YBCO absorptivity shown in Fig. 5.1 is for sample A from Chapter 3. Large sample to sample variations are present among the absorptivities for the three BKBO films. However, there are similar structures present for all films. There are steps in the absorptivity at 525 cm^{-1} and near 300 cm^{-1} . There is also a strong absorption onset observed for all films near the tunneling gap at $2\Delta = 3.5\ k_B T_c$.[124] However, the frequencies of the observed absorption onsets do not scale with the measured T_c values as listed in Table 5.1.

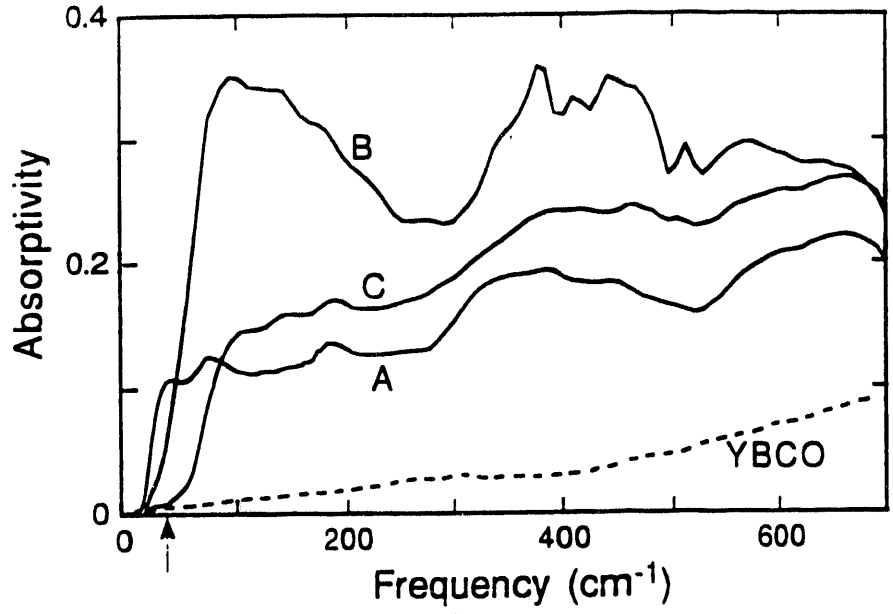

Fig. 5.1 - Measured absorptivities of films A, B and C at 2K. The measured absorptivity of a $YBa_2Cu_3O_7$ film (dotted line) is also shown for comparison. The arrow indicates the approximate tunneling gap value of $2\Delta = 3.5\ k_BT_c$ for film A. The frequencies of the observed absorption onsets do not scale with the measured T_c values as listed in Table 5.1.

5.4. Analysis

Two distinct physical phenomenon, a zero crossing of $\varepsilon_1(\omega)$ or an onset in $\sigma_1(\omega)$ can give rise to an onset of absorption. The former corresponds to a plasma edge; the latter to a superconducting gap. For example, an onset is observed in the absorption of polycrystalline $La_{1.85}Sr_{0.15}CuO_4$ near 50 cm^{-1} which is due to a plasma edge. Historically this feature was confused with a superconducting gap.[131] In order to understand the significance of the low frequency absorption onset it is necessary to obtain information about both $\varepsilon_1(\omega)$ and $\sigma_1(\omega)$.

We can estimate the London penetration depth in BKBO as $\lambda_L = c/\omega_p \sim$ 125 nm, where c is the speed of light and $\omega_p = 1.59$ eV is the optically determined plasma frequency.[132] Because the films used in this study are only slightly

thicker than λ_L we expect that some radiation will be transmitted through the films, so that the measured absorptivity will now contain contributions from the film/substrate interface and from the reflections off the back surface of the substrate. In the following section we argue that not resolving the interference pattern due to reflections off the back surface of the substrate is equivalent to ignoring the finite thickness of the substrate. We then analyze the equivalent but simpler system of the thin film on a semi-infinite substrate in order to determine the properties of the film independent of the film thickness.

5.4.1. Understanding the Absorption of a partially Transparent Film

Light at two points in space and time which is in principle capable of being superimposed to produce interference effects is said to be coherent. Radiation from a blackbody source such as the one used in our measurement can be characterized by a coherence time τ_c or equivalently a coherence length $l_c = c\tau_c$.[133] The potential magnitude of the interference effects in our measurement is governed by the first-order coherence of the light.[133] Radiation at two points (z_1,t_1) and (z_2,t_2) is first-order coherent only if $|c(t_2 - t_1) - z_2 - z_1| << l_c$.

Consider radiation emitted from a Michelson interferometer impinging on a partially transparent film which is on a substrate of index n and thickness t. The interferogram corresponding to power absorbed in the film/substrate system as a function of mirror travel δ will consist of several repeating interference patterns. The central interference pattern corresponding to $\delta = 0$ contains information about the front film/substrate interface. Subsequent interference patterns will occur about $\delta = m(2nt)$ for m = 1,2,3,... and will contain information about both the front film/substrate interface and the back substrate interface, in addition to information about the substrate itself. If the coherence length of the incident radiation is less than twice the optical thickness of the substrate, i.e. if l_c

$< 2nt$, then there is no way for radiation interacting with the back surface of the substrate to coherently interfere with radiation interacting with the front surface of the substrate. Therefore, the interference patterns occurring about $\delta = m(2nt)$ for m = 0,1,2,3,... are independent of each other, and the central interference pattern corresponding to $\delta = 0$ can be used independently of the other interference patterns to study the front film/substrate interface. Conversely, if $l_c > 2nt$ then the individual interference patterns occurring about $\delta = m(2nt)$ for m = 0,1,2,3,... overlap and cannot be studied independently from each other.

We can easily estimate the coherence length l_c of our radiation source since the modulus of the first-order coherence function is just the envelope of the interferogram, which is directly measured in our experiment. That is, l_c is just the optical path length δ that the mirror in the Michelson interferometer moves beyond which no interference fringes appear. Under the conditions of our measurement, we find $l_c \sim 0.1$ cm. For a typical substrate used in our measurement, $t \sim 0.05$ cm and $n \sim 4$ so that $2nt \sim 0.4$ cm, less than l_c.

5.4.2. Deconvolving Effects Due to Finite Film Thickness

From the results of the previous section we have shown that by ignoring the interference fringes due to reflection off the back surface of the substrate we are able to treat the optical properties of a partially transparent film on a substrate as if the substrate were semi-infinite, provided $l_c < 2nt$. If we know both the optical properties of the substrate and the film thickness then we can deconvolve the effects due to the substrate from the measured absorptivity. This results in the determination of the optical properties of the film independent of the substrate.

We do this in the following way. We calculate the complex pseudo-dielectric function $\langle\varepsilon(\omega)\rangle$. (The brackets here are simply to denote pseudo-

quantities, e.g., including finite film thickness effects, and is not related to time averaging.) This is just the dielectric function obtained from the Kramers-Kronig transform of the measured low resolution absorptivity spectrum. The pseudo-dielectric function includes finite film thickness effects. We can then define the complex reflection coefficient for the thin film on the semi-infinite substrate as

$$r(\omega) = \frac{\sqrt{<\varepsilon(\omega)>} - 1}{\sqrt{<\varepsilon(\omega)>} + 1}. \qquad (5.1)$$

Now the complex reflection coefficient $r(\omega)$ of a thin film on a semi-infinite medium is given by[134]

$$r(\omega) = r_{12}(\omega) + \frac{t_{12}(\omega)t_{21}(\omega)r_{23}(\omega)e^{i\Delta}}{1 - r_{23}(\omega)r_{21}(\omega)e^{i\Delta}}, \qquad (5.2)$$

where $r(\omega)_{ij} = (n_i(\omega) - n_j(\omega))/(n_i(\omega) + n_j(\omega))$, $t(\omega)_{ij} = 2n_i(\omega)/(n_i(\omega) + n_j(\omega))$, $\Delta = 2n_2(\omega)d\,w/c$, d is the film thickness, ω is the frequency, c is the speed of light, $n_i(\omega)$ is the complex refractive index for medium i and the indices i = 1,2 and 3 correspond to free space, the film and the substrate, respectively. The quantity $r(\omega)$ is the same in Equations 5.1 and 5.2, and is a function of the refractive index of both the substrate $n_{substrate}(\omega)$ and film $n_{film}(\omega)$ and of the film thickness d. Provided we know $n_{substrate}(\omega)$ and the film thickness d we can invert Eq. 5.2 and solve for $n_{film}(\omega)$.

Inverting Eq. 5.2 amounts to simultaneously solving two non-linear equations corresponding to the real and imaginary components of $r(\omega)$. Unlike minimizing χ^2 for an N dimensional function, where the gradient of the function defines an N dimensional surface which is smoothly connected to the minimum, simultaneous root solving of non-linear equations relies crucially on the quality

of the initial guess.[105] In the secant method of root finding the equations are linearized about an initial guess and the root of the coupled linear equations is calculated. The process is repeated using the new root until the solution converges.

The initial guess used to invert Eq. 5.2 relies on the fact that (a) when the film thickness d is extremely large, the value for $n_{film}(\omega)$ that satisfies Eq. 5.2 must be exactly $<\varepsilon(\omega)>^{1/2}$ and that (b) Eq. 5.2 varies smoothly with d. So we start with an artificially large value of d using $n_{film}(\omega) = <\varepsilon(\omega)>^{1/2}$ as the initial guess. Once a solution is found, d is decreased and a new root is found using the previous solution. This process continues until d converges to its actual value.

5.4.3. Discussion of Analysis

In what follows we describe our results for film A. Similar results are obtained for film B, also grown on an MgO substrate for which the FIR properties are described in the literature.[135] Film C, deposited on a $SrTiO_3$ substrate , poses a special problem, as the low temperature (~4K) FIR properties of this ferroelectric material are not adequately described in the literature.

We compute the Kramers-Kronig (KK) transform for film A using high frequency data measured up to 5 eV on a nominally identical sample.[39] Ellipsometric data, which gives both real and imaginary components to the conductivity at high frequencies, is used to correct the results of our KK analysis, as discussed in Sec. 1.3. We use the results of the KK transform above ~30 cm^{-1} , which are independent of the low frequency extrapolation used.

5.4.4. Results

The pseudo- functions $<\sigma_1(\omega)>$ and $<\varepsilon_1(\omega)>$ and the inferred functions $\sigma_1(\omega)$ and $\varepsilon_1(\omega)$ for BKBO (without and with finite film thickness correction) are

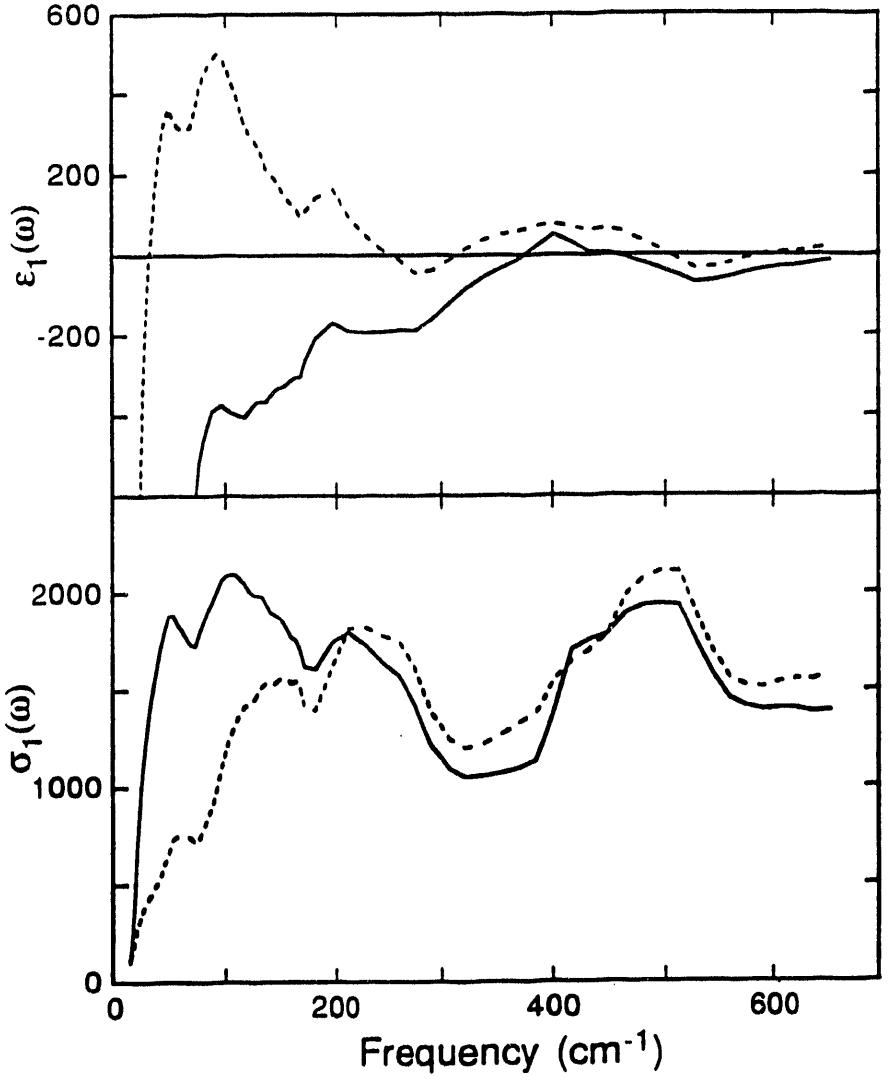

Fig. 5.2 - (a) Pseudo-dielectric function $<\varepsilon_1(\omega)>$ (dotted line) and inferred dielectric function $\varepsilon_1(\omega)$ (solid line) for film A. The pseudo-dielectric function is derived from the Kramers-Kronig transform of the measured absorptivity and is therefore not corrected for finite film thickness effects. The inferred dielectric function $\varepsilon_1(\omega)$ is corrected for the finite film thickness. The feature near 400 cm^{-1} may be due to a strong absorption band in the MgO substrate, which we are unable to remove from our data. (b) Pseudo-conductivity $<\sigma_1(\omega)>$ (dotted line) and inferred conductivity $\sigma_1(\omega)$ (solid line) for film A.

shown in Fig. 5.2 as dotted and solid lines, respectively. The pseudo-dielectric function $<\varepsilon_1(\omega)>$ in Fig. 5.2(a) crosses zero near the frequency of the low

frequency absorption onset. However $\varepsilon_1(\omega)$, which is corrected for the finite film thickness, does not cross zero near the absorption onset, indicating that the absorption onset is not a plasma edge, and may be a superconducting gap. The low frequency onset in the pseudo-conductivity $<\sigma_1(\omega)>$ also becomes more steep in $\sigma_1(\omega)$, as shown in Fig. 5.2(b). The increase in the slope of $\sigma_1(\omega)$ is consistent with our interpretation of this feature as a superconducting gap.

The presence of a zero crossing in $\varepsilon_1(\omega)$ at 400 cm^{-1} is near a strong absorption feature in the MgO substrate, and may be an artifact resulting from the technique for correcting finite film thickness effects. For example, if the film is not uniformly thick then we do not expect the inversion technique to work well. We also expect that such errors will be pronounced in the vicinity of a strong substrate absorption band, such as occurs near 400 cm^{-1}.

The absorptivity of BKBO (corrected for the finite film thickness) is shown in Fig. 5.3(a) as a dotted line. The measured absorptivity for the same sample, not corrected for finite film thickness effects, is shown again for comparison as a dashed line. The feature near 400 cm^{-1} may be due to the strong absorption in the MgO substrate. The remaining structure appears to be a real property of BKBO.

5.4.5. Eliashberg Strong Coupling Calculation

It is useful to investigate whether the structure observed in Fig. 5.3(a) is due to phonons via the Holstein effect,[33] expected in a strong coupling superconductor. In order to explore this question we compare our data to an Eliashberg strong coupling calculation.[40] We use the experimental plasma frequency ω_p = 1.59 eV[132], $\alpha^2F(\omega)$ from tunneling measurements[125] and various values of the impurity scattering rate $1/\tau_i = \hbar\Gamma$, as shown in Fig. 5.3(b). In the clean limit ($\hbar\Gamma = 0$) no absorption onset is observed. As the impurity scattering rate increases, an absorption onset appears. Structure present in the calculated

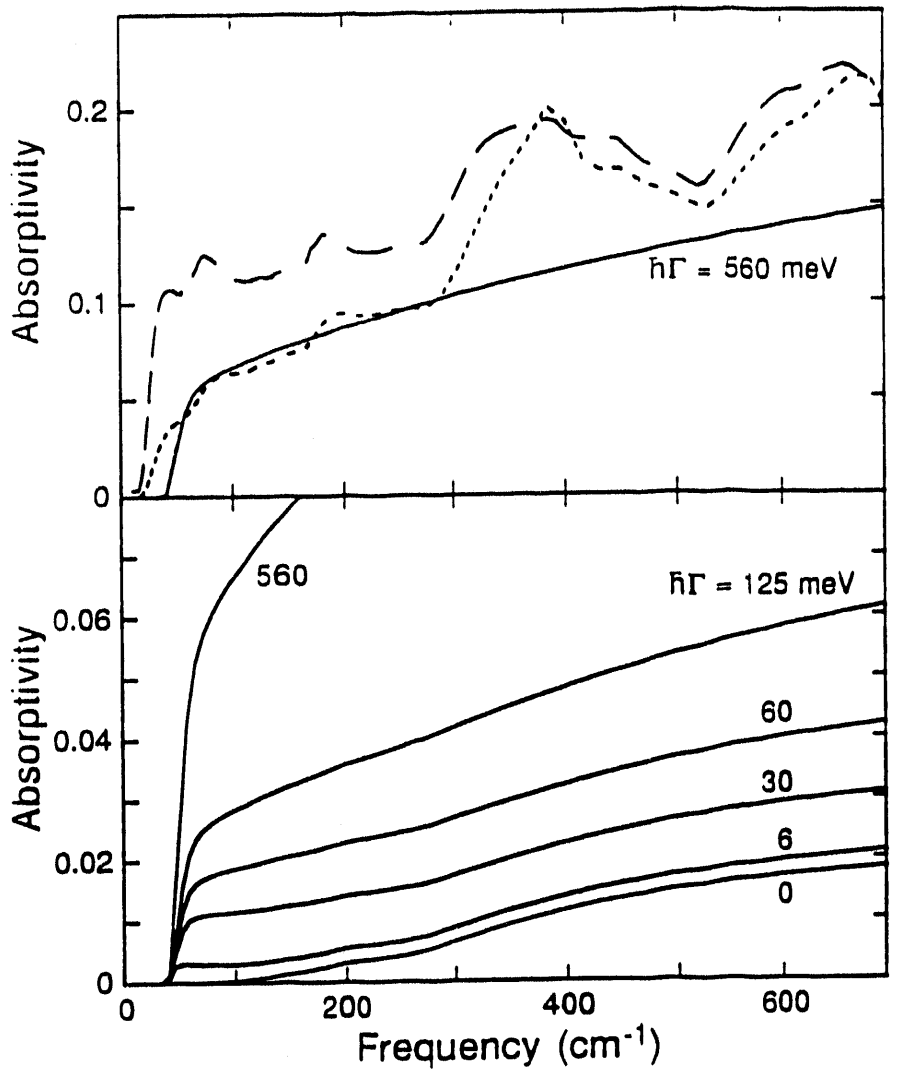

Fig. 5.3 - (a) The dotted line is the absorptivity of film A corrected for finite film thickness effects. The feature near 400 cm^{-1} may be due to a strong absorption band in the MgO substrate, which we are unable to remove from our data. The uncorrected absorptivity for sample A is also shown for comparison as the dashed line. The solid line is a fit to the data using the strong coupling Eliashberg theory with $\omega_p = 1.59$ eV, $\varepsilon_\infty = 3.8$ and $\hbar\Gamma = 560$ meV. (b) Results of the strong coupling Eliashberg theory with $\omega_p = 1.59$ eV, $\varepsilon_\infty = 3.8$ and $\hbar\Gamma = 0$, 6, 30, 60, 125 and 560 meV. Note that as $\hbar\Gamma$ increases, the Holstein structure due to phonon modes is washed out.

absorptivity due to phonon modes gets washed out as the scattering rate increases.

In order to fit the absolute value of the absorptivity, the inelastic scattering rate used in the Eliashberg calculation is so large ($\hbar\Gamma$ = 560 meV) that all features due to electron-phonon coupling are washed out. Inelastic scattering rates determined from reflectivity measurements range from 250 meV[127] to 900 meV,[132] in rough agreement with scattering rates from our best fits.

Although we do not understand the nature of the features observed in the corrected BKBO absorptivity in Fig. 5.3(a), it is interesting to speculate on possible origins. These features which the model is not able to fit may be due to the presence of insulating regions in the film,[136] corresponding to optical features of the insulating phases of $Ba_{1-x}K_xBiO_3$. Further study of the insulating phases of BKBO could clarify the nature of these features.

The Eliashberg calculation used to fit our data assumes local electrodynamics. We can check this assumption by estimating the quantity l/δ, where l is the electronic mean free path and δ is the skin depth. We approximate $l/\delta \sim v_F\tau_i/\lambda \sim 0.01$ where $v_F \sim 10^8$ cm s^{-1} is an upper limit on the Fermi velocity[59], $\lambda \sim 125$ nm is the superconducting penetration depth and $\tau_i = \Gamma^{-1}$ is the impurity scattering time from the best fit. Since $l/\delta \sim 0.01 << 1$ our assumption of local electrodynamics is justified.

5.5. Conclusions

We have directly measured the FIR absorptivity for three $Ba_{1-x}K_xBiO_3$ films at 2K. The measured absorptivities are significantly larger than for $YBa_2Cu_3O_7$ at the same temperature. In addition, there is considerable sample to sample variation among the films. We observe absorption onsets near 3.5 k_BT_c (~40 cm^{-1}) for all films which do not scale with T_c, as well as pronounced

structure at higher frequencies. After performing a Kramers-Kronig analysis and correcting for finite film thickness, we find that the absorption onset is consistent with a superconducting gap. Further measurements using thick films or single crystals are necessary to eliminate uncertainties associated with the finite film thickness correction. A strong coupling Eliashberg calculation does not account for the structure observed in the optical properties. This structure may be due to the presence of insulating regions in the film.[136]

6. Magnetic Field Effects

We have studied the dependence of magnetic field on directly measured absorptivities in epitaxial films of $YBa_2Cu_3O_7$. These measurements were made at 2K in fields up to 3 Tesla and for frequencies between 50 cm^{-1} and 200 cm^{-1}. Several models for the field dependent complex conductivity $\sigma(\omega;H)$ are discussed, and an attempt is made to fit the absorptivity data using these models.

6.1. Introduction

The high-T_c cuprates are extreme type II superconductors with the Ginzburg-Landau parameter $\kappa = \lambda/\xi >> 1$. For strongly type II superconductors the surface energy of a superconductor in a magnetic field is negative. A consequence is that magnetic flux does not penetrate the superconductor in laminar domains but instead in a regular array of flux tubes. Each flux tube, or vortex, carries the flux quantum $\Phi_0 = hc/2e$. The electrodynamics of Type-II superconductors in the mixed state, e.g., $H_{c1} < H < H_{c2}$ is determined by the dynamics of these vortices. In this chapter we will use several models to gain insight into the dynamics of the mixed state, and compare predictions of these models with absorptivities measured with and without a magnetic field.

The usual picture of loss in the mixed state is that phase slip from vortex motion normal to the supercurrent gives rise to an emf parallel to the current, resulting in dissipation. In another picture the vortices represent regions of reduced order parameter. Quasiparticle excitations within the vortex normal

cores gives rise to dissipation. The model of Karrai *et al.*[28] treats the intra-vortex excitations, while the model of Hsu *et al.*[29,30] treats both the vortex motion and the intra-vortex quasiparticle excitations.

6.1.1. Expressing $\sigma(\omega;H)$ in terms of $A(\omega;H)/A(\omega;0)$ and $T(H)/T(\omega;0)$

In the analysis below we want to completely describe the complex response function $\sigma(\omega;H)$ of the models we are studying. We have measured absorptivities which we express as the ratio $A(\omega;H)/A(\omega;0)$, so we would also like to compare the results of our modeling with the measured data. One way of specifying the complex response function is by calculating both the absorptivity ratio $A(\omega;H)/A(\omega;0)$ and the transmissivity ratio $T(\omega;H)/T(\omega;0)$, as shown below. The absorptivities are calculated assuming the sample is much thicker than the penetration depth. The transmissivities are calculated for a thin film on a dielectric substrate using the thin film approximation, as

$$T(\omega) = \frac{4n}{\left| n + 1 + \frac{4\pi}{c} t\ \sigma(\omega) \right|^2} \qquad (6.1)$$

where n is the substrate refractive index, t is the film thickness and $\sigma(\omega)$ is the film conductivity. In all calculations of the transmissivity we arbitrarily use n=4, corresponding to an MgO substrate, and t = 600Å. The precise values for these parameters do not alter our results.

The ratio $A(\omega;H)/A(\omega;0)$ is nearly identical to the ratio $\sigma_1(\omega;H)/\sigma_0$ and the ratio $T(\omega;H)/T(\omega;0)$ is nearly identical to the ratio $[\lambda_1(\omega;H)/\lambda_0]^4$, where $\sigma_0 = \sigma_1(0;0)$. The quantity $\lambda_1(\omega;H)$ is the real part of the effective superconducting penetration depth defined as

$$\lambda_1(\omega;H) = \sqrt{\frac{c^2}{4\pi\sigma_2(\omega;H)\omega}} \quad , \qquad (6.2)$$

where $\sigma_2(\omega;H) = \mathrm{Im}[\sigma(\omega;H)]$ and $\lambda_0 = \lambda_1(0;0)$.

At low frequencies the absorptivity $A(\omega;H) \sim (\pi/c)R_s \propto \omega^2\lambda_1^3(\omega;H)\sigma_1(\omega;H)$ so that $A(\omega;H)/A(\omega;0) \sim \lambda_1^3(\omega;H)\sigma_1(\omega;H)/\lambda_0^3\sigma_0$, where we have made the approximations $\sigma_0 \sim \sigma_1(\omega;0)$ and $\lambda_0 \sim \lambda_1(\omega;0)$. For the systems we have studied, $\lambda_1(\omega;H)$ changes by only a few percent as $\sigma_1(\omega;H)$ changes by as much as several hundred percent so that the ratio $A(\omega;H)/A(\omega;0) \sim \sigma_1(\omega;H)/\sigma_0$.

From Eq. 6.1 it can be seen that for large $|\sigma(\omega;H)|$, $T(\omega;H)/T(\omega;0) \sim |\sigma(\omega;0)/\sigma(\omega;H)|^2 \sim [\lambda_1(\omega;H)/\lambda_0]^4$, where the last relationship holds since $\lambda_1^{-2}(\omega;H) \propto \sigma_2(\omega;H) >> \sigma_1(\omega;H)$.

Therefore the ratios $A(\omega;H)/A(\omega;0)$ and $T(\omega;H)/T(\omega;0)$ specify $\sigma_1(\omega;H)$ and $\lambda_1(\omega;H)$ which in turn completely specify the complex response function $\sigma(\omega;H)$.

6.2. Models for $\sigma(\omega;H)$

In this section we introduce several models for the conductivity. One way of gaining physical insight into the models we use is to analyze the distribution of oscillator strength $\mathcal{A}$ as a function of magnetic field. The quantity $\mathcal{A}$ depends only on the intrinsic parameters n, e and m and therefore is conserved independent of extrinsic factors such as temperature or magnetic field. We will use the definitions for $\mathcal{A}$, $\mathcal{A}_s$ and $\mathcal{A}_n$ defined in Sec. 1.2.3.

6.2.1. Two-Fluid Model

For completeness we will first discuss the effects of a magnetic field on the two-fluid model which was already introduced in Section 3.5.2. To begin with,

we can look at the effect of a magnetic field on the normal, Drude, component of the conductivity. In a magnetic field with H along $\hat{z}$ the conductivity tensor of an isotropic medium can be expressed in terms of $\sigma^{xx}(\omega)$ and $\sigma^{xy}(\omega)$ where

$$\sigma^{xx}(\omega) = \frac{\sigma_0 (1 - i\,\omega\tau)}{(1 - i\,\omega\tau)^2 + (\omega_c\tau)^2},$$
$$\sigma^{xy}(\omega) = \frac{\sigma_0 (\omega_c\tau)}{(1 - i\,\omega\tau)^2 + (\omega_c\tau)^2}, \qquad (6.6)$$

and where σ_0 is the dc conductivity and $1/\tau$ the scattering rate of the normal fluid. The matrix elements $\sigma^{yy}(\omega) = \sigma^{xx}(\omega)$ and $\sigma^{yx}(\omega) = -\sigma^{xy}(\omega)$. The cyclotron resonance $\omega_c = eH/mc$. The response of the medium to unpolarized light is simply $\sigma(\omega) = \sigma^{xx}(\omega)$. The response of the medium to circularly polarized light is $\sigma^{\pm}(\omega) = \sigma^{xx}(\omega) \pm i\,\sigma^{xy}(\omega)$. For H = 1 T and e and m the charge and mass of a free electron, respectively, $\omega_c \sim 600$ MHz. In order to clearly resolve the cyclotron resonance, $\omega_c\tau >> 1$.

It is easy to show by numerical integration that the oscillator strength of $\sigma^{xx}(\omega)$ is independent of H. The conductivity in the TF model is $\sigma(\omega) = \sigma^{xx}(\omega) + ic^2/4\pi\lambda^2\omega$, so because total oscillator strength is conserved this implies λ is independent of H in the TF model. So in the two fluid model as described above, the effect of a magnetic field is to distort the normal component while leaving the superconducting condensate unaffected. For the systems we have studied and for the maximum magnetic fields used in our measurement, $\omega_c\tau << 1$ so that the effect of the magnetic field on the two-fluid model is negligible.

6.2.2. Weakly Coupled Grain Model

In a granular superconductor magnetic vortices can either be present either within the grains or within the intergranular region. If the dominant loss mechanism is due to vortex motion then it is critical to account for both grain-pinned and intergranular vortices using some effective field,[137] as

$$B_{eff} = (n_j + x\, n_g) \Phi_0 \quad , \tag{6.7}$$

where n_g is the density of vortices pinned somewhere within a grain, n_j is the density of vortices which do not pass through grains and x is the average fractional length of a grain pinned vortex which actually lies within a grain. We would expect x to be dependent on the morphology of the sample, with x the fraction of intergranular to total sample volume. Experimentally the problem is quite complicated, with n_j and n_g field, history and time dependent.[137] In addition, flux viscocities within the grain boundaries are estimated to be orders of magnitude smaller than within the grains,[138] also necessitating separate treatment of the grain-pinned and intergranular vortices.

The weakly-coupled-grain (WCG) model introduced in Sec. 3.5.3 provides us with a simplistic way of describing the loss mechanism in granular superconductors. The implicit assumption made in the WCG model that an effective continuum conductivity can be used to describe a discontinuous medium is equivalent to assuming that the currents, or fields, are uniform across the profile of a grain. This will be true provided $\lambda >> a$, the grain size. From the results of Chapter 3 we have found that $\lambda >> a$, so that to first order we are justified in using the WCG model to understand how magnetic flux interacts with granular superconductors.

We start by examining the effect of field on an isolated Josephson junction. Flux normal to the junction will thread the region between the two

superconductors, and induce a spatially varying phase difference along the junction, modulating the junction critical current as

$$I_c(\Phi) = I_{c0}\left|\frac{\sin(\pi\Phi/\Phi_0)}{(\pi\Phi/\Phi_0)}\right| \quad , \qquad (6.8)$$

where I_{c0} is the maximum critical current and Φ is the total flux through the junction. This equation neglects self-field effects, and should be applicable to small junctions.[63] For an array of junctions of varying dimensions which are randomly oriented with respect to magnetic field we would on average not expect to see the behavior of Eq. 6.8, shown in Fig. 6.1 as the solid line, since it is unlikely that the applied flux could cancel out the critical current in all junctions simultaneously. Rather, the qualitative shape of Eq. 6.8 would be preserved, while eliminating the nodes, and might look something like the dotted line in Fig. 6.1.

As the field applied normal to the superconducting film increases, the average critical current through the junction decreases. In terms of the RSJ equivalent circuit representation of the WCG model given in Fig. 3.5, this would lead to an increasing Josephson inductance $L_j = \mathcal{L}_j / a = \hbar/2eI_c(H)$, where I_c is now a function of H. The quantity a is the grain size, and is the only length scale associated with the microstructure of the film which enters into the WCG model. As L_j increases, more current is driven through the Josephson resistance $R_j = \rho_j/a$ hence we expect the loss to increase. The loss relative to zero field increases only at low frequencies. Above some cutoff frequency $\omega_{cutoff} = R_j/L_j$ the junction behavior is already dominated by the resistive component of the junction. For sample A of Chapter 3, $\omega_{cutoff} = 180\ cm^{-1}$.

We can calculate the optical response of the film to an applied field by estimating the amount of flux which passes through each Josephson junction

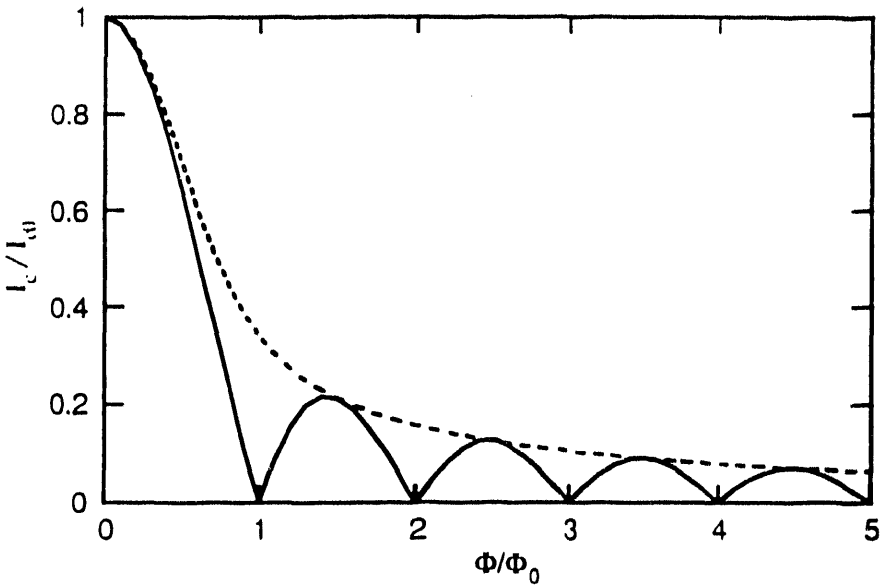

Fig. 6.1 - Normalized critical current I_c/I_{c0} through an ideal, isolated Josephson junction as a function of Φ, the total magnetic flux through the junction (solid line). The bounding curve (dotted line) is an approximation given by $I_c/I_{c0}(z) = (1 + 0.05\, z^3) / (1 + 0.167\, z^2 + 0.05\, z^4)$ with $z = \pi\, \Phi / \Phi_0$, where $\Phi_0 = hc/2e$ is the flux quantum.

element. The number of fluxons passing through each junction is $n = \Phi/\Phi_0 \sim Ha^2/4\Phi_0$, where H is the applied field. We have assumed that the magnetic flux in the film is present only in the intergrain regions. The factor of 4 comes from the 4 sides of each grain which can act as a junction. If we do not include this factor of 4 the resulting calculated absorptivity ratios are significantly larger. Note that for all films studied in Chapter 3, the Josephson penetration depth $\lambda_j >> a$, implying uniform penetration of the magnetic flux within the junction. Using the value of the grain dimension a = 40 nm for sample A from Table 3.1 we find $\Phi/\Phi_0 \sim 0.2$ fluxons per junction for a field of 1 Tesla. Note that the dimensions of the intergrain region do not explicitly enter the problem.

Knowing Φ/Φ_0 as a function of H and knowing the functional relationship between H and I_c, given as the dotted line in Fig. 6.1, allows us to

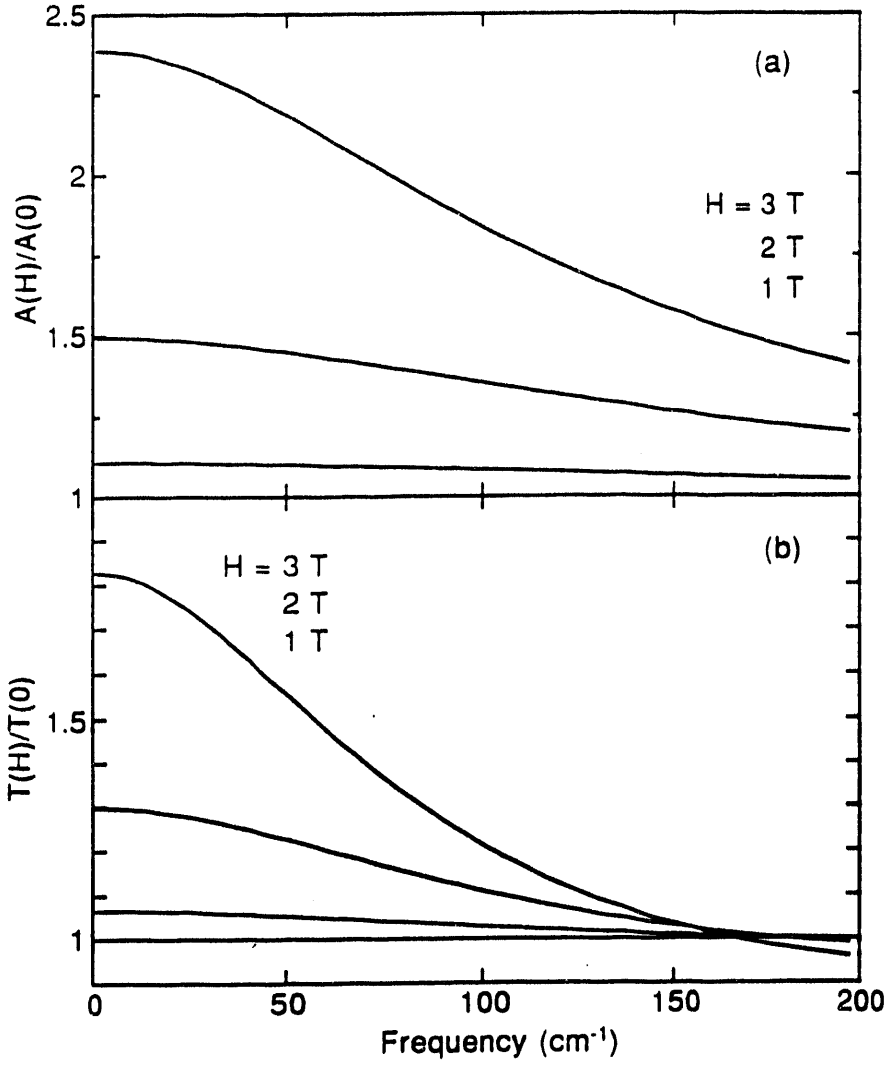

Fig. 6.2 - (a) The absorptivity ratio $A(\omega;H)/A(\omega;0)$ and (b) the transmissivity ratio $T(\omega;H)/T(\omega;0)$ for three values of the applied field H in the weakly-coupled-grain (WCG) model. The absorptivities are calculated assuming the sample is much thicker than the penetration depth. The transmissivities are calculated for a thin film on a dielectric substrate, as discussed in the text. The zero field parameters $\lambda_{eff} = 204$ nm, $\lambda_j = 148$ nm and $\rho_j = 93\ \mu\Omega$-cm for sample A listed in Table 3.1 are used in the WCG model.

determine the optical response of the granular film to an applied field. In Fig. 6.2 (a) we plot the calculated absorptivity ratio A(H)/A(0) and in Fig. 6.2 (b) the transmissivity ratio T(H)/T(0) for three values of the field. The results in Table

3.1 for sample A specify the zero field parameters of the WCG model. As expected, below ω_{cutoff} the absorptivity increases with increasing H. Above ω_{cutoff} the loss is already dominated by the resistive behavior of the junction. From the transmission ratio we see that the penetration depth λ_1 increases as H increases, reflecting the increasing inductive response of the junction which occurs as L_j increases.

An inconsistency in our treatment is that because $\lambda_{eff} >> a$, the RSJ junctions are inductively coupled,[139] which we have neglected in this treatment.

It is easy to show that in the WCG model, the oscillator strength from the delta function at $\omega = 0$ is simply $\mathcal{A}_s = (\pi/2)(\mathcal{L}_g + \mathcal{L}_j)^{-1}$, and the oscillator strength from the remaining carriers can be expressed as $\mathcal{A}_n = (\pi/2)\,(\mathcal{L}_j/\mathcal{L}_g)\,(\mathcal{L}_g + \mathcal{L}_j)^{-1}$. In the WCG model $\mathcal{L}_j$ increases as the field H increases, so $\mathcal{A}_s$ decreases and $\mathcal{A}_n$ increases as H increases. This corresponds to a shift of oscillator strength from the superconducting condensate to the normal fluid as H increases. The total oscillator strength $\mathcal{A} = \mathcal{A}_s + \mathcal{A}_n$ is, however, conserved.

6.2.3. Karrai Model

Another interesting phenomenological model is due to Karrai *et al.* [28] using the results of Caroli *et al.* .[140] Caroli *et al.* used the Bogoliubov equations[36] to solve for the quasi-particle excitations in a strongly type-II superconductor. They showed that for $\kappa >> 1$ an Abrikosov vortex line can be treated as a normal core with radius ξ_0, the coherence length. The normal core has a discrete quasiparticle excitation spectrum with energy spacing $\Omega_0 = \hbar/m\xi_0^2$. This can be understood from the uncertainty principle for an electron of mass m constrained to lie within a core of radius ξ_0: $\hbar\Omega_0 = \hbar^2\Delta p^2/m\xi_0^2 = \hbar^2/m\xi_0^2$ where $\Delta p\Delta x = \Delta p\xi_0 = \hbar$. The discrete quasiparticle states of the vortex can be thought of as superpositions of electron and hole states trapped in the vortex by continual

Andreev reflection due to the spatially varying order parameter, which defines the vortex.

For a conventional superconductor $\xi_0 \sim 100$ nm and the energy spacing is too small to be measured by conventional techniques. However, for high-T_c superconductors, $\xi_0 \sim 2$ nm and using $m \sim m_e$ we find $\Omega_0 \sim 150\ cm^{-1} = 19$ meV. Several methods have been proposed for observing this discrete structure within vortex cores through ultrasonic and nuclear magnetic relaxation.[141] However none of these methods has succeeded so far.

In the mixed state, we can think of 'normal' vortex cores immersed in a superconducting medium. We can treat this inhomogeneous system with an effective medium conductivity, since for wavelengths >> ξ, the medium appears homogeneous. Karrai *et al.* characterize the mixed state superconductor as a rigid lattice of cylindrical vortices where each vortex can be thought of as a two-level system with characteristic energy $\hbar\Omega_0$. The dielectric function within the vortex can be described by a lifetime-broadened Lorentzian as

$$\varepsilon_v(\omega) = 1 + \frac{\omega_p^2}{\Omega_0^2 - \omega^2 - i\,\frac{\omega}{\tau_q}} \quad , \tag{6.9}$$

where ω_p is the plasma frequency, and τ_q is the lifetime associated with the vortex quasiparticle excited state. (Actually, Karrai *et al.* use $\omega(\Omega_0 - \omega)$ in place of $\Omega_0^2 - \omega^2$ in Eq. 6.9, for reasons which are not clear to me.) Accounting for the depolarization field of the cylindrical vortex[59] immersed in the superconducting medium with conductivity $\sigma_s(\omega)$, or equivalently, dielectric function $\varepsilon_s(\omega)$, the effective conductivity of the vortex becomes

$$\sigma_{v,eff}(\omega) = \frac{2\sigma_v(\omega)}{1 + \frac{\varepsilon_v(\omega)}{\varepsilon_s(\omega)}} \quad . \qquad (6.10)$$

The total effective conductivity of the medium is then $\sigma_{eff}(\omega) = (1 - \phi)\sigma_s(\omega) + \phi\sigma_{v,eff}(\omega)$ where $\phi \sim H/H_{c2}$ is equivalent to the areal fraction of the superconductor penetrated by the vortices.

In the model of Karrai *et al.*[28], $\sigma_s(\omega) = i\, c^2/4\pi\lambda^2\omega$, corresponding to the purely inductive supercurrent response. In Chapter 3 we showed that at 2 K the volume fraction of normal carriers n_n can be as large as 50% in high quality $YBa_2Cu_3O_7$ thin films. Because n_n is so large it seems reasonable to include some normal carrier concentration in the otherwise purely inductive $\sigma_s(\omega)$, in the form of $\sigma_{Drude}(\omega) = \sigma_0/(1 - i\,\omega\tau)$, as discussed below. (I have also tried reproducing the *calculations* of Karrai *et al.*[28] which they used to model their transmissivity measurements. I have been unable to duplicate their results using the equations given in their paper unless I include some normal carrier concentration using values for σ_0 and τ such as found in Table 3.1. The inclusion of any such normal carrier concentration into their calculations is not discussed in Karrai *et al.*[28].)

There is one argument for not including some normal carrier concentration when calculating transmissivities. From Eq. 6.1 one can see that if $\sigma(\omega)$ is highly inductive, i.e., if $\sigma_2 >> \sigma_1$, then $T(\omega)$ will be dominated by σ_2. However, for the films we studied in chapter 3, the crossover frequency above which $\sigma_1 > \sigma_2$ typically occurs around 100 cm^{-1}, so that any complete description even of the transmissivity of thin films above this frequency must for completeness include the effects of normal carriers, if the results of chapter 3 are to be believed.

Of course, one must include the normal carrier contribution when describing the absorptivity. Without any such normal carrier concentration $\sigma(\omega)$ is completely imaginary and $A(\omega)$ is identically zero.

So in order to be consistent with the results of Chapter 3, we modify the conductivity of Karrai *et al.* to include the contribution of normal carriers so that

$$\sigma'_{eff}(\omega) = (1 - \phi)\sigma_s(\omega) + \phi\, \sigma_{v,eff}(\omega) + \sigma_{Drude}(\omega). \qquad (6.11)$$

Again, as ϕ increases, oscillator strength $\mathcal{A}_s$ decreases and $\mathcal{A}_n$ increases, corresponding to a shift of oscillator strength from the superconducting condensate to the normal fluid. Because $\lambda = c/\omega_p$, it is easy to show that changing ϕ simply shifts oscillator strength between $\sigma_s(\omega)$ and $\sigma_{v,eff}(\omega)$ in such a way that total oscillator strength is conserved, independent of field.

In Fig. 6.3 (a) we have plotted the calculated absorptivity ratio $A(\omega;H)/A(\omega; 0)$ and in Fig. 6.3 (b) the transmissivity ratio $T(\omega;H)/T(\omega; 0)$ for three values of the field, using H_{c2} = 100 T. The absorptivities are calculated assuming the sample is much thicker than the penetration depth. The transmissivities are calculated for a thin film on a dielectric substrate. The parameters λ = 200 nm, Ω_0= 80 cm^{-1}, $1/2\pi c\tau_{iv}$ = 50 cm^{-1} and values for Drude components σ_0 and τ found in Table 3.1 for Sample A. A resonance is clearly seen in both the absorptivity and transmissivity ratios near 80 cm^{-1}. The width of the resonance is relatively insensitive to $1/\tau_{iv}$ due to the presence of the normal carriers manifested by $\sigma_{Drude}(\omega)$, which dominate the loss.

Both the WCG model and the Karrai model predict an increased absorptivity at low frequencies; the Karrai model predicts more of a resonance while the WCG model predicts a monotonic, featureless increase.

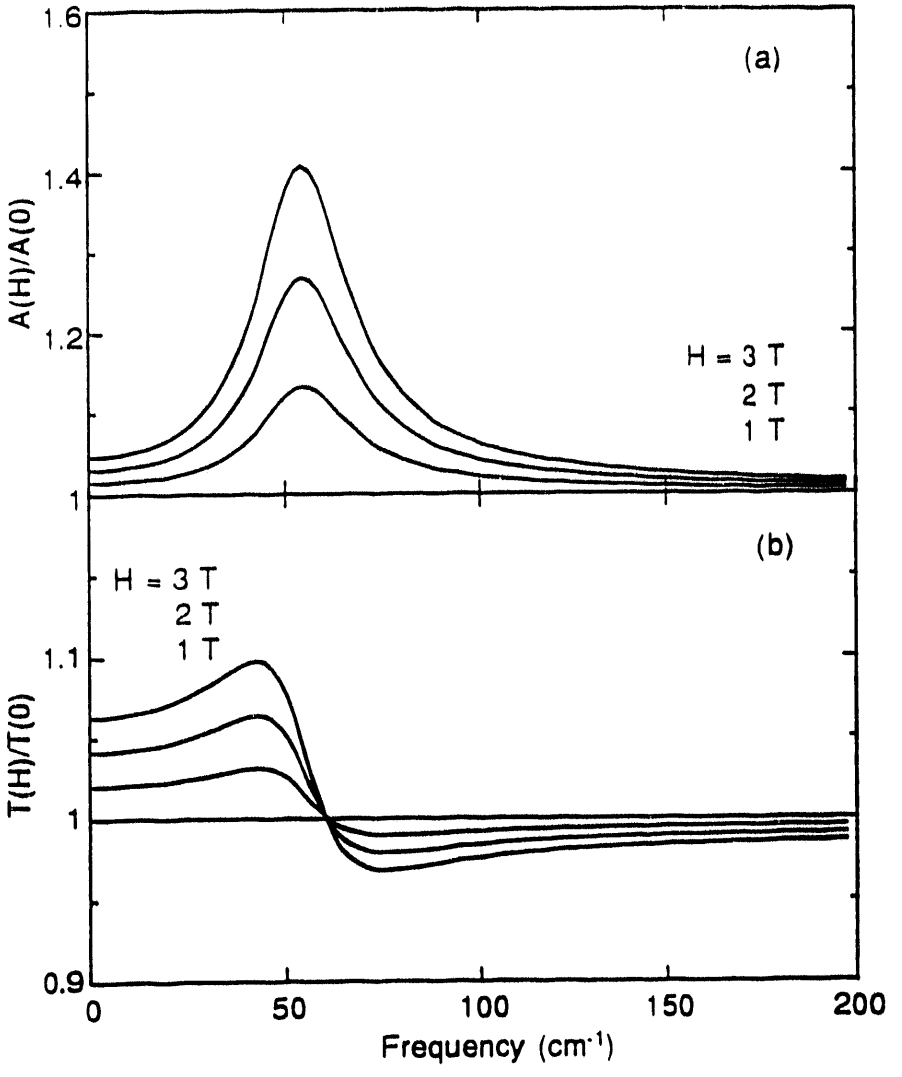

Fig. 6.3 - (a) The absorptivity ratio $A(\omega;H)/A(\omega;0)$ and (b) the transmissivity ratio $T(\omega;H)/T(\omega;0)$ for three values of the applied field H in the Karrai model using Eq. 6.11. The absorptivities are calculated assuming the sample is much thicker than the penetration depth. The transmissivities are calculated for a thin film on a dielectric substrate, as discussed in the text. In the calculations we use H_{c2} = 100 T, λ = 200 nm, Ω_0= 80 cm^{-1} , $1/2\pi c\tau_{iv}$ = 50 cm^{-1} and values for the Drude components σ_0 = 3000 $(\Omega\text{-cm})^{-1}$ and $1/2\pi c\tau$ = 377 cm^{-1}.

6.2.4. Hsu Model

In the Karrai model the mixed state is assumed to consist of a rigid lattice of vortices. In conventional superconductors vortices are strongly pinned at low

frequencies but undergo a crossover to unpinned behavior at some characteristic frequency $1/\tau_v = \kappa/\eta$: The pinning force per unit length is $-\kappa\delta x$ and the viscous drag force per unit length is $\eta\, v = \eta\omega\delta x$ and these two forces are equal when $\omega_{crossover} = 1/\tau_v$. In conventional superconductors this crossover has been observed near 10 MHz[142] so that at and above microwave frequencies the vortices are essentially unpinned. Any complete microscopic understanding of vortex dynamics must take into account both the discrete spectrum of states within the vortex cores as well as the motion of the vortices.

Hsu [29,30] has developed a novel, microscopic description of single vortex dynamics based on the Bogoliubov-deGennes equations for s-wave superconductors, valid for short range, instantaneous pairing interaction, with $k_F\xi >> 1$. This latter condition is barely satisfied for the high-T_c superconductors. In addition, high-T_c superconductors may have d-wave symmetry of the order parameter, for which the microscopic structure of vortices has not yet been calculated. Despite these caveats it is interesting to explore this model.

The Hsu model is applicable to the low temperature, clean, extreme Type II limit and for fields $H_{c1} << H << H_{c2}$. In this approach the excited state of the vortex cores are expressed in terms of vortex motion, which are then treated in the same manner as the usual motion of the supercurrent and pinned vortices. The vortex can be thought of as a self -consistent potential: The motion of the vortex creates quasiparticle excitations which need to be treated self-consistently with the state of the excited vortex core.

In what follows I will outline the main results of this model. We start here with the equation of motion for the vortex, which includes the intra-vortex excitations expressed in the rest frame, along with the background vortex and superfluid motion, and can be written as

$$\dot{v}_L = \dot{v}_S + \overline{\Omega}_0(v_L - v_S)x\hat{z} - \frac{1}{\tau_q}v_L - \alpha^2 r \qquad (6.12)$$

where v_L is the vortex velocity and v_S is the background superfluid velocity. The magnetic field is along the z direction. $\overline{\Omega}_0 = (1-\phi)\Omega_0$ with $\Omega_0 = \hbar/m\xi_0^2$. The quantity ϕ is roughly H/H_{c2}. Note that the vortex acceleration is not perpendicular to the vortex motion, which is the usual case for simple vortex dynamics. The coefficient of the drag term is a Drude-like scattering rate $1/\tau_q$ related to the lifetime of low energy quasiparticle states. The force due to the drag term in Eq. 6.12 can be written $f_d = m_v a = -\eta\, v_L$ where m_v is the vortex mass per unit length so that we can identify $1/\tau_q = \eta/m_v$ in Eq. 6.12. The last term in Eq. 6.12 is due to the pinning force $f_p = m_v a = -\kappa x$ so that $\alpha^2 = \kappa/m_v$.

The discrete vortex excitation energy $\Omega_0 = \hbar/m\xi_0^2$ can be expressed in several ways. Ignoring factors of order π we can write $\Omega_0 = \Delta^2/\hbar E_F$ where $\Delta = 2\hbar v_F/\pi\xi_0$. We can also write $\Omega_0 = eH_{c2}/m_e c$, where $H_{c2} \sim \Phi_0/\pi\xi_0^2$. Hsu defines $\Omega_0 \equiv \omega_c/\phi$, where $\omega_c = eH/mc$ is the cyclotron frequency. Still another way of representing the vortex excitation energy Ω_0 is in terms of the vortex mass m_v. The vortex mass per unit length can be thought of as the product of the bare carrier mass, the two dimensional density of carriers n_{2d}, and the area of the vortex so that $m_v = mn_{2d}\xi_0^2 = n_{2d}\hbar/\Omega_0$.

The conductivity is calculated by expressing the total current J and electric field E as a function of v_L and v_S, using the equation of motion to eliminate v_L, and then finding the tensor connecting J and E. The results can be compactly expressed in terms of the functions P and Q defined by

$$P = -\omega^2 \frac{\overline{\Omega}_0^2 - \omega^2 - i\,\omega/\tau_q + \alpha^2}{(-\omega^2 - i\,\omega/\tau_q + \alpha^2)^2 - \omega^2\overline{\Omega}_0^2}\,, \qquad (6.13)$$

$$Q = i\,\omega\bar{\Omega}_0 \frac{-i\,\omega/\tau_q + \alpha^2}{(-\omega^2 - i\,\omega/\tau_q + \alpha^2)^2 - \omega^2\bar{\Omega}_0^2} \,. \tag{6.14}$$

The system can most conveniently be characterized in terms of its response to circularly polarized light. The conductivity for incident radiation of positive and negative helicity can be written as

$$\sigma^{\pm}(\omega) = \frac{n_s e^2}{m} \frac{1 - \phi + \phi(P \pm i\,Q)}{-i\,\omega + \omega_c(-Q \pm i\,P)} \,. \tag{6.15}$$

The magneto-optical activity predicted by Eq. 6.15 is a consequence of the presence of the magnetic field, which breaks time reversal symmetry. Because the incident radiation is unpolarized in the experiment we have performed we are most interested in the response of the medium to unpolarized light, which can be described by $\sigma^{xx}(\omega) = (1/2)\,(\sigma^{+}(\omega) + \sigma^{-}(\omega))$. Resonances present either in $\sigma^{+}(\omega)$ or in $\sigma^{-}(\omega)$ will appear in $\sigma^{xx}(\omega)$ and can be distinguished from each other, provided they do not overlap in frequency or are too strongly damped.

It is instructive to look at the limiting behavior of Eq. 6.15 for several cases.

(a) When $H = 0$, $\phi = 0$, and the optical activity is destroyed, i.e., $\sigma^{+}(\omega) = \sigma^{-}(\omega)$, and $\sigma^{xx}(\omega) = i\,n_s e^2/m\omega$, the London conductivity. This is identical to the TF model conductivity, apart from the $\sigma_{Drude}(\omega)$ term, discussed previously. In Chapter 3 we showed that a significant portion of the charge carriers could be in the normal state even at low temperatures. We therefore express the response of the system to unpolarized radiation, including the normal carriers, as

$$\sigma^{xx}_{eff}(\omega) = \frac{\sigma+(\omega) + \sigma(\omega)}{2} + \sigma_{Drude}(\omega). \tag{6.16}$$

(b) In the limit $\tau_q \rightarrow \infty$, $\sigma^{xx}(\omega) = (\imath\omega n_s e^2/m)/(\omega^2 - \omega_c^2)$, which is the cyclotron resonance of a clean system, in agreement with Eq. 6.6.

(c) When the pinning frequency $\alpha >> \Omega_0, \omega$ and for small fields such that $\phi \rightarrow 0$ Eq. 6.15 becomes

$$\sigma^{\pm}(\omega) = \frac{i\, n_s e^2}{m\omega}\left(1 + \phi\frac{\Omega_0^2}{\alpha^2}\frac{1}{1 - i\,\omega\tau_v}\right)^{-1}. \qquad (6.17)$$

The scattering rate $1/\tau_v = \kappa/\eta$ so that $\alpha^2 = (1/\tau_v)(1/\tau_q)$. Ignoring any normal carrier contributions, Eq. 6.17 is identical to the low temperature result of Coffey and Clem[143] for the optical response in the mixed state, provided we make the identification $\phi\,\Omega_0^2/\alpha^2 = \lambda_c^2/\lambda^2$. λ_c is the Campbell penetration depth with $\lambda_c^2 = H\Phi_0/4\pi\kappa$. It can also be shown that $\lambda_c^2/\lambda^2\phi = H_c^2/4\pi\kappa$, and hence $\Omega_0^2/\alpha^2 = H_c^2/4\pi\kappa$.

Note that $\phi\,\Omega_0^2/\alpha^2$ and by extension Eq. 6.17 are independent of the vortex mass m_v. Since $\alpha \propto m_v^{-1/2}$, this implies $\Omega_0 \propto m_v^{-1/2}$. We expect this to be the case since Eq. 6.17 is applicable for frequencies well below the vortex resonance frequency $\alpha = (\kappa/m_v)^{1/2}$. Below (above) $\omega_{crossover} = 1/\tau_v = \kappa/\eta$ the vortex is strongly (weakly) pinned, where $\omega_{crossover} << \alpha$.

We can see an interesting relationship between Ω_0 and α in the following way.[144] The Free energy per unit length of the pinned vortex is $H_c^2\xi_0^2/8\pi$. If we imagine that the vortex is at a minimum in the pinning potential well defined by the force constant κ, then $\kappa\xi_0^2/2 = H_c^2\xi_0^2/8\pi$. This implies $H_c^2/4\pi\kappa = 1$, or, since $\Omega_0^2/\alpha^2 = H_c^2/4\pi\kappa$, $\Omega_0 = \alpha$. If the vortices are less strongly pinned then $H_c^2/4\pi\kappa > 1$ and $\Omega_0 < \alpha$.

In Fig. 6.4 (a) we have plotted the calculated absorptivity ratio $A(\omega;H)/A(\omega;0)$ and in Fig. 6.4 (b) the transmissivity ratio $T(\omega;H)/T(\omega;0)$ for three values of the field, using $H_{c2} = 100$ T. We use Eq. 6.16 to describe the

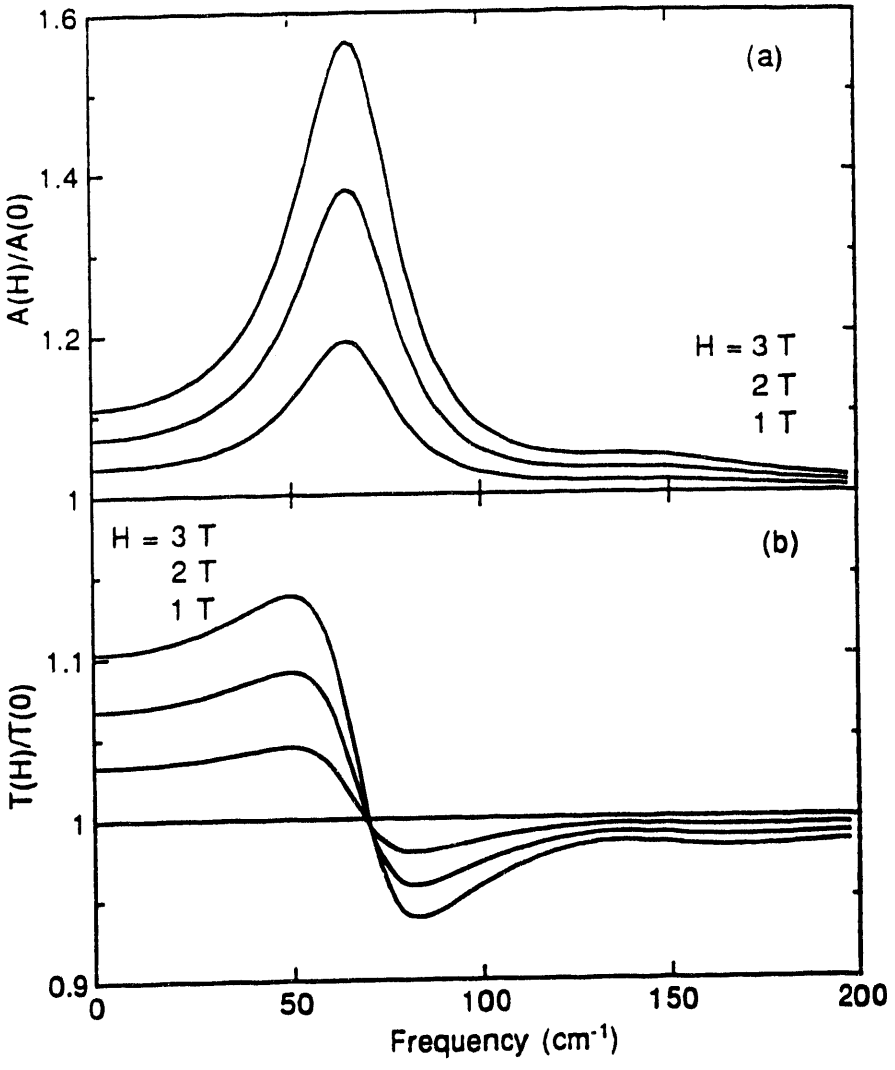

Fig. 6.4 - (a) The absorptivity ratio $A(\omega;H)/A(\omega;0)$ and (b) the transmissivity ratio $T(\omega;H)/T(\omega;0)$ for three values of the applied field H in the Hsu model using Eq. 6.16. The absorptivities are calculated assuming the sample is much thicker than the penetration depth. The transmissivities are calculated for a thin film on a dielectric substrate, as discussed in the text. In the calculations we use $H_{c2} = 100$ T, $\lambda = 200$ nm, $\alpha = 100$ cm $^{-1}$, $\Omega_0 = 80$ cm^{-1} , $1/2\pi c\tau_q = 50$ cm^{-1} and values for Drude components $\sigma_0 = 3000$ $(\Omega\text{-cm})^{-1}$ and $1/2\pi c\tau = 377$ cm^{-1}. A resonance is clearly seen in both the absorptivity and transmissivity ratios near 60 cm^{-1} , and a smaller feature is seen near 140 cm^{-1}.

effective response of the medium to unpolarized radiation. The absorptivities are calculated assuming the sample is much thicker than the penetration depth. The transmissivities are calculated for a thin film on a dielectric substrate. The parameters are λ_0 = 200 nm, α = 100 cm $^{-1}$, Ω_0= 80 cm^{-1} , $1/2\pi c\tau_q$ = 50 cm^{-1} and values for Drude components σ_0 and τ found in Table 3.1 for Sample A. As with the WCG and Karrai model, the strength of the resonances in A(H)/A(0) and in T(H)/T(0) depend on ϕ. The plots shown in Fig. 6.4 are qualitatively similar to the results of the Karrai model calculations shown in Fig. 6.3. A resonance is clearly seen in both the absorptivity and transmissivity ratios near 60 cm^{-1} , and a smaller feature is seen near 140 cm^{-1}.

By making the quasiparticle scattering rate $1/\tau_q$ very short, we have also been able to clearly resolve how values of α and Ω_0 affect the various contributions to the resonances. We observe two resonances in $\sigma^{xx}(\omega)$, at $\omega = \alpha \pm \Omega_0$, corresponding to a resonance in $\sigma^+(\omega)$ and in $\sigma^-(\omega)$. The amplitude of the resonances decrease as α increases. In Fig. 6.5 we plot $\sigma^+(\omega)$, $\sigma^-(\omega)$ and $\sigma_{Drude}(\omega)$ for comparison using the same previous values but with $1/2\pi c\tau_q$ = 10 cm^{-1}. We can clearly see the resonances at $\omega = \alpha \pm \Omega_0/2$. In Fig. 6.4 the resonance at $\omega = \alpha + \Omega_0/2$ is dominated by $\sigma_{Drude}(\omega)$. In the limit where the quasiparticle scattering rate $1/\tau_q$ becomes equal to or longer than Ω_0, the resonances in $\sigma^+(\omega)$ and in $\sigma^-(\omega)$ cannot be distinguished. In this limit, there should be very little magneto-optic activity.

By numerical integration we find oscillator strength is conserved in the Hsu model as a function of ϕ. As ϕ increases, oscillator strength $\mathcal{A}_s$ decreases and $\mathcal{A}_n$ increases, corresponding to a shift of oscillator strength from the superconducting condensate to the normal fluid.

A significant conclusion of the Hsu model is that in the absence of pinning and damping (e.g., α = 0 and $1/\tau_q$ = 0) there is no dissipation. An applied field,

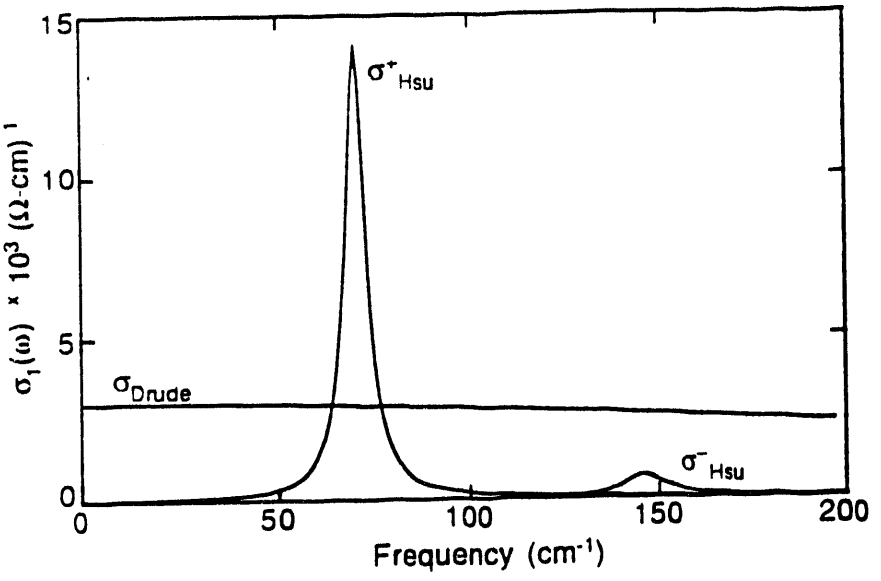

Fig. 6.5 - The quantities $\sigma^+(\omega)$ and $\sigma^-(\omega)$ from the Hsu model, Eq. 6.15, with $\phi = 0.03$, $\lambda = 200$ nm, $\alpha = 100$ cm $^{-1}$, $\Omega_0 = 80$ cm^{-1} and $1/2\pi c\tau_q = 10$ cm^{-1}. Also shown for comparison is $\sigma_{Drude}(\omega)$ using $\sigma_0 = 3000$ $(\Omega\text{-cm})^{-1}$ and $1/2\pi c\tau = 377$ cm^{-1}.

instead of causing a dipole transition within the vortex, causes the vortex to move instead. The vortex does not stand still to allow a dipole transition to occur, as would the core of an atom. Only when the translational invariance of the system is broken does dissipation appear near Ω_0.

Recently, magneto-optical activity has been observed in the far-infrared in transmission measurements through thin superconducting $YBa_2Cu_3O_7$ films.[28] Although working at frequencies much higher than the cyclotron resonance ω_c, these workers claim that the observed magneto-optic activity is due to the high frequency tail of the cyclotron resonance. This work is an apparent demonstration of the validity of the Kohn theorem to an electron system in the superconducting state.[28]

6.3. Magnetic Field Experiment

We have directly measured the absorptivities of $YBa_2Cu_3O_7$ films at 2 K in magnetic fields up to 3 Tesla. We use a bolometric technique where the thin film acts as the absorber in a composite bolometric detector. In these measurements the film is located at the center of a superconducting solenoid.

6.3.1. Description of Experiment

A schematic diagram of the apparatus is shown in Fig. 6.6. Incident radiation A from a Fourier transform spectrometer passes through a cold low pass filter (not shown) and through the polypropylene window B. The throughput limiter C defines the radiation incident on the superconducting film, D. An infrared absorber surrounding the opening,[58] I, reduces stray radiation. A small thermistor, E, is glued to the back of the substrate to measure the absorbed radiation. The superconducting film is located at the center of the superconducting solenoid, F, which is inside the evacuated bolometer can, G. The vacuum can is immersed in pumped LHe. The superconducting substrate is spring loaded against the throughput limiter by means of a thin walled fiberglass tube, H. The thermal conductance of the fiberglass tubing is small enough that the electrical leads to the thermistor (not shown) dominate the thermal conductance of the bolometer. The throughput limiter, substrate and fiberglass tube are all attached to a cut away brass tube assembly which slides into a 7/16" bore. The solenoid has a 1/2" ID bore.

The absorptivity is measured with and without magnetic field H and the ratio $A(\omega;H)/A(\omega;0)$ is calculated from the ratio of the respective spectra. The output spectrum $F(\omega;H) = L(\omega)A(\omega;H)\,S(f)$ where ω is the frequency of light, $L(\omega)$ is the submillimeter spectrum incident on the absorbing film from the spectrometer, $A(\omega;H)$ is the absorptivity of the film, and $S(f)$ is the responsivity of the detector to absorbed power. The responsivity of the bolometric detector is

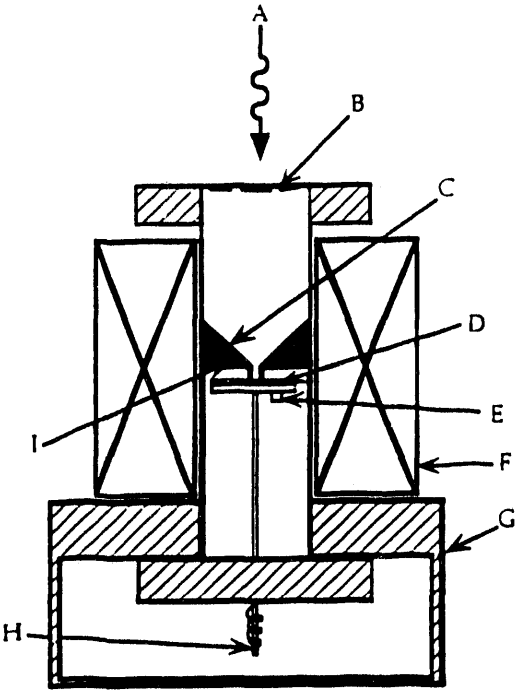

Fig. 6.6 - A schematic diagram of the apparatus used in this experiment. Incident radiation A from a Fourier transform spectrometer passes through a cold low pass filter (not shown) and through the polypropylene window B. The throughput limiter C defines the radiation incident on the superconducting film, D. An infrared absorber surrounding the opening,[58] I, reduces stray radiation. A small thermistor, E, is glued to the back of the substrate to measure the absorbed radiation. The superconducting film is located at the center of the superconducting solenoid, F, which is inside the evacuated bolometer can, G. The vacuum can is immersed in pumped LHe. The superconducting substrate is spring loaded against the throughput limiter by means of a thin walled fiberglass tube, H. The throughput limiter, substrate and fiberglass tube are all attached to a cut away brass tube assembly which slides into a 7/16" bore. The solenoid has a 1/2" ID bore.

measured from the dc-IV characteristics of the thermistor,[45] which is measured at each value of field. We do not find any explicit field dependence on $S(f)$. Because only the field is varied, many systematic errors, such as sample placement, are

avoided, and the normalization procedure is appreciably more simple than when a separate reference detector is used, as discussed in Chapter 2.

We use a General Electric Model 103-2883 superconducting magnet with a persistent current switch rated at 3 Tesla / 13.5 Amperes. The magnet was calibrated with a Hall probe located at the position where the film normally sits, and is monitored during each run with a Hall probe located off axis. Supercurrents generated in the leads of the magnet persist even when the external current is nulled. This is a problem associated with older superconducting magnets, which is avoided in newer models by using higher gauge windings with better electrical isolation between the windings. We can null the field by reversing the current through the magnet, however the Hall probe that is used to monitor the field is located off axis and does not give the precise value of the field at the location of the high-T_c film. For this reason we are only able to measure $A(\omega;H)$ monotonically in H starting with H = 0 T.

6.3.2. Samples Used

We have studied four $YBa_2Cu_3O_7$ (YBCO) samples, listed in Table 6.1. Sample A was grown at Stanford using an off-axis sputtering technique on an MgO substrate.[87] This is the same sample A listed in Table 3.1 and was previously described in Chapter 3. Samples B, C and D were grown at Hewlett-Packard using an off-axis-sputtering technique on Al_2O_3 substrates with a CeO_2 buffer layer.[145]

Good epitaxy between film and substrate is necessary for the growth of high quality, e.g., low loss, YBCO films. Technological applications in the microwave require low loss substrates, and substrates which provide good epitaxy often have unacceptable microwave losses. A practical solution is to use a low loss substrate, such as Al_2O_3, on which a diffusion barrier, or buffer layer,

Sample	Institution	thickness (nm)	Substrate	Tc/δT (K)	R_S (μΩ)	ρ_n(300 K) (μΩ-cm)
A	Stanford	500	MgO	85 / 1.0	12	195
B	Hewlett-Packard	300	CeO_2/Al_2O_3	85 / 0.6	35	345
C	Hewlett-Packard	300	CeO_2/Al_2O_3	85 / 0.6	35	345
D	Hewlett-Packard	300	CeO_2/Al_2O_3	86 / 0.5	40	340

Table 6.1 - YBCO samples measured in this work. Values of microwave surface resistance R_s measured at 4K near 10 GHz are scaled to 10 GHz using an ω^2 law, where ω is the microwave frequency. Superconducting transition temperatures are measured from midpoint of transition; transition widths are measured from 10 - 90 % of transition. Values for the dc resistivity ρ_n measured at 300 K are listed for comparison. Sample A in this table is the identical film to sample A in Table 3.1. Samples B and C were taken from the same 1×1 cm^2 substrate and sample D was grown under nominally identical conditions as samples B and C. The CeO_2 buffer layer used in films B, C and D is approximately 10 nm thick.

has been deposited. A CeO_2 buffer layer on an r-plane Al_2O_3 has been shown to provide excellent in plane epitaxy. The Al_2O_3 is coated with a 10 nm thick layer of CeO_2. The CeO_2 layer is deposited by a single source metalorganic chemical vapor deposition (MOCVD) process.[92] The thin films of YBCO are subsequently deposited by an off-axis, rf-magnetron sputtering from a single stoichiometric target onto targets held at elevated temperatures during the deposition process.[92]

Samples B and C were taken from the same 1×1 cm^2 substrate and sample D was grown under nominally identical conditions as samples B and C. The microwave surface resistance R_s was measured for the samples at 4K near 10 GHz. The values for R_s listed in Table 6.1 are scaled to 10 GHz using an ω^2 law,

where ω is the microwave frequency. Values for the dc resistivity ρ_n measured at 300 K are also listed in Table 6.1 for comparison.

6.3.3. Results

The absorptivity ratios $A(\omega;3\ T)/A(\omega;0)$ for the $YBa_2Cu_3O_7$ samples A - D are plotted in Fig. 6.7 (a) - (d), respectively, as the jagged lines. The smooth lines are best fits which will be described below. The data are taken between ~ 30 cm^{-1} and 200 cm^{-1} at a temperature of 2 K. Because of the limited sensitivity of this experiment we have only plotted results corresponding to the maximum field that our magnet is capable of generating. In this way the magnitude of the measured absorptivity ratio is maximized. When we have examined the field dependence of the absorptivity ratio we find that the amplitude of the features scale proportionately with field H.

For all films the absorptivity ratio $A(\omega;3\ T)/A(\omega;0)$ increases with increasing frequency at low frequencies, rising to a maximum near 60 cm^{-1}, then decreases monotonically. For samples A, B and C the absorptivity ratio approaches the asymptotic limit of unity at high frequencies. The absorptivity ratio for sample D drops below unity at high frequencies. The amplitude, width and precise frequency of the maximum near 60 cm^{-1} varies considerably from sample to sample. Surprisingly, the frequency of the maximum varies most for samples B and C, which are taken from the same 1×1 cm^2 substrate. In addition, the maximum is quite broad for sample D.

Because the maximum in the absorptivity ratio occurs at such a low frequency, especially for samples A, B and D, it is reasonable to ask whether the low frequency feature we observe is a peak, with a well defined low frequency minimum, or simply a shoulder, with the absorptivity ratio rising at low frequencies and remaining constant. In order to explore this we have taken data

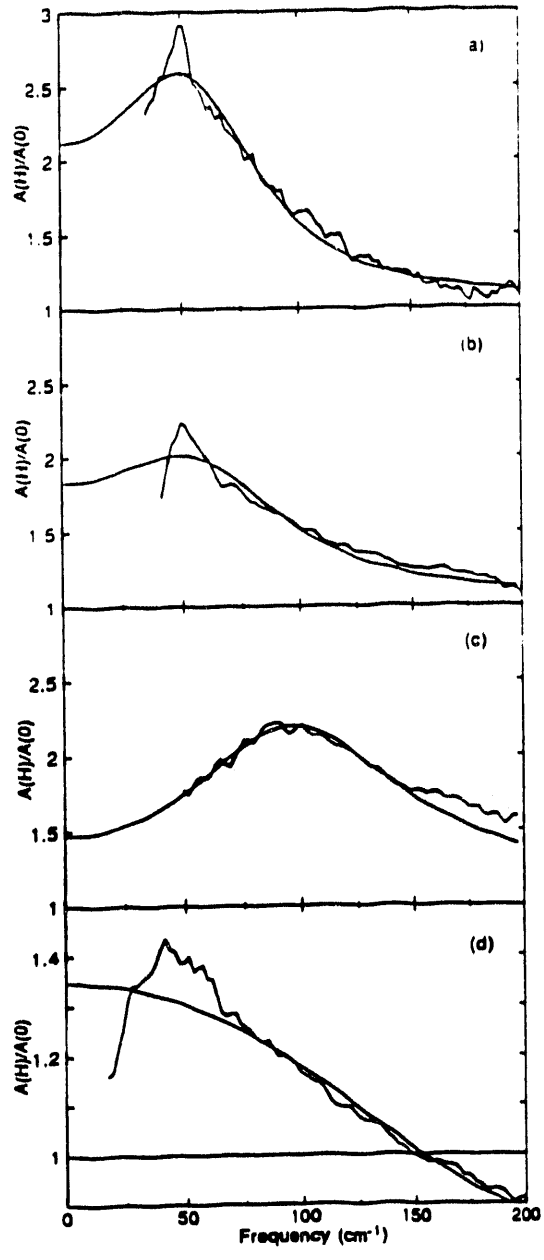

Fig. 6.7 - The directly measured absorptivity ratios $A(\omega;3\ T)/A(\omega;0)$ (jagged lines) for the $YBa_2Cu_3O_7$ samples A - D in cells (a) - (d), respectively. The data are taken at a temperature of 2 K. Also shown are best fits to the absorptivity ratio (smooth lines) using the Hsu model, as described in the text.

to lower frequencies near 15 cm^{-1} for sample D. The results of these measurements are consistent with the results from higher frequencies. However,

this does not rule out systematic errors such as frequency dependent radiation leakage. In Sec. 2.3.2 we discussed the low frequency limit to our measurement. We expect that leakage of radiation around the absorbing sample dominates the measured absorptivity below ~ 30 cm^{-1}. If radiation leakage dominates the absorptivity at low frequencies then the measured absorptivity ratio $A(\omega;H)/A(\omega;0) \rightarrow 1$ as $\omega \rightarrow 0$, which is consistent with our observations. Therefore we cannot rule out the possibility that the decrease in $A(\omega;H)/A(\omega;0)$ as $\omega \rightarrow 0$ is due to frequency dependent leakage. Perhaps the most convincing argument that the low frequency rolloff is real is simply that we also observe a peak in the absorptivity ratio for sample C. For this sample, the frequency of the peak is well above where we suspect frequency dependent leakage effects may dominate the absorptivity.

6.3.4. Analysis

Because it is the more complete of the models presented here, we have used the Hsu model to fit our data. We use the effective conductivity from Eq. 6.16 using values for the Drude components σ_0 and τ found in Table 3.2 for Sample A.

The more degrees of freedom available to fit our data the less meaningful the values of the deduced parameters will be. For this reason we would like to constrain some of the parameters in the model. Initially, we constrained the value of $\phi \sim H/H_{c2} = 0.03$, where we have used the fact that H = 3 T in our measurement and H_{c2} ~ 100 T. The fits obtained in this way are quite poor, and in most cases do not even intersect the data. The best fits have instead been obtained statistically by minimizing χ^2 using the steepest descent method[105] and assuming a normal error distribution. The four parameters Ω_0, α, $1/\tau_q$ and ϕ are allowed to vary. The results of this fitting for samples A - D are shown as the

smooth lines in Fig. 6.7 (a) - (d), respectively. Even by allowing all four parameters to vary the best fit curves are unable to describe the measured low frequency resonance except for sample B, where the resonance is quite broad. However, the fits are able to describe the overall absorptivity levels.

Values of the parameters for these fits are given in Table 6.2. Uncertainties are estimated from the diagonal elements of the covariance matrix,[105] assuming a normal distribution of errors. There are several important features in Table 6.2. From our estimates of the uncertainties, only the fits for samples A and B are statistically meaningful. The minimum in χ^2 is too shallow for samples C and D, as indicated by the large statistical uncertainties for the parameters. In addition, the best fit for sample D is unphysical, as indicated by the negative value for the parameter $1/\tau_q$. We do not understand why the model seems to have the ability to describe our results for samples A and B but not for samples C and D. In what follows we concentrate on the results for the statistically significant fits A and B.

From our discussion of the Hsu model, we expect that $\Omega_0 \leq \alpha$. This is consistent with the results in Table 6.2 within the uncertainties for both samples A and B. We find $\Omega_0 \sim \alpha \sim 170\ cm^{-1}$, in agreement with our initial estimate for $\Omega_0 \sim 150\ cm^{-1}$ from Sec. 6.2.3. Values for $1/\tau_q$, expressed in wavenumbers as $(2\pi c\tau_q)^{-1}$, are comparable to or larger than values for Ω_0. Assuming $H_{c2} \sim 100$ T, values for ϕ should be ~ 0.03, since we used a H = 3 T in our measurement. The results in Table 6.2 for samples A and B are consistent with a slightly smaller H_{c2}. We can also estimate $H_{c2} \sim \Phi_0/\pi\xi_0^2 = 164$ T using $\xi_0 = 2$ nm.

We would like to be able to extract values for the physically meaningful parameters κ, η, and m_v corresponding to the force constant, viscocity and mass of the vortex, respectively. Unfortunately, there are too many unknown quantities for this to be possible. Instead we use values for κ and η which were obtained from time domain terahertz transmission measurements on

Sample	Ω_0 (cm^{-1})	α (cm^{-1})	$(2\pi c\tau_q)^{-1}$ (cm^{-1})	ϕ
A	182 ± 82	127 ± 25	189 ± 62	0.09 ± 0.03
B	218 ± 159	154 ± 51	273 ± 155	0.07 ± 0.04
C	1.1 ± 770	121 ± 9	134 ± 15	0.23 ± 0.02
D	322 ± 543	315 ± 225	- 543 ± 670	0.17 ± 0.05

Table 6.2 - Best fit parameters of the Hsu model used to describe the measured absorptivity ratios for samples A - D, as described in text. The parameters Ω_0, α, $1/\tau_q$ and ϕ correspond to the discrete vortex excitation energy, the vortex resonant frequency, the quasiparticle scattering rate and H/H_{c2}, respectively. Uncertainties are determined from the diagonal elements of the covariance matrix.

$YBa_2Cu_3O_7$ thin films.[144] The films used in this experiment are approximately 300 Å thick and were grown at Hewlett-Packard Laboratories using the same technique as for samples B, C and D studied in this chapter. The results for their measurement is $\kappa = 5 \times 10^6$ gm cm^{-1} s^{-2} and $\eta = 5 \times 10^{-7}$ gm cm^{-1} s^{-1}, or $1/\tau_v = \kappa/\eta = 53$ cm^{-1}. This value for κ is significantly larger than $\kappa = 2 \times 10^5$ gm cm^{-1} s^{-2} used by Coffey *et al.*.[143] We can put an upper limit on the value for κ from the results of Sec. 6.2.4 where we showed $\kappa \leq H_c^2/4\pi$. Using a value for the thermodynamic critical field $H_c \sim \Phi_0/\pi\lambda\xi_0$ with $\lambda = 200$ nm and $\xi_0 = 2$ nm we find that $\kappa \leq 2 \times 10^7$ gm cm^{-1} s^{-2}, consistent with our values for κ.

From the discussion of Sec. 6.2.4 we found $\alpha^2 = (1/\tau_v)(1/\tau_q)$ so from the results of Table 6.2 we find $1/\tau_v = 85$ cm^{-1} and 87 cm^{-1} for samples A and B, respectively, in good agreement with $1/\tau_v$ determined from the terahertz transmission technique.

From the definition of $\alpha = (\kappa/m_v)^{1/2}$ and using $\kappa = 5 \times 10^6$ gm cm^{-1} s^{-2} we find $m_v = 9 \times 10^{-21}$ gm cm^{-1}. Assuming $m \sim m_e$ for the charge carriers and that

there is one plane of carriers every $l \sim 10$ Å then this implies each vortex consists of $n = lm_v/m \sim 1$ bare carrier.

6.4. Conclusions

We have measured the absorptivity ratios $A(\omega;H = 3\ T)/A(\omega;H = 0\ T)$ for four $YBa_2Cu_3O_7$ thin films at 2 K. We observe a resonant absorption in each of the films near 60 cm^{-1}; however, the amplitude, width and precise frequency of this resonance varies greatly from sample to sample. We have attempted to understand these absorptivity ratios by using a model by Hsu *et al.* to fit our data. While the best fits are able to describe the overall magnitude of the absorptivity, they are unable to fit the low frequency resonance for samples A, B and D. For two of the samples (C and D) the best fits are not statistically significant. Values of the parameters obtained from this fit are consistent with recent results from a time domain terahertz transmission measurement on similar samples.[144]

A future goal of this experiment is to measure the transmission of a thin superconducting film in a magnetic field. In a collaborative effort, a time domain terahertz spectroscopic technique will be used to obtain both real and imaginary components of the conductivity for the same sample.[146] The results of the submillimeter and terahertz transmission measurements made on the same sample can then be compared and used to constrain our interpretation of the data.

References

1. J. Bardeen, L.N. Cooper and J.R. Schrieffer, Phys. Rev. **108**, 1175 (1957)
2. P.L. Richards and M. Tinkham, Phys. Rev. **119**, 575 (1960)
3. M.A. Biondi and M.P. Garfunkel, Phys. Rev. Lett. **2**, 143 (1959)
4. R.E. Glover and M. Tinkham, Phys. Rev. **108**, 243 (1957)
5. D.M. Ginsburg and M. Tinkham, Phys. Rev. **118**, 990 (1960)
6. R.R. Joyce, Thesis, University of California at Berkeley (1970)
7. J.B. Bednorz and K.A. Muller, Z. Phys. B **64**, 189 (1986)
8. T. Timusk, M. Reedyk, R. Hughes, D.A. Bonn, J.D. Garrett, J.E. Greedan, C.V. Stager, D.B. Tanner, F. Gao, S.L. Herr, K. Kamaras, G.A. Thomas, S.L. Cooper, J. Orenstein, L.F. Schneemeyer and A.J. Millis, Physica C **162-164**, 841 (1989)
9. D.L. Kaiser, F.W. Gayle, R.S. Roth and L.J. Swartzendruber, J. Mater. Res. **4**, 745 (1989)
10. B. Batlogg, in High Temperature Superconductivity Proceedings, Los Alamos Symposium 1989 , edited by K. S. Bedell, D. Coffey, D. E. Meltzer, D. Pines and J. R. Schrieffer (Addison-Wesley, California, 1990), p. 37
11. T. Timusk and D.B. Tanner, in Physical Properties of High Temperature Superconductors I , edited by D. M. Ginsberg (World Scientific, New Jersey, 1989), p. 339
12. M. Rabinowitz, Lettere al Nuovo Cimento **4**, 549 (1970)
13. T. Yogi and J.E. Mercereau, IEEE Trans. Magn. **17**, 931 (1981)
14. J. Halbritter, IEEE Trans. Magn. **11**, 427 (1975)
15. D. Miller, T.W. Kenny, P.L. Richards, S.R. Spielman and T.H. Geballe, Bull. Am. Phys. Soc. **34**, 792 (1989)

16. T. Pham, H.D. Drew, S.H. Moseley and J.Z. Liu, Phys. Rev. B **41**, 11681 (1990)

17. D. Miller, P.L. Richards, S. Etemad, A. Inam, T. Venkatesan, B. Dutta, X.D. Wu, C.B. Eom, T.H. Geballe, N. Newman and B.F. Cole, Appl. Phys. Lett. **59**, 2326 (1991)

18. D. Miller, P.L. Richards, W.Y. Lee, N. Newman, S.M. Garrison and J.S. Martens, in Proceedings of the conference: Lattice Effects in High-Tc superconductors , edited by Y. Bar-Yam, T. Egami, J. M.-d. Leon and A. R. BIshop (World Scientific, River Edge, NJ, 1992), p. 269

19. D. Miller, P.L. Richards, S.M. Garrison, N. Newman, C.B. Eom, T.H. Geballe, S. Etemad, A. Inam, T. Venkatesan, J.S. Martens, W.Y. Lee and L.C. Bourne, J. Superc. **5**, 379 (1992)

20. D. Miller, P.L. Richards, S. Etemad, A. Inam, T. Venkatesan, B. Dutta, X.D. Wu, C.B. Eom, T.H. Geballe, N. Newman and B.F. Cole, Phys. Rev. B **47**, 8076 (1993)

21. D. Miller and P.L. Richards, Phys. Rev. B **47**, 12308 (1993)

22. M. Hawley, I.D. Raistrick, J.G. Beery and R.J. Houlton, Science **251**, 1587 (1991)

23. C.M. Jackson, J.H. Kobayashi, E.B. Guillory, C. Pettiette-Hall and J.F. Burch, J. Superc. **5**, 417 (1992)

24. E. Belohoubek, E. Denlinger, D. Kalokitis, A. Fathy, R. Paglione, V. Pendrik, J. Brown, A. Pique, X.D. Wu, S.M. Green, S. Mathews, R. Edwards, M. Mathur and T. Venkatesan, J. Superc. **5**, 423 (1992)

25. S. Verghese, P.L. Richards, K. Char, D.K. Fork and T.H. Geballe, J. Appl. Phys. **71**, 2491 (1992)

26. H. Piel and G. Muller, IEEE Trans. Magn. **27**, 854 (1991)

27. K. Karrai, E. Choi, F. Dunmore, S. Liu, X. Ying, Q. Li, T. Venkatesan, H.D. Drew, Q. Li and D.B. Fenner, Phys. Rev. Lett. **69**, 355 (1992)

28. K. Karrai, E.J. Choi, F. Dunmore, S. Liu, H.D. Drew, Q. Li, D.B. Fenner, Y.D. Zhu and F.C. Zhang, Phys. Rev. Lett. **69**, 152 (1992)

29. T.C. Hsu, Phys. Rev. B **46**, 3680 (1992)

30. T.C. Hsu, (preprint)

31. M. Tinkham, in Far Infrared Properties of Solids , edited by S. S. Mitra and S. Nudelman (Plenum, New York, NY, 1970), p.

32. G.E.H. Reuter and E.H. Sondheimer, Proc. Roy. Soc. (London) **A195**, 336 (1948)

33. T. Holstein, Phys. Rev. **96**, 535 (1954)

34. R.R. Joyce and P.L. Richards, Phys. Rev. Lett. **24**, 1007 (1970)

35. M. Tinkham and R.A. Ferrell, Phys. Rev. Lett. **2**, 331 (1959)

36. M. Tinkham, Introduction to Superconductivity , (McGraw-Hill, New York, 1975)

37. F. Wooten, Optical Properties of Solids , (Academic, San Diego, CA, 1972)

38. M. Cardona and D.L. Greenaway, Phys. Rev. **133A**, 1685 (1964)

39. I. Bozovic, J.H. Kim, J.S.H. Jr., E.S. Hellman, E.H. Hartford and P.K. Chan, Phys. Rev. B **46**, 1182 (1992)

40. N.E. Bickers, D.J. Scalapino, R.T. Collins and Z. Schlesinger, Phys. Rev. B **42**, 67 (1990)

41. W.L. McMillan and J.M. Rowell, in Superconductivity , edited by R. D. Parks (Marcel Dekker, New York, NY, 1969), p. 561

42. D.J. Scalapino, in Superconductivity , edited by R. D. Parks (Marcel Dekker, New York, NY, 1969), p. 449

43. N.S. Nishioka, P.L. Richards and D.P. Woody, Appl. Optics **17**, 1562 (1978)

44. P.L. Richards, unpublished (1993)

45. R.C. Jones, J. Opt. Soc. Am. **43**, 1 (1953)

46. F. Reif, Fundamentals of Statistical and Thermal Physics , (McGraw-Hill, New York, NY, 1965)

47. E.E. Haller, Infrared Phys. **25**, 257 (1985)

48. NiCr resistors are manufactered by Mini-Systems Inc., North Attleboro, Mass. 02761

49. T.W. Kenny, P.L. Richards, I.S. Park, E.E. Haller and J.W. Beeman, Phys. Rev. B **39**, 8476 (1989)

50. P. Fellgett, J. Physique **19**, 187 (1958)

51. R.J. Bell, Introductory Fourier Transform Spectroscopy , (Academic, New York, NY, 1972)

52. R.B. Sanderson and E.E. Bell, Appl. Optics **12**, 266 (1973)

53. M.L. Forman, W.H. Steel and G.A. Vanasse, J. Opt. Soc. Am. **56**, 59 (1966)

54. H. Sakai, G.A. Vanasse and M.L. Forman, J. Opt. Soc. Am. **58**, 84 (1968)

55. L. Mertz, Infr. Phys. **7**, 17 (1967)

56. E.E. Bell, Infr. Phys. **6**, 57 (1966)

57. Y. Yamada, A. Mitsuishi and H. Yoshinaga, J. Opt. Soc. Am. **52**, 17 (1962)

58. The infrared absorber is made from precast Eccosorb CR110, Emerson and Cuming, Gardena, CA, USA

59. C. Kittel, Introduction to Solid State Physics , (Wiley, New York, 1986)

60. R.G. Chambers and A.B. Pippard, Institute of Metals Monograph **13**, 281 (1953)

61. W. Koster and H.P. Rave, Z. Metallkde. **55**, 750 (1964)

62. M. Halpern, H.P. Gush, E. Wichnow and V. deCosmo, Appl. Optics **25**, 565 (1986)

63. T. Vanduzer and C.W. Turner, Principles of Superconducting Devices and Circuits , (Elsevier, New York, NY, 1981)

64. J.P. Carbotte, Rev. Mod. Phys. **62**, 1027 (1990)

65. G.B. Arnold, J. Zasadzinski, J.W. Osmun and E.L. Wolf, Journal of Low Temperature Physics **40**, 225 (1980)

66. L. Ghivelder and W.A. Phillips, Phys. Rev. B **41**, 4056 (1990)

67. W.L. McMillan and J.M. Rowell, Phys. Rev. Lett. **14**, 108 (1965)

68. O.V. Lounasma, Experimental Principles and Methods below 1K , (Academic Press, New York, NY, 1974)

69. CRC Handbook of Chemistry and Physics, 72nd Edition, edited by D.R. Lide (CRC Press, Boston, MA, 1991)

70. Thermophysical Properties of Matter, edited by Y.S. Touloukian (Plenum, New York, NY, 1970)

71. Z. Schlesinger, R.T. Collins, D.L. Kaiser and F. Holtzberg, Phys. Rev. Lett. **59**, 1958 (1987)

72. K. Kamaras, L.L. Herr, C.D. Porter, N. Tache, D.B. Tanner, S. Etemad, T. Venkatesan, E. Chase, A. Inam, X.D. Wu, M.S. Hegde and B. Dutta, Phys. Rev. Lett. **64**, 84 (1990)

73. J. Orenstein, G.A. Thomas, A.J. Millis, S.L. Cooper, D.H. Rapkine, T. Timusk, L.F. Schneemeyer and J.V. Waszczak, Phys. Rev. B **42**, 6342 (1990)

74. Z. Schlesinger, R.T. Collins, F. Holtzberg, C. Field, G. Koren and A. Gupta, Phys. Rev. B **41**, 11237 (1990)

75. D. vanderMarel, M. Bauer, E.H. Brandt, H.U. Habermeier, D. Heitmann, W. Konig and A. Wittlin, Phys. Rev. B **43**, 8606 (1991)

76. K.F. Renk, B. Gorshunov, J. Schutzmann, A. Pruckl, B. Brunner, J. Betz, S. Orbach, N. Klein, G. Muller and H. Piel, Europhys. Lett. **15**, 661 (1991)

77. J. Schutzmann, W. Ose, J. Keller, K.F. Renk, B. Roas, L. Schultz and G. Saemann-Ischenko, Europhys. Lett. **8**, 679 (1989)

78. R.T. Collins, Z. Schlesinger, R.H. Koch, R.B. Laibowitz, T.S. Plaskett, P. Freitas, W.J. Gallagher, R.L. Sandstrom and T.R. Dinger, Phys. Rev. Lett. **59**, 704 (1987)

79. G.A. Thomas, J. Orenstein, D.H. Rapkine, M. Capizzi, A.J. Millis, R.N. Bhatt, L.F. Schneemeyer and J.V. Waszczak, Phys. Rev. Lett. **61**, 1313 (1988)

80. Z. Schlesinger, R.T. Collins, F. Holtzberg, C. Feild, S.H. Blanton, U. Welp, G.W. Crabtree, Y. Fang and J.Z. Liu, Phys. Rev. Lett. **65**, 801 (1990)

81. T. Pham, M.W. Lee, H.D. Drew, U. Welp and Y. Fang, Phys. Rev. B **44**, 5377 (1991)

82. F. Gao, G.L. Carr, C.D. Porter, D.B. Tanner, S. Etemad, T. Venkatesan, A. Inam, B. Dutta, X.D. Wu, G.P. Williams and C.J. Hirschmugl, Phys. Rev. B **43**, 10383 (1991)

83. G.P. Williams, R.C. Budhani, C.J. Hirschmugl, G.L. Carr, S. Perkowitz, B.Lou and T.R. Yang, Phys. Rev. B **41**, 4752 (1990)

84. T. Timusk, C.D. Porter and D.B. Tanner, Phys. Rev. Lett. **66**, 663 (1991)

85. D.C. Mattis and J. Bardeen, Phys. Rev. **111**, 412 (1958)

86. K.F. Renk, J. Schutzmann, A. Pruckl, B. Roas, L. Schultz and G. Saemann-Ischenko, Physica B **165&166**, 1253 (1990)

87. C.B. Eom, J.Z. Sun, K. Yamamoto, A.F. Marshall, K.E. Luther and T.H. Geballe, Appl. Phys. Lett. **55**, 595 (1989)

88. N. Newman, K. Char, S.M. Garrison, R.W. Barton, R.C. Taber, C.B. Eom, T.H. Geballe and B. Wilkens, Appl. Phys. Lett. **57**, 520 (1990)

89. A. Inam, M.S. Hegde, X.D. Wu, T. Venkatesan, P. England, P.F. Miceli, E.W. Chase, C.C. Chang, J.M. Tarascon and J.B. Wachtman, Appl. Phys. Lett. **53**, 908 (1988)

90. D.M. Hwang, T. Venkatesan, C.C. Chang, L. Nazar, X.D. Wu, A. Inam and M.S. Hegde, Appl. Phys. Lett. **54**, 1702 (1989)

91. A. Inam, X.D. Wu, L. Nazar, M.S. Hegde, C.T. Rogers, T. Venkatesan, R.W. Simon, K. Daly, H. Padamsee, J. Kirchgessner, D. Moffat, D. Rubin, Q.S. Shu, D. Kalokitis, A. Fathy, V. Pendrick, R. Brown, B. Brycki, E. Belohoubek, L. Drabeck, G. Gruner, R. Hammond, F. Gamble, B.M. Lairson and J.C. Bravman, Appl. Phys. Lett. **56**, 1178 (1990)

92. C.B. Eom, J.Z. Sun, B.M. Lairson, S.K. Streiffer, A.F. Marshall, K. Yamamoto, S.M. Anlage, J.C. Bravman, T.H. Geballe, S.S. Laderman, R.C. Taber and R.D. Jacowitz, Physica C **171**, 354 (1990)

93. S.S. Laderman, R.C. Taber, R.D. Jacowitz, J.L. Moll, C.B. Eom, T.L. Hylton, A.F. Marshall, T.H. Geballe and M.R. Beasley, Phys. Rev. B **43**, 2922 (1991)

94. N. Newman, B.F. Cole, S.M. Garrison, K. Char and R.C. Taber, IEEE Trans. Magn. **27**, 1276 (1991)

95. T.S. Ravi, D.M. Hwang, R. Ramesh, S.W. Chan, L. Nazar, C.Y. Chen, A. Inam and T. Venkatesan, Phys. Rev. B **42**, 10141 (1990)

96. J. Sizemore, R. Barton, A. Marshall, J.C. Bravman, M. Naito and K. Char, IEEE Trans. Magn. **25**, 2245 (1989)

97. R.C. Taber, Review of Scientific Instruments **61**, 2200 (1990)

98. H. Padamsee, J. Kirchgessner, D. Moffat, J. Potts, D.L. Rubin, Q.S. Shu, A. Inam, X.D. Wu, L. Nazar, M.S. Hegde and T. Venkatesan, (unpublished)

99. N. Klein, H. Chaloupka, G. Muller, S. Orbach, H. Piel, B. Roas, L. Schulz, U. Klein and M. Peiniger, J. Appl. Phys. **67**, 6940 (1990)

100. R. Feile, Physica C **159**, 1 (1989)

101. T.L. Hylton, A. Kapitulnik, M.R. Beasley, J.P. Carini, L. Drabeck and G. Gruner, Appl. Phys. Lett. **53**, 1343 (1988)

102. T.L. Hylton and M.R. Beasley, Phys. Rev. B **39**, 9042 (1989)

103. R. Gross, P. Chaudhari, M. Kawasaki and A. Gupta, IEEE Trans. Magn. **27**, 3227 (1991)

104. D.R. Harshman, L.F. Schneemeyer, J.V. Waszczak, G. Aeppli, R.J. Cava, B. Batlogg, L.W. Rupp, E.J. Ansaldo and D.L. Williams, Phys. Rev. B **39**, 851 (1989)

105. W.H. Press, B.P. Flannery, S.A. Teukolsky and W.T. Vetterling, Numerical Recipes in C: The Art of Scientific Computing , (Cambridge Press, New York, NY, 1990)

106. A. Schenck, Muon Spin Rotation Spectroscopy: Principles and Applications in Solid State Physics , (Adam Hilger, Accord, MA, 1985)

107. W. Barford and J.M.F. Gunn, Physica C **156**, 515 (1988)

108. E.H. Brandt, Phys. Rev. B **37**, 2349 (1988)

109. G. Aeppli, R.J. Cava, E.J. Ansaldo, J.H. Brewer, S.R. Kreitzman, G.M. Luke, D.R. Noakes and R.F. Kiefl, Phys. Rev. B **35**, 7129 (1987)

110. S.M. Anlage, H. Sze, H.J. Snortland, S. Tahara, B. Langley, C.B. Eom, M.R. Beasley and R. Taber, Appl. Phys. Lett. **54**, 2710 (1989)

111. D.A. Bonn, R. Liang, D.J. Baar, D.C. Morgan, P. Dosanjh, W.N. Hardy, C. Kallin and A.J. Berlinsky, (preprint)

112. D.B. Romero, C.D. Porter, D.B. Tanner, L. FOrro, D. Mandrus, L. Mihaly, G.L. Carr and G.P. Williams, Phys. Rev. Lett. **68**, 1590 (1992)

113. K. Kamaras and S. Etemad, Private Communication

114. S. Tajima, H. Ishii, T. Nakahashi, T. Takagi, S. Uchida, M. Seki, S. Suga, Y. Hidaka, M. Suzuki, T. Murakami, K. Oka and H. Unoki, J. Opt. Soc. Am. B **6**, 475 (1989)

115. W.Y. Lee, S.M. Garrison, M. Kawasaki, E.L. Venturini, B.T. Ahn, R. Boyers, J. Salem, R. Savoy and J. Vazquez, Appl. Phys. Lett. **60**, 772 (1992)

116. Z. Schlesinger, R.T. Collins, N.C. Yeh, W.Y. Lee and S.S.P. Parkin, Physica C **162-164**, 1111 (1989)

117. I. Bozovic, J.H. Kim, J.S. Harris and W.Y. Lee, Phys. Rev. B **43**, 1169 (1991)

118. R.B. Hammond, G.B. Negrete, L.C. Bourne, D.D. Strother, A.H. Cardona and M.M. Eddy, Appl. Phys. Lett. **57**, 825 (1990)

119. J.S. Martens, V.M. Hietala, D.S. Ginley, T.E. Zipperian and G.K.G. Hohenwarter, Appl. Phys. Lett. **58**, 2326 (1991)

120. T. Zetterer, M. Franz, J. Schutzmann, W. Ose, H.H. Otto and K.F. Renk, Phys. Rev. B **41**, 9499 (1990)

121. A.D. Kulkarni, F.W. DeWette, J. Prade, U. Schroder and W. Kress, Phys. Rev. B **41**, 6409 (1990)

122. D. Yoshioka and H. Fukuyama, J. Phys. Soc. Jpn. **54**, 2996 (1985)

123. V.J. Emery, J. Appl. Phys. **67**, 4666 (1990)

124. F. Sharifi, A. Pargellis, R.C. Dynes, B. Miller, E.S. Hellman, J. Rosamilia and E.H.H. Jr., Phys. Rev. B **44**, 12521 (1991)

125. Q. Huang, J.F. Zasadzinski, N. Tralshawala, K.E. Gray, D.G. Hinks, J.L. Peng and R.L. Greene, Nature **347**, 369 (1990)

126. H. Sato, H. Takagi and S. Uchida, Physica C **169**, 391 (1990)

127. Z. Schlesinger, R.T. Collins, J.A. Calise, D.G. Hinks, A.W. Mitchell, Y. Zheng, B. Dabrowski, N.E. Bickers and D.J. Scalapino, Phys. Rev. B **40**, 6862 (1989)

128. E.S. Hellman, E.H.H. Jr. and E.M. Gyorgy, Appl. Phys. Lett. **58**, 1335 (1991)

129. B.M. Moon, C.E. Platt, R.A. Schweinfurth and D.J. VanHarlingen, Appl. Phys. Lett. **59**, 1905 (1991)

130. J. Amano, H. Ko, M. Narbutovskih, J. Sheats and K. Tibbs, (preprint)

131. M.S. Sherwin, P.L. Richards and A. Zettl, Phys. Rev. B **37**, 1587 (1988)

132. H. Sato, S. Tajima, H. Takagi and S. Uchida, Nature **338**, 241 (1989)

133. R. Loudon, The quantum theory of light , (Oxford, New York, NY, 1983)

134. M. Born and E. Wolf, Principles of Optics , (Pergamon, Elmsford, NY, 1970)

135. J.R. Jasperse, A. Kahan, J.N. Plendl and S.S. Mitra, Phys. Rev. **146**, 526 (1966)

136. E.S. Hellman and E.H.H. Jr., Phys. Rev. B (in press), (1993)

137. L. Ji, M.S. Rzchowski and M. Tinkham, Phys. Rev. B **42**, 4838 (1990)

138. A.M. Portis and K.W. Blazey, Solid State Communications **68**, 1097 (1988)

139. C.S. Owen and D.J. Scalapino, J. Appl. Phys. **41**, 2047 (1970)

140. C. Caroli, P.G. DeGennes and J. Matricon, Phys. Lett. **9**, 307 (1964)

141. C. Caroli and J. Matricon, Phys. Kondens. Materie **3**, 380 (1965)

142. J.I. Gittleman and B. Rosenblum, J. Appl. Phys. **39**, 2617 (1968)

143. M.W. Coffey and J.R. Clem, Phys. Rev. Lett. **67**, 386 (1991)

144. S.R. Spielman, (private communication)

145. P. Merchant, R.D. Jacowitz, K. Tibbs, R.C. Taber and S.S. Laderman, Appl. Phys. Lett. **60**, 763 (1992)

146. S.R. Spielman, B. Parks and J. Orenstein, (unpublished)

DATE
FILMED
1/6/94
END